THERMAL FATIGUE OF SOLDER JOINTS IN MICRO-ELECTRONIC DEVICES

by

PAMELA JOAN ADAMS

S.B., Massachusetts Institute of Technology (1984)

Submitted to the Department of
Mechanical Engineering
in Partial Fulfillment of the Requirements
for the Degree of

**MASTER OF SCIENCE
IN MECHANICAL ENGINEERING**

at the

MASSACHUSETTS INSTITUTE OF TECHNOLOGY
August, 1986
© Charles Stark Draper Laboratory, Inc. 1986

Signature of Author ____________________
Department of Mechanical Engineering
August, 1986

Approved by ____________________
Dr. Elaine Savage
Technical Supervisor, CSDL

Certified by ____________________
Prof. Lallit Anand
Thesis Supervisor

Accepted by ____________________
Ain A. Sonin
Chairman, Department Graduate Committee

MASSACHUSETTS INSTITUTE OF TECHNOLOGY

OCT 0 3 1986

LIBRARIES

Acknowledgements

I would like to extend my thanks to Professor Lallit Anand and Dr. Elaine Savage for their technical guidance and support, without which this work would not have been possible. I would also like to thank the many people at the Charles Stark Draper Laboratory whose technical assistance was invaluable. Finally, I wish to express my gratitude to my parents for their moral support and encouragement.

This report was prepared at The Charles Stark Draper Laboratory, Inc. under Contract N00030-84-C-0036.

Publication of this report does not constitute approval by the Draper Laboratory or the sponsoring agency of the findings or conclusions contained herein. It is published for the exchange and stimulation of ideas.

I hereby assign my copyright of this thesis to The Charles Stark Draper Laboratory, Inc., Cambridge, Massachusetts.

Permission is hereby granted by The Charles Stark Draper Laboratory, Inc. to the Massachusetts Institute of Technology to reproduce any or all of this thesis.

Thermal Fatigue of Solder Joints in Micro-Electronic Devices

by

Pamela J. Adams

Submitted to the Department of Mechanical Engineering
on August 15, 1986 in partial fulfillment of the
requirements for the Degree of Master of Science in
Mechanical Engineering

Abstract

The goal of this research was to develop a methodology to estimate the fatigue life during thermal cycling of solder joints formed between materials with different coefficients of thermal expansion. An isotropic elastic-perfectly-viscoplastic constitutive equation was formulated for 60/40 tin-lead solder. The elastic constants were determined using bounding theorems and the results compared favorably with available experimental results obtained by ultrasonic test methods. The viscoplastic equation is a hyperbolic sine model which fits the data over a range of temperatures between -55° C and 125 C and a range of strain rates between 8.33×10^{-5} s^{-1} and 8.33×10^{-2} s^{-1}. This equation is valid over a range of temperatures and strain rates much larger than any other equation found in the literature. The viscoplastic parameters were determined from isothermal tensile tests.

This constitutive model was implemented in a finite element code. A numerical analysis was performed to determine the cyclic plastic strains in a solder joint caused by thermal coefficient of expansion mismatch between a particular type of component and circuit board assembly.

Simultaneously, a double shear test fixture was designed to test solder joint properties in simple shear. Joints of 60/40 tin-lead solder were cast between pieces of a nickel-plated steel fixture. During the fatigue tests, cracks formed and propagated along the nickel-solder interface, indicating that the interface was weaker than the solder joint. A Coffin-Manson relation for low cycle fatugye crack propagation was fit to the data. Using the numerical results about cyclic plastic strains and the experimental fatigue-life curves, an estimate of the life of the numerically modelled solder joint was made as an example of the methodology. Because of the interfacial failure in the experiments the predicted life was lower than observed in ongoing experiments at the C. S. Draper Laboratory. Some directions for future research are suggested.

Thesis Supervisor: Prof. Lallit Anand
Title: Associate Professor of Mechanical Engineering

Contents

1 Introduction **5**

2 Constitutive Equations **8**

2.1 Theory 8

2.2 Determination of Material Parameters 11

2.2.1 Elastic Constants 11

2.2.2 Tensile Test Results 19

2.2.3 Viscoplastic Constitutive Equation 20

2.3 Comparison of the model to the data 23

3 Finite Element Analysis **23**

3.1 Component and Joint Configuration 24

3.2 Model 26

3.3 Results 28

4 Fatigue Test Method **31**

4.1 Fixture Design 31

4.2 Specimen Fabrication 33

4.3 Microstructure 36

4.4 Fatigue Testing 40

4.4.1 Experimental Procedure 40

4.4.2 Results 41

5 Discussion **43**

6 Conclusions and Recommendations **44**

References **48**

A Mechanical Drawings of Double Shear Test Fixture **52**

List of Tables **64**

List of Figures **72**

1 Introduction

For high reliability applications, electronic circuit board assemblies are thermally cycled to test mechanical workmanship. Each assembly contains two circuit boards laminated to either side of an aluminum frame heat sink. Ceramic components are joined to solder-plated copper pads on these circuit boards with near-eutectic tin-lead solder. During thermal cycling, the thermal coefficient of expansion (TCE) difference between the board/frame assembly and the ceramic components causes strain-controlled fatigue of the tin-lead solder joints. The heat sink, which is not used in most commercial applications, causes a higher TCE mismatch than what is found in commercial assemblies.

At the C. S. Draper Laboratory in Cambridge, Mass., experience with electronic assemblies of this type has shown that cracks appear in the solder joints during thermal cycling. However, the thermal fatigue cracks appear long before the occurrence of electrical failure [1] of the solder joint. Independent of the definition of electrical failure, the formation and growth of thermal fatigue cracks and the occurrence of electrical failure are ultimately related. It is therefore of interest to characterize the mechanical performance, and in particular the fatigue behavior, of these joints.

The overall intent in this work is to develop a methodology to analyse the deformation and fatigue behavior of these joints. The steps in this methodology are:

[1] The definition of electrical failure of a solder joint depends upon the component involved, and is often defined as a 5 or 10% change in electrical resistance of the solder joint, as in the work by Wild [1].

1. Develop a set of elasto-viscoplastic constitutive equations that model the rate-dependent plastic deformation behavior of the particular solder alloy.

2. Use these constitutive equations to numerically model the thermo-mechanical behavior of representative solder joints in electronic assemblies with finite element methods to determine the cyclic plastic strain levels in the solder joints during thermal cycling.

3. Devise experiments to determine the fatigue life for mechanical failure of solder joints under isothermal cyclic straining.

4. Use the results from (2) and (3) above to *estimate* the mechanical fatigue life during thermal cycling of a solder joint in an electronic assembly.

Here we report on our efforts at (1) formulating constitutive equations and determining the material parameters for a 60/40 tin-lead alloy; (2) modelling the response to thermal cycling of a particular electronic assembly by using the finite element method; and (3) determining the strain-life behavior of the 60/40 tin-lead solder in isothermal shear fatigue at room temperature. We emphasize that although the results reported here are extremely encouraging they are indeed preliminary, and much work needs to be done to refine the methodology before it may actually be used.

Although some data on the mechanical properties of tin-lead solders exists, published results are for a variety of test conditions, and in particular a wide range of strain rates. Thus, these results vary considerably. A series of tensile tests was

therefore conducted for temperatures ranging from -55° C to 125° C and strain rates ranging from 8.33 x $10^{-5}s^{-1}$ to 8.33 x $10^{-2}s^{-1}$. An elastic-perfectly-viscoplastic model was formulated and the relevant viscoplastic parameters were determined from these tests. The elastic constants were calculated by using bounding theorems. These equations were then incorporated into a user material subroutine developed by Anand et al. [2] for the ABAQUS [3] finite element code.

A photograph of the assembly which was then modelled with ABAQUS [3] is shown in Figure 1, and a schematic of the assembly cross-section is included in Figure 2. The electrical components in the assembly are barium titanate ceramic chip capacitors with five-sided end terminations made of a fired silver-borosilicate glass mixture. The test boards are a polyimide-glass composite and are mounted on an aluminum frame. The solder is a 60/40 tin-lead alloy.

The region of highest strain in a solder joint has been analytically determined as the area under the capacitor, which deforms in an approximate simple shear mode during thermal cycling. Therefore, we chose to perform the fatigue testing in shear as well. A double shear fixture was designed so that end effects in the solder joints were minimized. The fixture was designed to avoid backlash so that tests could be conducted in reverse shear. In addition, MTS hydraulic grips were used to eliminate backlash from the load train. These tests were conducted with an MTS 880 servo-hydraulic system.

Preliminary tests were conducted to determine a fatigue life curve for the solder

alloy at room temperature using two mechanical failure criteria. Then, using the finite element estimates of the maximum plastic strain amplitude in the joint, an estimate was made of the number of cycles to these failure critera for the chip capacitor solder joint during thermal cycling. These results are compared to the preliminary results of actual thermal cycling tests of chip capacitor solder joints which are in progress at the C. S. Draper Laboratory.

In future work, this methodology will be used to compare alternate reflow soldering processes involving different solder joint geometries, such as manual soldering, heater bar soldering, and vapor phase soldering. In addition, comparisons of the behavior of alternate soft solder alloys will also be made.

2 Constitutive Equations

2.1 Theory

In a one-dimensional idealization of elastic-viscoplastic behavior, the total strain rate is additively decomposed into the elastic strain rate and the plastic strain rate,

$$\dot{\epsilon} = \dot{\epsilon}^e + \dot{\epsilon}^p. \tag{1}$$

The elastic strain rate is given by the relation

$$\dot{\epsilon}^e = \frac{\dot{\sigma}}{E} + \alpha \dot{\theta}, \tag{2}$$

where σ is the stress, θ is the absolute temperature, E is the Young's modulus, and α is the coefficient of thermal expansion. The viscoplastic strain rate is a function of

the current stress level, the absolute temperature, and a list of internal state variables I_n,

$$\dot{\epsilon}^p = f(\sigma, \theta, I_n). \tag{3}$$

The characterization of these internal state variables is currently one of the unsolved problems in plasticity. As a first approximation we assume that the internal state of the material can be adequately described with one scalar parameter, the deformation resistance s, as in Anand [4]. In pure metals, s is proportional to $\mu b\sqrt{\rho}$, where μ is the shear modulus, b is the magnitude of the Burgers vector, and ρ is the dislocation density. Further, we assume that the evolution of s depends on the current values of stress, temperature, and the deformation resistance:

$$\dot{s} = g(\sigma, \theta, s). \tag{4}$$

Following Anand [5], we assume isotropy and generalize these equations to three dimensions as follows. We use notation which is standard in continuum mechanics, as in Gurtin [6]. Scalars are written as lowercase letters, both vectors and points are boldface lowercase letters; second order tensors are boldface uppercase letters; and fourth order tensors are written as script uppercase letters. Some standard definitions are listed below:

$\mathbf{x} = \tilde{\mathbf{x}}(\mathbf{p}, t)$...motion;

$\mathbf{p} = \tilde{\mathbf{p}}(\mathbf{x}, t)$ ...reference map;

$\dot{\mathbf{x}}(\mathbf{p}, t) = \frac{\partial}{\partial t}\tilde{\mathbf{x}}(\mathbf{p}, t)$...velocity;

$\mathbf{v}(\mathbf{x},t) = \dot{\mathbf{x}}(\bar{\mathbf{p}}(\mathbf{x},t),t)$ ...spatial description of velocity;

$\mathbf{F} = \frac{\partial}{\partial \mathbf{p}}\bar{\mathbf{x}}(\mathbf{p},t),\ \det\mathbf{F} > 0$...deformation gradient;

$\mathbf{L}(\mathbf{x},t) = \frac{\partial}{\partial \mathbf{x}}\mathbf{v}(\mathbf{x},t) = \dot{\mathbf{F}}\mathbf{F}^{-1}$ ...velocity gradient;

$\mathbf{D}(\mathbf{x},\mathrm{t}) = \frac{1}{2}(\mathbf{L}+\mathbf{L}^T)$...stretching tensor;

$\mathbf{W}(\mathbf{x},\mathrm{t}) = \frac{1}{2}(\mathbf{L}-\mathbf{L}^T)$ ...spin tensor;

$\mathbf{T}(\mathbf{x},\mathrm{t}) = \mathbf{T}^T(\mathbf{x},\mathrm{t})$ ...Cauchy stress tensor;

$\mathbf{T}'(\mathbf{x},t) = \mathbf{T} - \frac{1}{3}(tr\mathbf{T})\mathbf{1}$...Deviatoric part of the Cauchy stress tensor;

$\mathbf{T}^{\nabla}(\mathbf{x},t) = \dot{\mathbf{T}} - \mathbf{W}\mathbf{T} + \mathbf{T}\mathbf{W}$...Jaumann derivative of the Cauchy stress tensor.

To generalize equation 1, the stretching tensor $\mathbf{D}$ may be additively decomposed into its elastic and plastic parts:

$$\mathbf{D} = \mathbf{D}^e + \mathbf{D}^p \tag{5}$$

For infinitesimal elastic stretches and isotropy, the elastic stretching is given by

$$\mathbf{D}^e = \mathcal{K}\mathbf{T}^{\nabla} + \mathbf{A}\dot{\theta}, \tag{6}$$

which is the generalization of equation 2. Here, the compliance tensor $\mathcal{K}$ is defined as

$$\mathcal{K} = \frac{1}{2\mu}\left(\mathcal{I} - \frac{1}{3}\mathbf{1}\otimes\mathbf{1}\right) + \frac{1}{3k}\left(\frac{1}{3}\mathbf{1}\otimes\mathbf{1}\right), \tag{7}$$

where μ is the shear modulus, k is the bulk modulus, and $\mathcal{I}$ is the fourth order identity tensor. $\mathbf{A}$ is the strain temperature tensor

$$\mathbf{A} = \alpha\mathbf{1}, \tag{8}$$

with α the thermal coefficient of expansion.

The Flow Rule, which is the generalization of equation 3, is

$$\mathbf{D}^p = \dot{\bar{\epsilon}}^p \left[\frac{3\mathbf{T}'}{2\tilde{\sigma}} \right]. \tag{9}$$

The equivalent tensile stress $\tilde{\sigma}$ is defined by

$$\tilde{\sigma} = \left\{ \left(\frac{3}{2} \right) \mathbf{T}' \cdot \mathbf{T}' \right\}^{\frac{1}{2}}, \tag{10}$$

and $\dot{\bar{\epsilon}}^p$ is an equivalent plastic tensile strain rate which is a function of the equivalent stress, the temperature, and the deformation resistance:

$$\dot{\bar{\epsilon}}^p = \hat{\mathrm{f}}(\tilde{\sigma}, s, \theta) > 0,$$

$$\text{with } \hat{\mathrm{f}}(0, s, \theta) = 0. \tag{11}$$

A particular form for the function $\hat{\mathrm{f}}$ will be discussed later. The generalization of equation 4 is simply

$$\dot{s} = \hat{\mathrm{g}}(\tilde{\sigma}, \theta, s). \tag{12}$$

2.2 Determination of Material Parameters

2.2.1 Elastic Constants

Values reported in the literature for the elastic modulus of near-eutectic tin-lead solders are typically obtained by performing tension tests. However, even at room temperature these alloys are at high homologous temperatures. For example, the 60/40 tin-lead alloy reaches the liquidus at 185° C, and is therefore at 0.65 T_m at room

temperature and at 0.5 T_m at -44° C. Since these materials are in the high temperature regime, elastic moduli found from tensile stress-strain curves are lower than true elastic moduli because of the accompanying time-dependent plastic deformation.

A graph comparing some of the published results for the Young's modulus of near-eutectic tin-lead solders as functions of temperature is shown in Figure 3. The variation in the results shown here may be explained by the different rates at which testing was conducted and by the different methods used to calculate the Young's modulus.

The calculation of bounds for the elastic constants using bounding theorems obtained by Hashin and Shtrickman [10] was prompted by both the variability of available results in the literature and concerns about the method for determining the elastic constants from tension tests performed at such high homologous temperatures. These theorems bound the effective elastic moduli of isotropic multi-phase materials with arbitrary phase geometry by using the isotropic elastic constants of the phases to estimate the elastic constants of the alloy. The elastic constants of the individual phases were estimated by using these theorems with the bounds for pure tin and pure lead. The bounds for the pure metals were estimated from single crystal constants which were determined from ultrasonic testing.

Bounds for the moduli of β-tin: First, the bounds for the bulk and shear moduli of β-tin were calculated. (Although pure tin is known to undergo a phase transforma-

tion from the tetragonal β-tin to the cubic α-tin at 13° C, this phase transformation does not occur when the tin is alloyed with lead.) The stiffness matrix for a tetragonal material is

$$\begin{pmatrix} C_{11} & C_{12} & C_{13} & 0 & 0 & 0 \\ C_{12} & C_{11} & C_{13} & 0 & 0 & 0 \\ C_{13} & C_{13} & C_{33} & 0 & 0 & 0 \\ 0 & 0 & 0 & C_{44} & 0 & 0 \\ 0 & 0 & 0 & 0 & C_{44} & 0 \\ 0 & 0 & 0 & 0 & 0 & C_{66} \end{pmatrix}.$$

Values for the single crystal constants of β-tin were obtained from Hellwege [11] for temperatures below 300° K. The data was in the form of reference values at 300° K and linear temperature dependence terms for both 100° K to 300° K and 200° K to 300° K for each single crystal stiffness. Above 300° K, data was obtained from Kammer et al. [12]. Here, values of the single crystal constants were listed at various temperatures, so the constants at temperatures of interest for this work were obtained by interpolation. The calculated single crystal constants are listed in Table 1.

Voigt and Reuss bounds for polycrystalline materials were then used to calculate the shear and bulk moduli. These bounds were obtained from Simmons and Wang [14]. Voigt upper bounds were derived by averaging the single crystal elastic stiffnesses over all space, while the Reuss lower bounds were obtained by similarly averaging the single crystal elastic compliances. The compliances were calculated from the stiffness data by a standard matrix inversion. The Voigt bounds are:

$$\kappa_V = \frac{1}{3}(A + 2B) \tag{13}$$

$$\mu_V = \frac{1}{5}(A - B + 3C) \tag{14}$$

where

$$3A = C_{11} + C_{22} + C_{33} \tag{15}$$

$$3B = C_{23} + C_{31} + C_{12} \tag{16}$$

$$3C = C_{44} + C_{55} + C_{66}. \tag{17}$$

The Reuss bounds are:

$$\kappa_R = \frac{1}{3a + 6b} \tag{18}$$

$$\mu_R = \frac{5}{4a - 4b + 3c} \tag{19}$$

where

$$3a = S_{11} + S_{22} + S_{33} \tag{20}$$

$$3b = S_{23} + S_{31} + S_{12} \tag{21}$$

$$3c = S_{44} + S_{55} + S_{66}. \tag{22}$$

Results of these calculations are listed in Table 2, and they are also plotted in Figure 4. The discontinuity in the bulk modulus of tin at about 300 K occurs because the data was obtained from two different sources.

Bounds for the moduli of lead: Lead is a cubic metal, and the single crystal stiffness matrix for a cubic material is

$$\begin{pmatrix} C_{11} & C_{12} & C_{12} & 0 & 0 & 0 \\ C_{12} & C_{11} & C_{12} & 0 & 0 & 0 \\ C_{12} & C_{12} & C_{11} & 0 & 0 & 0 \\ 0 & 0 & 0 & C_{44} & 0 & 0 \\ 0 & 0 & 0 & 0 & C_{44} & 0 \\ 0 & 0 & 0 & 0 & 0 & C_{44} \end{pmatrix}.$$

Data for the single crystal elastic constants of lead at a reference temperature of 300° K and the temperature coefficients for 100° K to 300° K, 200° K to 300° K, and 300° K to 600° K were obtained from Hellwege [13]. Calculated values of these constants at some temperatures of interest are listed in Table 3. For cubic metals, the bulk modulus can be calculated exactly with the equation

$$\kappa = \frac{1}{3}(C_{11} + 2C_{12}). \tag{23}$$

The Hashin-Shtrickman bounds for single phase cubic metals were then used to calculate the shear modulus bounds for lead. These bounds were taken from Simmons and Wang [14]. As in Simmons and Wang, we will use the subscript H to denote the upper bound and the subscript S to denote the lower bound. The upper bound, μ_H, is

$$\mu_H = \mu_1 + 3\left(\frac{5}{\mu_2 - \mu_1} + 4\left(\frac{3(\kappa + 2\mu_1)}{5\mu_1(3\kappa + 4\mu_1)}\right)\right)^{-1}, \tag{24}$$

and the lower bound, μ_S, is

$$\mu_S = \mu_2 + 2\left(\frac{5}{\mu_1 - \mu_2} + 6\left(\frac{3(\kappa + 2\mu_2)}{5\mu_2(3\kappa + 4\mu_2)}\right)\right)^{-1} \tag{25}$$

where

$$\mu_1 = \frac{1}{2}(C_{11} - C_{12}) \tag{26}$$

$$\mu_2 = C_{44}. \tag{27}$$

The results of these calculations are listed in Table 4 and plotted in Figure 5.

Bounds for the moduli of the tin-rich and lead-rich phases: The moduli calculated for pure tin and pure lead were then used to obtain bounds for the moduli of the lead-rich and tin-rich phases using the Hashin-Shtrickman bounds [10] for two phase materials:

$$\kappa_U^* = \kappa_{Sn} + \frac{v_{Pb}}{\frac{1}{\kappa_{Pb}-\kappa_{Sn}} + \frac{3v_{Sn}}{3\kappa_{Sn}+4\mu_{Sn}}}, \tag{28}$$

$$\kappa_L^* = \kappa_{Pb} + \frac{v_{Sn}}{\frac{1}{\kappa_{Sn}-\kappa_{Pb}} + \frac{3v_{Pb}}{3\kappa_{Pb}+4\mu_{Pb}}}, \tag{29}$$

$$\mu_U^* = \mu_{Sn} + \frac{v_{Pb}}{\frac{1}{\mu_{Pb}-\mu_{Sn}} + \frac{6(\kappa_{Sn}+2\mu_{Sn})v_{Sn}}{5\mu_{Sn}(3\kappa_{Sn}+4\mu_{Sn})}}, \text{and} \tag{30}$$

$$\mu_L^* = \mu_{Pb} + \frac{v_{Sn}}{\frac{1}{\mu_{Sn}-\mu_{Pb}} + \frac{6(\kappa_{Pb}+2\mu_{Pb})v_{Pb}}{5\mu_{Pb}(3\kappa_{Pb}+4\mu_{Pb})}}. \tag{31}$$

Here the upper and lower bounds for the bulk modulus are κ_U^* and κ_L^*, and for the shear modulus are μ_U^* and μ_L^*, respectively. The bounds for the moduli of the pure metals were substituted appropriately into equations 28 to 31 so as to not artificially tighten the resulting bounds.

The variables v_{Pb} and v_{Sn} are the volume fractions of lead and tin, respectively. Since the solder used here was chill-cast, it was assumed that the compositions of

the phases remained the same as those formed upon solidification, or that the lead rich phase was 81.0 wt.% lead and the tin-rich phase was 97.5 wt.% tin. (See the phase diagram in Figure 6.) A SEM micrograph of 60/40 tin-lead solder is shown in Figure 7. The lighter regions are the lead-rich phase and the darker matrix is the tin-rich phase. The volume fraction of lead in in the lead-rich phase is .732 at room temperature, and the volume fraction of tin in the tin-rich phase is .984 at room temperature. The volume fractions change no more than ±.40% over the temperature range of interest. The resultant bounds are listed in Tables 5 and 6.

Bounds for the moduli of 60/40 tin-lead solder: Finally, the bounds for the moduli of the 60/40 tin-lead alloy were obtained by using the same Hashin-Shtrickman bounds [10] for two-phase materials and the bounds of the moduli calculated above for the tin-rich and the lead-rich phases. Calling the lead-rich phase α and the tin-rich phase β, these equations become:

$$\kappa_U = \kappa_\beta + \frac{v_\alpha}{\frac{1}{\kappa_\alpha - \kappa_\beta} + \frac{3v_\beta}{3\kappa_\beta + 4\mu_\beta}}, \quad (32)$$

$$\kappa_L = \kappa_\alpha + \frac{v_\beta}{\frac{1}{\kappa_\beta - \kappa_\alpha} + \frac{3v_\alpha}{3\kappa_\alpha + 4\mu_\alpha}}, \quad (33)$$

$$\mu_U = \mu_\beta + \frac{v_\alpha}{\frac{1}{\mu_\alpha - \mu_\beta} + \frac{6(\kappa_\beta + 2\mu_\beta)v_\beta}{5\mu_\beta(3\kappa_\beta + 4\mu_\beta)}}, \text{ and} \quad (34)$$

$$\mu_L = \mu_\alpha + \frac{v_\beta}{\frac{1}{\mu_\beta - \mu_\alpha} + \frac{6(\kappa_\alpha + 2\mu_\alpha)v_\alpha}{5\mu_\alpha(3\kappa_\alpha + 4\mu_\alpha)}}. \quad (35)$$

The volume fraction of the tin-rich phase in 60/40 tin-lead solder is .6061 at room temperature, and varies no more than .12% over the temperature range of the

calculations. The results of these calculations are listed in Table 7.

The bounds for the Young's modulus were then calculated using the relationship

$$E = \frac{9\kappa\mu}{3\kappa + \mu}. \tag{36}$$

These bounds are compared to some of the published data and to some data obtained from ultrasonic testing by Getzan [16] in Figure 8. The predictions for E based on the calculations using the bounding theorems are in very good agreement with the experiments of Getzan [16]. It should be noted, however, that the bounding equations are very sensitive to the estimated volume fraction of the phases. For example, assuming equilibrium composition of the phases at room temperature lowers the bounds by approximately 10%. The differences in the results obtained from tension testing and the ultrasonic data as seen in Figure 8 are probably due to time-dependent plastic deformation occuring during the tension tests.

Two elastic constants are needed to describe the isotropic elastic behavior of the solder, and the two used in the user material subroutine [2] are the bulk modulus and the shear modulus. The bulk modulus was obtained by averaging the results of the bounding theorems. It was chosen instead of the shear modulus since its bounds were tighter. The relationship

$$\mu = \frac{9\kappa E}{9\kappa - E} \tag{37}$$

was then used to find the shear modulus using the calculated bulk modulus and the Young's modulus obtained from ultrasonic testing by Getzan [16]. The final results are

listed in Table 8. These data points were fit to linear curves valid over the temperature range from 218° K (-55° C) to 398° K (125° C). The equations for these curves are:

$$\mu = 24.28 - .0290\theta, \text{and} \tag{38}$$

$$\kappa = 61.06 - .0274\theta, \tag{39}$$

where θ is the absolute temperature. The regression coefficients for these linear curve fits were 99.04% for the shear modulus and 93.24% for the bulk modulus. The results are plotted in Figure 9.

2.2.2 Tensile Test Results

To determine the values of the viscoplastic parameters, a series of tensile tests was conducted on an Instron 1122. The tests were performed at constant temperatures between -55° C and 125° C and over a range of strain rates from 8.33 x 10^{-5} s^{-1} to 8.33 x 10^{-2} s^{-1}. The test matrix is listed in Table 9. These tests were run at a constant crosshead speed, but since only small strain data was used this was assumed to be approximately constant true strain rate. The specimens were manufactured by machining cast bars of Alpha Metals 60/40 tin-lead solder according to ASTM standard E-8-82. The room temperature data is plotted in Figure 10 showing the strain rate dependence of the material. The rest of the data is shown in Figures 11 to 13, where stress-strain curves obtained at rates of 1.67x10^{-2} s^{-1}, 1.67x10^{-3} s^{-1}, 1.67x10^{-4} s^{-1} are plotted.

2.2.3 Viscoplastic Constitutive Equation

The constitutive equation for the equivalent plastic strain rate was determined as follows. The plastic strain rate is a function of the stress, the temperature and the deformation resistance,

$$\dot{\epsilon}^p = \hat{f}(\sigma, s, \theta). \tag{40}$$

The inverse of this equation is

$$\sigma = g_1(\dot{\epsilon}^p, \theta, s). \tag{41}$$

Using the Zener-Holloman parameter [17],

$$Z \equiv \dot{\epsilon}^p \exp\left(\frac{Q}{R\theta}\right), \tag{42}$$

which is a temperature compensated strain rate, equation 41 can be written as a function of this parameter and the internal variable s:

$$\sigma = g_2(Z, s). \tag{43}$$

In equation 42 Q is and activation energy and θ is the absolute temperature. If we assume that the stress must scale with the deformation resistance, then at a constant strain rate and temperature

$$\sigma = s \times \{g_3(Z)\}, \tag{44}$$

where g_3 is a function of Z alone. Given that the stress-strain curves show little or no strain hardening after strains of the order of approximately 5%, a non-hardening

version of the constitutive model was adopted. In this case, the deformation resistance s is set equal to a steady state deformation resistance s^* and no evolution equation for s is needed. Equation 44 then becomes

$$\sigma = s^* \times \{g_3(Z)\}. \tag{45}$$

The stress level corresponding to the assumption of a constant value of s during viscoplastic flow was taken as either the maximum stress level or the stress level at 5% strain.

Following Sellars and Tegart [18], we can take the function g_3 as

$$g_3(Z) = \frac{1}{\xi}\sinh^{-1}\left[\frac{Z}{A}\right]^m, \tag{46}$$

where ξ, A, and m are material parameters. Finally, equation 45 may be rewritten as

$$\dot{\epsilon}^p = A\exp\left(-\frac{Q}{R\theta}\right)\left[\sinh\left(\frac{\xi\sigma}{s^*}\right)\right]^{\frac{1}{m}}. \tag{47}$$

The method used to determine A, Q, s^*, ξ, and m is as follows:

1. The low strain rate high temperature data was fit to the power law constitutive equation:

$$\dot{\epsilon}^p = A^*\exp\left(-\frac{Q}{R\theta}\right)\left(\frac{\sigma}{s^*}\right)^{\frac{1}{m}}. \tag{48}$$

From this, a value of the activation energy was determined using a linear least-squares algorithm.

2. Equation 47 was written in the form

$$\dot{\epsilon}^p = A \exp\left(-\frac{Q}{R\theta}\right)[\sinh \alpha\sigma]^{\frac{1}{m}} \tag{49}$$

where

$$\alpha = \frac{\xi}{s^*}. \tag{50}$$

3. This equation was fit to the data using the non-linear least-squares algorithm ZXSSQ (an IMSL [19] routine) to find A, α, and m with the value of Q that was determined in step 1.

4. Since s^* and ξ are not independent, the constant s^* was chosen arbitrarily to be 50 MPa, and ξ was calculated from equation 50.

The results are:

m = .4118,

Q = 57.32 kJ/mol,

ξ = 5.363, and

A = 2893. s^{-1}

In Figure 14, the data for the stress level at 5% strain is plotted versus the Zener-Holloman parameter [17]. The value of Q calculated above was used to determine Z. The dotted line is the prediction from the model.

The values for Q and m determined here are consistent with those found in other work. They are compared to some published results in Tables 10 and 11. These values were all found using different forms of a power law relation between plastic strain rate

and stress, except for Schneibel and Hazzledine [21]. They used a Coble creep equation which is valid for small strains and where $m = 1$ is assumed to calculate the activation energy, but they calculated the strain rate sensitivity using the definition

$$m = \left. \frac{\partial \log \sigma}{\partial \log \dot{\epsilon}^p} \right|_{T,L=const} . \tag{51}$$

2.3 Comparison of the model to the data

This elastic-perfectly viscoplastic model was incorporated into the user material subroutine developed by Anand et al. [2]. Using the ABAQUS [3] finite element code, the tensile tests were simulated using a one element mesh. The resulting stress-strain curves are compared to the data in Figures 15 to 21. Figures 15 to 20 compare the results at each of the temperatures at which tests were conducted, while Figure 21 shows the results of all the data taken at a strain rate of 1.67x10^{-3} s^{-1}.

Obviously, this type of a model is an approximation to the shape of the stress-strain curve. However, it does model the temperature and strain-rate dependence of plastic flow quite well.

3 Finite Element Analysis

Using the constitutive equations for 60/40 tin-lead solder developed in the previous section, thermal cycling of a soldered chip capacitor assembly is modelled. First, the actual test configuration of the chip capacitor and the solder joint is described. Then, the assumptions made about material properties and the thermal cycle for the

purposes of the finite element analysis are discussed. Finally, the results obtained from the analysis are reported.

3.1 Component and Joint Configuration

For thermal cycling tests, components are soldered to boards without copper runs or plated through holes. The nominal dimensions of the chip capacitor are .250 inches along the sides with the solder joints and .220 inches wide. The thickness of the component is determined by the required capacitance. In this case, the capacitor chosen for the model was .060 inches thick.

The solder joints in electronic assemblies that are to be thermally cycled are examined both optically and in a scanning electron microscope (SEM) for the initial evaluations. These examinations are repeated at intervals during the cycling, and some boards are cross-sectioned. A SEM micrograph of a cross-sectioned chip capacitor soldered to such a test board is shown in Figure 22. This assembly was cross-sectioned prior to thermal cycling. The capacitor is made of laminated layers of a barium titanate dielectric and platinum-palladium electrodes. These electrodes are the thin horizontal lines visible in the photograph of the cross-sectioned chip capacitor. The capacitor is designed so that alternating electrodes are electrically connected by one end termination (i.e. if the capacitor were electrically connected, all would be at the same voltage). The remaining electrodes are connected to the opposite end termination, forming many thin capacitors in parallel.

The end termination is a thick paste mixture of silver and a boro-silicate glass which is applied to the capacitors by dipping, and then fired. The metallization is then barrel plated with a nickel diffusion barrier, followed by tin plating to prevent the formation of nickel oxides and provide enhanced solderability.

The solder joint is formed by the following process:

1. The chip is aligned on copper pads which have been previously plated with one to two mils of eutectic (61.9Sn-38.1Pb) tin-lead solder.

2. Heat is then applied to both pads. No additional solder is added.

3. The solder melts and flows up the sides of the chip capacitor and underneath, achieving additional standoff height. The chip is allowed to settle during this step.

Due to this process both the fillet shape and the thickness of the solder beneath the component can vary. The ones shown here have a relatively small standoff height. A photograph of one of the solder joints shown in Figure 22 is shown at a higher magnification in Figure 23. The tin-rich area at the top of the fillet (the darker area) is caused by the tin plating on the capacitor. The height of the solder layer beneath the capacitor in this photograph is approximately .0007 inches.

Micrographs of a cross-sectioned chip capacitor that was subjected to 200 thermal cycles between the limits of -20° C and 100° C with a transfer time of approximately 5 seconds and hold times of 30 minutes at each limit are shown in Figures 24 and 25.

Note the crack that formed in the solder beneath the chip capacitor at the end of the metallization, which is indicated in Figure 25 by an arrow. This location is a typical one for crack growth in these assemblies when subjected to this type of thermal cycle.

3.2 Model

Several assumptions had to be made about the material properties of the chip capacitor, the metallization, and the board due to a lack of available experimentally determined data and the inherent variability in the manufacturing process. The properties of the board and the solder were modelled as temperature dependent. Since modulus data was available only at certain temperatures, the moduli were assumed constant for a range about these temperatures. The properties of the other materials were assumed to be constant over the temperature range of the thermal cycle.

The mechanical properties of the capacitor were assumed to be the same as those of bulk barium titanate, although the ceramic used in the capacitors contains proprietary additives. The electrodes in the chip capacitor were not modelled.

No mechanical properties were available for the silver-glass metallization, which is a mixture of one-third boro-silicate glass and two-thirds silver, so the mechanical properties and the thermal coefficient of expansion were assumed to be the same as those of silver. Since the nickel and tin plating are thin compared to the metallization, it was assumed that they had little mechanical effect on the solder joint and did not need to be included in the model.

According to Safranek [26], the mechanical properties of plated copper are approximately the same as those of annealed copper. The Young's modulus was obtained from his data, while the Poisson's ratio was assumed to be the same as that of bulk copper.

The board was modelled as isotropic using elastic moduli found along the length of the glass fibers since no data was available for properties through the thickness of the board. The modulus data used was for a board with a 42.45 wt % resin content. The properties used in the finite element model are listed in Table 12, along with appropriate references.

Thermal cycles such as the ones experienced by the component and solder joints shown in Figures 24 and 25 are accomplished by moving the assembly between two chambers, one at each temperature extreme. The transfer time is approximately 5 seconds; the hold time is 30 minutes. The temperature of the assembly would actually change more slowly than the ambient temperature, as shown schematically in Figure 26. However, as a first approximation it was assumed that the temperature of the assembly was the same as the ambient temperature. This assumption causes the estimates of strain rate, and therefore strain, to be higher than in an actual assembly. It was also assumed that the temperatures of all parts of the assembly remained equal at all times during the thermal cycle, so that strains caused by thermal gradients were not considered. Also, in this preliminary analysis, the hold times have been neglected. The temperature history input for this analysis is shown in Figure 27.

Figure 28 shows the finite element mesh of the electronic assembly. Since the assembly is symmetric about the centerline of the frame, the model includes only one board and half of the frame. The bottom two rows of elements in the mesh are the aluminum frame. Boundary conditions established along the centerline of the frame were that no movement could take place in the 2-direction (see figure). The solder joint assembly is also symmetric about the centerline of the capacitor, where the boundary conditions were that no movement was allowed in the 1-direction. This was a plane strain analysis.

A more detailed plot of the solder joint mesh is shown in Figure 29. The length to width ratios of the elements at the top and far right of the joint are about 10:1, but this is not critical since these areas are subjected to very little strain. The elements at the left end of the mesh (under the chip capacitor) were made rectangular even though this does not accurately model the geometry of an actual solder joint. For example, compare the fillets in the photographs in either Figure 23 or Figure 25 to the mesh. Since these geometries are so different, the results in this corner cannot be considered accurate. However, results approximately three elements away from this corner are not influenced by this geometry and can be considered reliable.

3.3 Results

The results show quite clearly that the deformation in the solder joint is concentrated in the region below the chip capacitor. The equivalent plastic shear strain contours at

100° C in the first cycle are plotted in Figures 30 to 32. The plastic strain levels are very high in the lower left hand corner of the joint, but this is an artifact of the mesh geometry. The difference in the mesh geometry and the geometry of an actual solder joint fillet explains why the highest strain levels in the mesh are not in the same place as the cracks in the solder joint.

Ignoring the effects of the corner, the integration point with the highest plastic strain level is the point indicated by the arrow on the contour plot. The equivalent plastic shear strain and the equivalent plastic shear stress at this point are plotted against time in Figure 33.

When the temperature reaches a maximum or a minimum and the shear deformation changes direction, the equivalent plastic strain rate does not decrease to zero immediately as it would in a material at a low homologous temperature. Therefore the equivalent plastic strain continues to increase slightly as is shown in Figure 33. Since the solder is in the high temperature regime throughout the temperature cycle a non-zero stress will cause the plastic strain to increase with time. This change in plastic strain is greater at the higher temperature extremum than at the lower.

The equivalent shear stress and the equivalent plastic shear strain are cross-plotted in Figure 34. The goal is to change these results into hysteresis loops for shear deformation. Then, the results can be compared with the results of the double shear fatigue tests which will be discussed later. This was accomplished in the following manner.

The equivalent shear stress is

$$\tilde{\tau} = \frac{\tilde{\sigma}}{\sqrt{3}} = \left| \left\{ \left(\frac{1}{2} \right) \mathbf{T}' \cdot \mathbf{T}' \right\}^{\frac{1}{2}} \right|, \tag{52}$$

where by convention the positive root is always taken. We will define an equivalent stress τ^* which can be either positive or negative, but is otherwise equal to the equivalent shear stress $\tilde{\tau}$. Also, the equivalent plastic shear strain rate is

$$\dot{\tilde{\gamma}}^p = \sqrt{3}\dot{\tilde{\epsilon}}^p, \tag{53}$$

and the equivalent plastic shear strain is the time integral of $\dot{\tilde{\gamma}}^p$:

$$\tilde{\gamma}^p = \int_0^t \dot{\tilde{\gamma}}^p(\varsigma)\, d\varsigma. \tag{54}$$

We can define an equivalent plastic strain γ^{p*} that can be positive or negative and which corresponds to τ^*. The quantities $\tilde{\gamma}^p$ and $\tilde{\gamma}^{p*}$ are plotted in Figure 35.

In Figure 34, the equivalent shear stress does not decrease to zero after the beginning of the analysis. However, it is clear from the shape of the curve that the shear stress τ^* changes sign, and this should occur where the plastic shear strain becomes approximately constant. The places where the plastic shear strain are constant coincide with local minima in the equivalent stress $\tilde{\tau}$. This implies that the time step of the finite element program was too large and the zero stress data points were missed by the analysis. Therefore, the minimum stress was assumed to be the point at which the change in sign of the stress τ^* occurred. The appropriate zero stress points were added to the plot in Figure 34. The result is shown in Figure 36.

Finally, if we cross-plot τ^* and γ^{p*}, we get the equivalent shear hysteresis loops shown in Figure 37. The shear strain range for each of these hysteresis loops is listed in Table 13.

4 Fatigue Test Method

4.1 Fixture Design

A double shear specimen was designed so that two solder joints were cast as the gage sections between pieces of a steel fixture. Photographs of completed specimens are shown in Figures 38 and 39, where the solder joints are indicated by arrows. The design considerations were: (1) the solder joints should have essentially homogeneous stress and strain fields; (2) there should be no backlash in the load train, caused either by the fixture or the grips; and (3) the solder joints should be large enough so that bulk properties are tested.

The homogeneous stress and strain fields in the solder joints have been obtained by choosing the dimensions of the solder joints appropriately. Constraints for the gage section dimensions for a double shear specimen for testing thin polymer sheets were given by G'Sell, Boni, and Shrivastava [32]. Here, where the solder joints are thick enough so that buckling is not a consideration, only two constraints need to be considered. They are: (1) the minimization of end effects and a better approximation of simple shear, and (2) the maximum load capacity of the testing machine. If we want to approximate simple shear and minimize end effects, then according to G'Sell,

Boni, and Shrivastava [32] we must have

$$\frac{L}{h} > 15, \tag{55}$$

where the dimensions L and h are defined in Figure 40. To satisfy the second condition, the maximum load necessary to apply the required shear stress must not be greater than the load capacity of the test machine, or

$$Le < \frac{F_{max}}{\tau_{max}}. \tag{56}$$

The dimension e is also defined in Figure 40. The maximum shear stress was estimated as approximately 10,000 psi from the previous tensile test results. The maximum load capacity of the testing machine is 20,000 pounds. After choosing the length L arbitrarily as 2 inches, equations 55 and 56 gave the upper bounds for h and e as

$$h < 0.133 \text{ inches, and} \tag{57}$$

$$e < 1 \text{ inch.} \tag{58}$$

The final values chosen for h and e were $h = .100$ inches and $e = .125$ inches, giving $L/h = 20$ and $Le = .5$.

To determine if the resulting stress field was approximately homogeneous, a crude finite element model of a solder joint with these dimensions was analyzed. A shear strain of 2% was applied at room temperature using the elasto-viscoplastic constitutive equations derived in Section 2. The deformed mesh with a displacement magnification of 10× is shown in Figure 41. No deformation was allowed in the 2-direction. the shear

stress was approximately *constant* 25.8 MPa, and accordingly there are no contours for σ_{12}. The stress contours for σ_{11} and σ_{22} are shown in Figures 42 and 43. Note that these stresses are zero everywhere except in the corners.

Mechanical drawings of the fixture and of the mold used to cast the solder joints are included in Appendix A.

Carbon steel was chosen as the material for the fixture. Because steel is not readily solderable, it was necessary to electroplate the parts of the fixture that were to be soldered. The upper half of the fixture is split in half to allow more uniform plating of these regions.

Extensometers can be mounted on the specimen by attaching adaptors to either of the two sets of threaded holes in the fixture. There are two sets of holes so that extensometers can be mounted on either side. With different adaptors, various sizes of either clip gages or extensometers can be used so that the most appropriate transducer may be chosen for each test.

4.2 Specimen Fabrication

After some experimentation with different plating materials, nickel plating covered by a layer of tin plating was found to form the best bond with the solder. Coincidentally, these are also the materials that are plated on to the end terminations of the chip capacitors, where the nickel is a diffusion barrier. In both cases, the tin retards oxidation of the nickel and therefore maintains the solderability of the nickel. The

total thickness of the plating on the shear fixture was less than .001 inches.

The plated areas of the fixture included the faces to be soldered and continue around the corners to the front and back of the fixture for an additional .050 inches. This ensures that the solder wets the entire face during casting. The edges of the nickel plating are visible in Figure 39 as the shiny bands along the edges of the solder joints. The tin plating on these regions was removed during the final polishing step.

The solder joints were cast in the following manner:

1. Solder was melted in a crucible and placed in a vacuum oven at approximately 260° C for at least 45 minutes to eliminate trapped air.

2. The individual pieces of the plated fixture were heated on a hot plate until the tin plating melted. This step allowed the organic additives from the plating bath to outgas before the solder joint was formed. The plating was covered with RA (activated rosin) flux during this time to prevent the formation of oxides. After the tin was reflowed, the flux residue was removed by soaking the pieces in flux thinner.

3. The pieces of the fixture were placed in the mold and clamped together. These clamps remained on the fixture until the beginning of the test to eliminate any straining of the solder joints. The fixture and the mold were heated on a hot plate until the tin plating melted. The plated area was kept covered with RA (rosin activated) flux during this procedure.

4. The molten solder was then removed from the vacuum oven and poured into the heated mold. The flux floated to the top of the joint when the solder was added; no contamination from the flux was found when the joints were later cross sectioned. The mold was designed with indentations below the solder joints so that bubbles formed by trapped gases could be removed by mechanically removing the affected solder without damaging the final specimen.

5. The specimen was then placed in a vacuum oven for 15 minutes at a temperature high enough to keep the solder molten so that any additional voids resulting from the casting process could be eliminated. After this step was added to the process, it was determined that the indentations in the mold were deeper than necessary since the vacuum removed almost all voids.

6. The fixture was removed from the oven and vibrated ultrasonically until solidification of the eutectic matrix occurred, which was necessary since otherwise the lead-rich dendrites were found only in the bottom of the joint. Explanations for this phenomenon and photographs showing the results of adding this step to the process will be discussed later. The time to complete solidification was between 4 minutes 30 seconds and 5 minutes.

7. The specimen was allowed to air cool to room temperature, which took approximately one hour and fifteen minutes.

8. Some specimens were later annealed at 170° C for varying amounts of time to

determine the effect on the microstructure.

9. Excess solder was mechanically removed until the edges of the solder joints were even with the top and bottom of the fixture. The solder joints were polished to a 600 grit finish before testing. The fixture was kept clamped together until it was mounted in the testing machine and was at zero load. This eliminated any straining of the solder joints prior to the test.

4.3 Microstructure

The microstructure of 60/40 tin-lead solder consists of a lead-rich phase dispersed in a tin-rich matrix. Since solder joints on electronic components are small, they solidify quickly and the microstructure is similar to a chill-cast structure. The eutectic composition of the tin-lead system is 61.9/38.1 tin-lead, and the excess lead forms lead-rich dendrites surrounded by a eutectic structure. Interdendritic spacing is often used as a measure of grain size in cast structures because grain boundaries are difficult to determine. Along with the distance between the lead-rich dendrites and their size, the structure of the eutectic matrix is also of interest. This matrix can have a lamellar structure or it may be composed of spheroidal lead-rich regions surrounded by the tin-rich phase. The phase size in chip capacitor joints can vary by approximately two orders of magnitude. The phase size is a function of the cooling rate which is determined by the soldering method. At the C. S. Draper Laboratory, visual comparison of SEM micrographs has been used to determine relative differences in

the microstructures resulting from different soldering methods.

Figures 44 and 45 are micrographs of a chip capacitor solder joint. These micrographs are backscatter electron images in which lighter areas represent materials with a higher atomic number. In this case, the lighter areas are the lead-rich phase and the darker regions are the tin-rich phase. The specimens were mounted in room temperature epoxy and metallographically polished, but they were not etched. This particular joint was soldered with a heater bar, which is a variation on a resistance welding technique. The joint has a more pronounced gradient of lead-rich dendrites than would be expected in a hand soldered joint. However, the phase sizes are within the expected range of microstructures for solder joints on electonic components.

The experimental goal of this part of the study was to make shear fatigue specimens with microstructures representative of those found in actual soldered connections. These specimens could then be used to address the effects of microstructure on fatigue behavior. The cooling rate of a joint in the shear fixture is much slower than that of a solder joint in an electronic assembly. This had to be taken into consideration when casting the joints in the shear fixture. The approach to controlling the microstructure of these joints is to vary the cooling rate to change the phase size and to adjust the heat treatment to homogenize any gradients of tin or lead.

In addition, there was the problem of lead-rich dendrites appearing only at the bottom of solder joint. Since these fatigue tests are to determine bulk properties, a homogeneous microstructure was considered desirable. Therefore, a method had to

be determined to obtain an even distribution of dendrites throughout the joint.

What is reported here is a preliminary attempt at investigating the techniques for obtaining the desired microstructures. Since a quick quench gives a finer microstructure, the mold was designed using a minimum of material. A water quench was attempted first. There were problems with this technique, however. When the hot mold and fixture were lowered into chilled water, steam entered the molten solder through the gap between the fixture and the mold and bubbled up through the solder. Therefore, an air quench was used for the next phase of testing. The time to solidification with this method was between 4 minutes 30 seconds and 5 minutes.

Five double shear specimens were manufactured by different processes to compare the resulting microstructures. This series of tests is summarized in Table 14, which also lists the specimen numbers for later use. Specimens were mounted for metallographic study using the procedure outlined for the chip capacitor solder joint above.

The fact that the lead-rich dendrites appeared only in the bottom of the solder joint could be caused by either a temperature gradient prior to solidification or it could be a phenomenon known as *gravity-induced segregation*. Gravity-induced segregation occurs when the density of the dendrites is significantly different than the density of the eutectic liquid in which they form. In the case of the 60/40 tin-lead, the dendrites are about 30% more dense than the eutectic liquid at 183° C. Reed-Hill [33] describes a similar phenomenon in the lead-antimony system in which the almost pure

antimony crystals rise to the top of a casting because their density is so much lower than the surrounding liquid. On the basis of this assumption, ultrasonic vibration during solidification was added to the process in an attempt to keep the dendrites from settling. A set of four specimens was used to determine the effects of ultrasonic vibration during cooling and the effects of an additional two hour heat treatment at 170° C after the specimen had been air cooled to room temperature.

Figures 46 and 47 compare two specimens, one of which was ultrasonically vibrated during solidification and one of which was not. Micrographs of these specimens at a higher magnification are on the following page. The specimen which was vibrated shows a reasonably uniform distribution of lead-rich dendrites, while the specimen which was not shows a uniform eutectic matrix. Without agitation, the dendrites sink to the bottom of the joint before the eutectic liquid solidifies. They are removed with the excess solder in the final polishing step of the manufacturing process. This hypothesis is substantiated by the micrograph shown in Figure 50, which shows a cross-section removed from a specimen which did not receive the final polishing step. The specimen with the evenly dispersed dendrites has a microstructure that is more representative of solder joints on electrical components and is therefore preferable.

Figures 51 through 54 compare the microstructures of two specimens which were ultrasonically vibrated but received different heat treatments. Both were air cooled to room temperature after casting, but one received a further two hour heat treatment at 170° C. Figures 55 through 60 compare the microstructures of the two specimens

that received no ultrasonic vibration as they solidified. Again, both were air cooled to room temperature and one had an additional heat treatment at 170° C for two hours. These comparisons show that the two hour heat treatment had no definitive effect on the phase size, and no discernible effect on the microstructure of these specimens.

In addition to this series of tests, another specimen was cast using the ultrasonic vibration technique and an additional heat treatment of 45 minutes at 170° C. Micrographs of this specimen are shown in Figures 61 through 63. Again, no effect of the heat treatment was observed.

4.4 Fatigue Testing

4.4.1 Experimental Procedure

All testing was done on an MTS 880 Servohydraulic Materials Test System. MTS 641 Hydraulic Grips were used to eliminate backlash in the load train. The clamps on the fixture were removed only after the specimen was mounted in the test machine and at zero load. The fixture is shown with these clamps in Figure 64.

The tests were run in total strain control with a ramp waveform and zero mean strain. The frequency was .1 Hz, which corresponds to the five second transfer time for the electronic assemblies during thermal cycling. The thermal expansion of the component and the board/frame assembly drive solder joint fatigue, applying a total shear strain to the solder joint. Therefore, testing was done with total shear strain as the controlling parameter. All of these preliminary tests were conducted at room

temperature.

For these initial tests, two mechanical failure criteria were chosen. These were (1) the formation of a crack .1 inches long, and (2) the formation of a crack .25 inches long. The cracks were observed through a microscope. Crack length was measured using scales with divisions in hundredths that were glued to the fixture beside the solder joints.

Four tests were successfully conducted. These had shear strain ranges of 1.5%, 2.0%, 2.5%, and 3.0%.

4.4.2 Results

Stable hysteresis loops were obtained after about 10 cycles in each test, although prior to that there was some shifting of the mean stress from zero. The hysteresis loop at cycle 10 and the final hysteresis loop of the test (when a crack of length .250" was detected) are plotted for each of these tests in Figures 65 to 68.

Cracks formed at the nickel-solder *interface* along the center portion of the fixture in all cases and they propagated along the interface for the duration of the test. This indicates that the interface was weaker than the solder joint. In actual chip capacitor solder joints, such interface cracks do not form during thermal cycling. Even though the plated materials were the same as those used on a chip capacitor, the plated area on the double shear fixture was much larger. Because of the size of the plated area, variations in the microchemistry are probable. In addition, because of edge

effects the thickness of the plating tends to decrease towards the edges. Variations in microchemistry and edge effects may have contributed to the weakness of the interface.

The stress ranges throughout the tests were examined to determine if a load drop could be used as an alternate failure criterion. These are plotted in Figures 69 through 72. Although the shape of the hysteresis loops changed as the cracks grew, there was no apparent relationship between load drop and crack length.

A monotonic shear test was also conducted to determine an effective shear modulus. This modulus also included the elastic deformation of the fixture that was measured by the extensometer. Using this estimate, plastic strains for the stable hysteresis loops were calculated so that comparisons could be made to the results of the finite element analysis. The shear stress versus plastic shear strain curves are shown in Figures 73 to 76.

The results of the monotonic shear test were also used as a fatigue data point at 1/4 cycle. The stress-strain curve for this test is plotted in Figure 77. The cracks in this specimen propagated so quickly that the strain level at which a crack of .100" could be detected could not be measured with the current procedure. For the fatigue-life curves, it was assumed that the plastic strain level was the same for both crack lengths in the quarter cycle test.

The fatigue-life data is summarized in Table 15. The data was fit to the Coffin-Manson Law:

$$\left(\frac{\Delta\gamma^p}{2}\right) = \gamma_f{}'\,(2N_f)^c. \tag{59}$$

For the .100" crack length, the results were

$$\gamma_f{}' = 0.060 \text{ and} \tag{60}$$

$$c = -0.361, \tag{61}$$

and for the .250" crack length,

$$\gamma_f{}' = 0.059 \text{ and} \tag{62}$$

$$c = -0.320. \tag{63}$$

The regression coefficients for these curve fits were 97.90% and 96.52%, respectively. The shear fatigue ductility γ_f' is a material parameter and should be approximately equal to the monotonic shear ductility, which is .075. The values for the fatigue ductility exponent c found here are lower than the range of typical values for most metals, which is between -.5 and -.7. The fatigue-life curves for these failure criteria are plotted in Figures 78 and 79.

5 Discussion

Finally, the Coffin-Manson equations may be used to estimate the life of the solder joint in the modelled electronic assembly from Section 2. The plastic strain amplitude in the third hysteresis loop was 4.305×10^{-2}. This gives an estimate of approximately 9 cycles until a crack length of .100 inches is reached, and of approximately 12 cycles

until the formation of a crack of length .250 inches. This estimate does not include any effects of the mean plastic strain. These estimates are much lower than what has been found so far in the thermal cycle testing being done at the C. S. Draper Laboratory. In these tests, crack initiation often begins by 50 thermal cycles. Cracks are established by 200 cycles and they are on the order of 50 microns long. Testing is being conducted to 1000 thermal cycles, but no data beyond 200 thermal cycles is yet available. However, it is clear that the fatigue data from the double shear tests has strongly underestimated the life of such a solder joint in thermal fatigue. This is not surprising given the interface failures of these specimens.

6 Conclusions and Recommendations

Here, bulk properties of solder have been used to determine the plastic strain levels in a chip capacitor solder joint. A continuum analysis such as this is valid if there are approximately 10 phase boundaries across the thinnest portion of the material. A micrograph of the thinnest region of the solder joint is shown in Figure 80. The number of phase boundaries across this area is between 8 and 10, making this a borderline case for the use of a continuum analysis. However, this joint has a very small standoff height compared to other types of solder joints, so this may be regarded as a worst case.

In this work, material constants and constitutive functions were determined for an elasto-perfectly viscoplastic constitutive model of 60/40 tin-lead solder for tempera-

tures between -55° C and 125° C and for strain rates between 8.33×10^{-5} and $8.33 \times 10^{-2}\ s^{-1}$. Elastic moduli were calculated from single crystal constants of tin and lead, thus avoiding the problems inherent in conducting tensile tests on materials at high homologous temperatures. The constitutive model for the viscoplastic behavior is a hyperbolic sine function which fits the data over a range of temperature more than twice as large as any we found in the literature and over three orders of magnitude of strain rate. The strain rate sensitivity and the activation energy which were found compared favorably to results in the literature. This model adequately predicted both the strain rate dependence and the temperature dependence of the alloy.

Using finite element methods and this constitutive model, an estimate of the plastic strain levels in a representative solder joint during thermal cycling was obtained. This showed high strains in the solder below the component and relatively low strains in the remainder of the joint. The mean plastic shear strain at an integration point in the high strain region was approximately 6.1%, with the plastic shear strain ranges of the hysteresis loops varying between 3.9% and 4.3%. This estimate should be considered approximate because of the relatively coarse mesh used in the solder joint. In addition, the geometry of the mesh at the end of the joint below the chip capacitor was not accurate, and this area is where cracks form during thermal cycling. The estimates given above are for a region of the solder far enough away from this edge that effects of the difference in geometry are not included in the results. However, the plastic strain levels may be higher than reported at this edge.

Shear fatigue test specimens were designed and preliminary fatigue tests were conducted. However, failure occurred at the interface between the plating and the solder joint. A specimen in which failure occurs in the solder is essential for the use of this methodology in determining the fatigue life of these joints. However, with the current specimen much has been learned about microstructures and casting techniques that will aid in future work. In addition, the analysis of the solder joint shows the strain range in which testing should be conducted and indicates the need to determine the effects of the mean plastic strain on the life of such solder joints.

In future work, it is recommended that the following steps be taken:

- Perform constant true strain rate tests to determine more accurate viscoplastic constitutive equations, which also model the strain hardening behavior of the material.

- Conduct the numerical analysis using a more refined and more accurate mesh for the solder joint to determine the stress and strain levels in the area where cracks appear during thermal cycling.

- Numerically perform a thermal analysis of the electronic assembly to determine its actual temperature history during thermal cycling and couple this with a mechanical analysis.

- Conduct finite element analyses on solder joints of different geometries to compare alternate reflow soldering processes (i.e. manual, heater bar, and vapor

phase soldering).

- Determine the cause of the interfacial failure problem in the double shear test and design a test specimen in which it can be avoided.

- Conduct shear fatigue tests on solder joints of various thicknesses down to approximately .001 inch in thickness.

- Perform these fatigue tests not only at room temperature but at other temperatures between -20° C and 100° C. Obtain more data points on the plastic strain amplitude versus number of reversals curve and also determine the effect of the frequency of cycling.

References

[1] Wild, R. N., "Some Fatigue Properties of Solders and Solder Joints", IBM No. 74Z000481, 1975.

[2] Anand, L., Lush, A., Briceno, M., and Parks, D., "A Time-Integration Procedure for a Set of Internal Variable Type Elasto-viscoplastic Constitutive Equations", M.I.T. Report of Research in Mechanics of Materials, Sept., 1985.

[3] ABAQUS Version 4.5.159, Hibbit, Karlsson, and Sorensen, Inc. Providence, R.I.

[4] Anand, L., "Constitutive Equations for the Rate-Dependent Deformation of Metals at Elevated Temperatures," *ASME Journal of Engineering Materials and Technology*, Vol. **104**, pp. 12-17, 1982.

[5] Anand, L., "Constitutive Equations for the Hot-Working of Metals",*International Journal of Plasticity*, Vol. **1**, pp. 213-231, 1985.

[6] Gurtin, M., *An introduction to Continuum Mechanics*, Academic Press, New York, 1981.

[7] "Development of Highly Reliable Soldered Joints for Printed Circuit Boards", Westinghouse Defence and Space Center, Contract NAS8-21233, August, 1968.

[8] Rhode, R. W., and Swearengen, J. C., "Deformation Modeling Applied to Stress Relaxation of Four Solder Alloys", *Journal of Engineering Materials and Tech-*

nology, Vol. **102**, pp. 207-214, April, 1980.

[9] Dunn, B. D., "The Properties of Near-Eutectic Tin/Lead Solder Alloys Tested Between +70° and -60° C and the use of Such Alloys in Spacecraft Electronics", European Space Agency, Technical Memorandum ESA TM-162 (ESTEC), Sept., 1975.

[10] Hashin, Z., and Shtrickman, S., "A Variational Approach to the Theory of the Elastic Behavior of Multiphase Materials," *J. Mech. Phys. Solids*, Vol. **11**, pp. 127-140, 1963.

[11] Hellwege, K.-H., ed. *Landolt-Börnstein, Numerical Data and Functional Relationships in Science and Technology, Group III: Crystal and Solid State Physics*, Vol. **11**, p. 113 and p. 203, Springer-Verlag, 1979.

[12] Kammer, E. W., Cardinal, L. C., Vold, C. L., and Glicksman, M. E., "The Elastic Constants for Single-Crystal Bismuth and Tin from Room Temperature to the Melting Point", *J. Phys. Chem. Solids*, Vol **33**, pp. 1891-1898, 1972.

[13] Hellwege, K.-H., ed. *Landolt-Börnstein, Numerical Data and Functional Relationships in Science and Technology, Group III: Crystal and Solid State Physics*, Vol. **11**, p. 60 and p. 97, Springer-Verlag, 1979.

[14] Simmons, G., and Wang, H., *Single Crystal Elastic Constants and Calculated Aggregate Properties: A Handbook*, 2nd Edition, M.I.T. Press, 1971.

[15] Barry, B. T. K., and Thwaites, C. J., *Tin and its Alloys and Compounds*, Ellis Horwood Limited, Chichester, West Sussex, England, 1983.

[16] Getzan, G., unpublished work, The C. S. Draper Laboratory, Inc., Cambridge, MA.

[17] Zener, C., and Hollomon, J. H., "Effect of Strain Rate Upon Plastic Flow of Steel", *Journal of Applied Physics*, Vol. **15**, pp. 22-32, 1944.

[18] Sellars, C. M., and Tegart, W. J. McG., "Hot Workability", *International Metallurgical Reviews*, Vol. **17**, pp. 1-24, 1972.

[19] IMSL edition 9.2, IMSL, Inc., Houston, Texas, 1984

[20] Mohammed, F. A., and Langdon, T. G., "Creep Behavior in the Superplastic Pb-62% Sn Eutectic," *Phil. Mag.*, Vol. **32**, pp. 611-614, 1975.

[21] Schneibel, J. H., and Hazzledine, P. M., "The Role of Coble Creep and Interface Control in Superplastic Sn-Pb Alloys," *Journal of Material Science*, Vol. **18**, pp. 53-58, 1983.

[22] Kashyap, B. P., and Murty, G. S., "Superplastic Behavior of the Sn-Pb Eutectic in the As-Worked State," *Metallurgical Transactions A*, Vol. **13A**, pp. 53-58, 1982.

[23] Pink, E., Kutschej, R., and Stuewe, H. P., "Evidence for Lattice-Diffusion Controlled Superplasticity in a Sn-Pb Eutectic," *Scripta Metallurgica*, Vol. **15**, pp.

185-189, 1981.

[24] Murty, G. S., "Stress Relaxation in Superplastic Materials", *Journal of Materials Science*, Vol. 8, pp. 611-614, 1973.

[25] Baker, E., "Stress Relaxation in Tin-Lead Solders", *Materials Science and Engineering*, Vol. 38, pp. 241-247, 1979.

[26] Safranek, W. H., *The Properties of Electrodeposited Metals and Alloys, A Handbook, Second Edition*, American Elsevier Publishing Company, Inc., New York, 1986.

[27] *A.S.M. Metals Handbook, Ninth Edition*, Vol. 2, pp. 115-116.

[28] Fallon, L., "Analytical Study of Thermal Shock of an A-sized Chip Capacitor", C. S. Draper Intralab Memorandum, 4/19/85

[29] Blanchet, D., "3-Dimensional Thermal Stress Analysis of a Ceramic Chip Capacitor Mounted on a G10 MLB/Aluminum Module Frame", C. S. Draper Intralab Memorandum # DB:81:16, 2/6/81.

[30] Adams, P., "Final Results of Modulus Testing of PWB Materials", C. S. Draper Intralab Memorandum, 8/22/83.

[31] *A.S.M. Metals Handbook, Ninth Edition*, Vol. 2., p. 621.

[32] G'Sell, C., Boni, S., and Shrivastava, S., "Application of the Plane Simple Shear Test for Determination of the Plastic Behavior of Solid Polymers at Large Strains", *Journal of Materials Science*, Vol. **18**, pp. 903-918, 1983.

[33] Reed-Hill, R. E., *Physical Metallurgy Principles, Second Ed.*, Litton Educational Publishing, Inc., 1973.

A Mechanical Drawings of Double Shear Test Fixture

MATERIAL: 1018 CR STEEL.
MAKE 20.

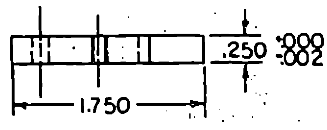

NOTE: ALL TOLERANCES NOT OTHERWISE SPECIFIED ARE ±.003

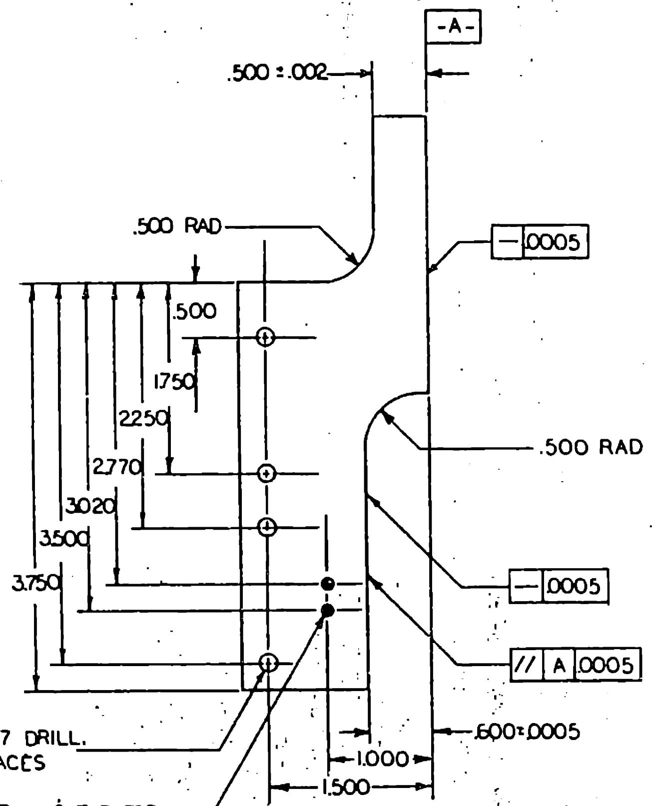

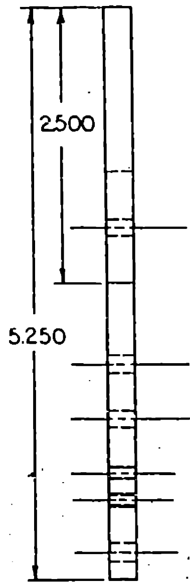

DOUBLE SHEAR FIXTURE		
SCALE: 1:1	9-23-85	PAM ADAMS

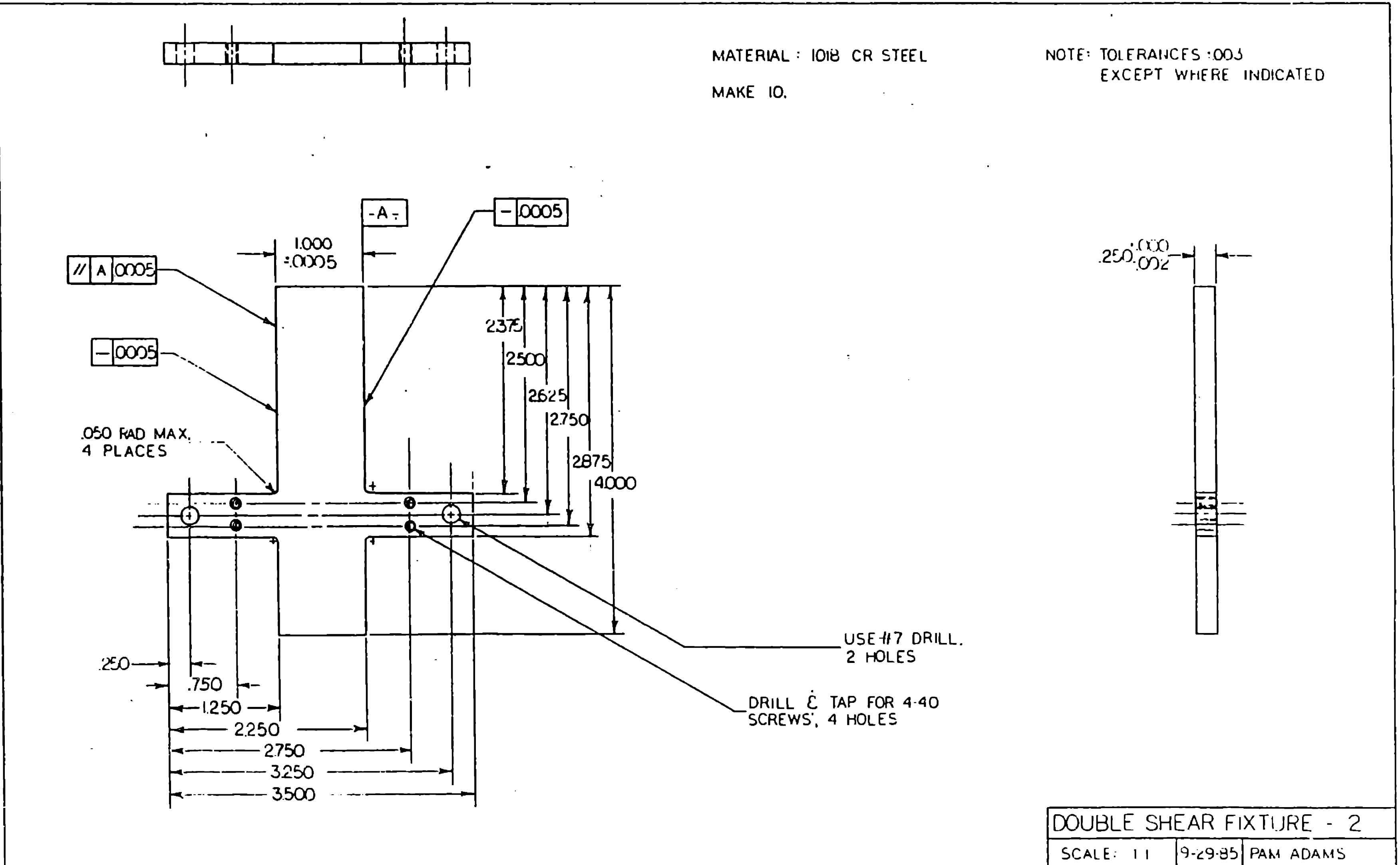
MATERIAL : 1018 CR STEEL
MAKE 10.
NOTE: TOLERANCES ±.003
EXCEPT WHERE INDICATED
-A-
// A .0005
— .0005
— .0005
1.000
±.0005
.050 RAD MAX.
4 PLACES
2.375
2.500
2.625
2.750
2.875
4.000
.250
.750
1.250
2.250
2.750
3.250
3.500
USE #7 DRILL.
2 HOLES
DRILL & TAP FOR 4-40
SCREWS, 4 HOLES
.250 +.000 -.002
DOUBLE SHEAR FIXTURE - 2
SCALE: 1:1
9-29-85
PAM ADAMS

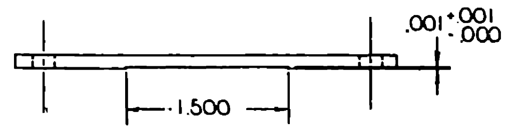

MATERIAL: 1018 CR STEEL.
MAKE 2.

NOTE: ALL TOLERANCES ±.003
UNLESS OTHERWISE INDICATED.

NOT TO SCALE.

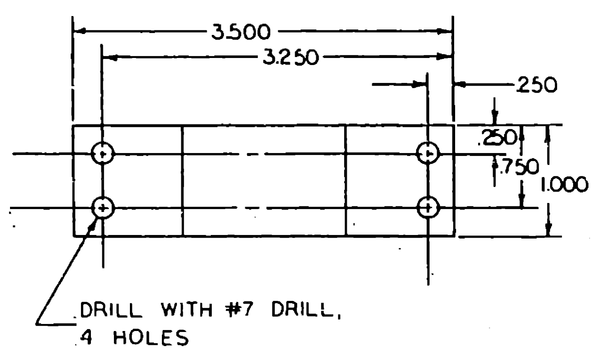

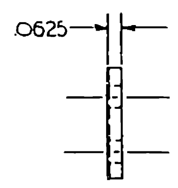

SHEAR FIXTURE GUIDE		
SCALE: 1:1	9-25-85	PAM ADAMS

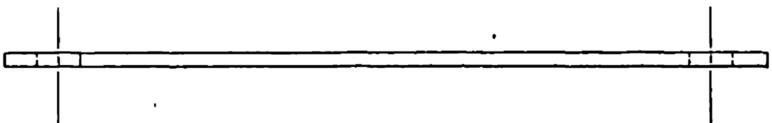

NOTE: TOLERANCES ±.003

MATERIAL: 1018 CR STEEL

MAKE 10

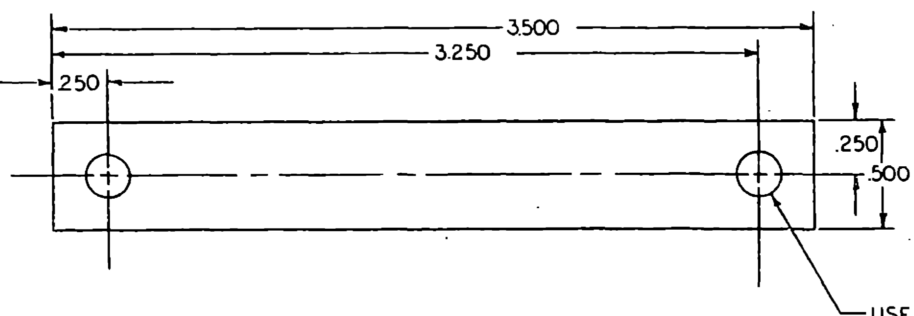

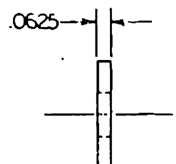

SHEAR FIXTURE TOP BRACE		
SCALE: 2:1	9-26-85	PAM ADAMS

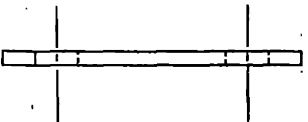

NOTE: TOLERANCES ±.003

MATERIAL: 1018 CR STEEL

MAKE 20

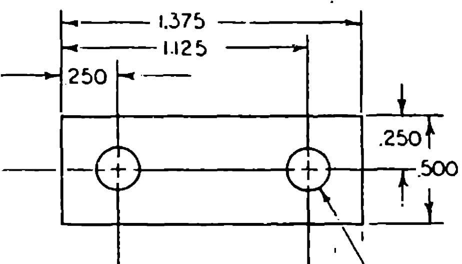

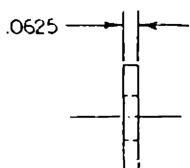

SHEAR FIXTURE LOWER BRACE		
SCALE: 2:1	9 26 85	PAM ADAMS

.1875
.325
.4375
.0625
DRILL & TAP FOR
4-40 SCREWS, 1/4" DEEP
8 PLACES
1.250
.125
1.500
.250
±.001
.247
±.001
3.250
5.250
MAKE 2 SLOTS,
.125 WIDE, .020 DEEP
.200
1.300
MATERIAL: STAINLESS STEEL,
ANY TYPE
MAKE 1.
NOTE: ALL TOLERANCES ±.003
EXCEPT WHERE
INDICATED
.3125
.125
.350
.750
.950
1.6875
2.3125
MAKE SLOT .080" DEEP
5.500
6.300
7.250
6.500
6.900
DRILL & TAP
FOR 4-40 SCREWS,
1/4" DEEP, 2 PLACES
DRILL & TAP
FOR 4-40 SCREWS,
4 PLACES
MOLD BASE
SCALE: 1:1
9-17-85
PAM ADAMS

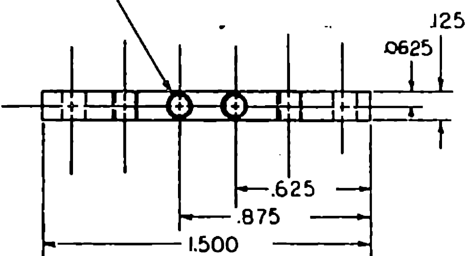

MATERIAL: STAINLESS STEEL,
ANY TYPE

NOTE: TOLERANCES ±.003

MAKE 1.

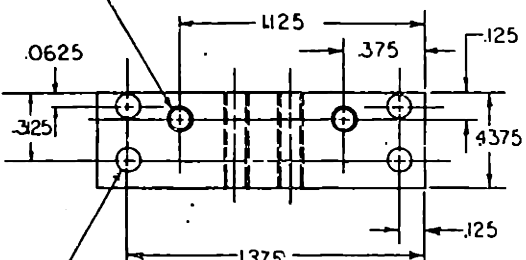

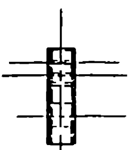

MOLD END 1		
SCALE: 2:1	9-16-85	PAM ADAMS

DRILL & TAP FOR
4-40 SCREWS,
2 PLACES

MATERIAL: STAINLESS STEEL,
ANY TYPE

NOTE: TOLERANCES ±.003

MAKE 1.

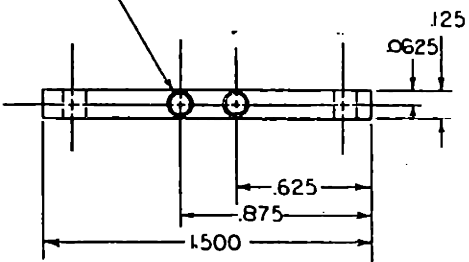

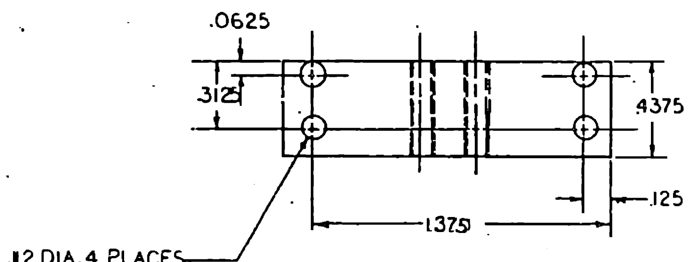

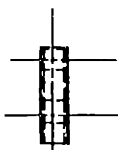

MOLD END 2		
SCALE: 2:1	9-16-85	PAM ADAMS

MATERIAL: STAINLESS STEEL,
ANY TYPE

MAKE 1 EACH.

NOTE: TOLERANCES ±.003

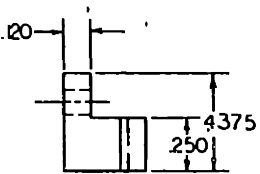

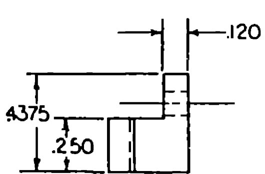

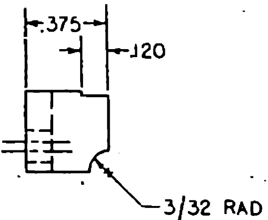

.125
.230
.270
.375
SLOT .120 WIDE

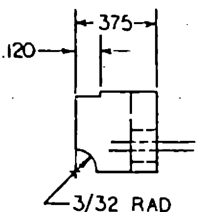

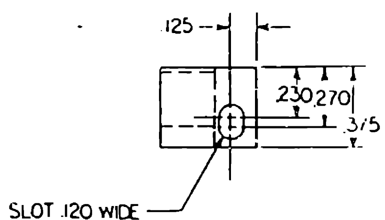

LOWER CLAMPS		
SCALE: 2:1	9-29-85	PAM ADAMS

MATERIAL: STAINLESS STEEL,
ANY TYPE

MAKE 1.

NOTE: TOLERANCES $^{+.000}_{-.001}$

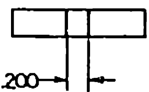

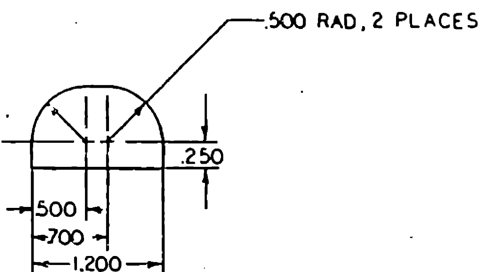

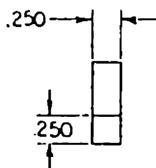

SPACER		
SCALE: 1:1	9-29-85	PAM ADAMS

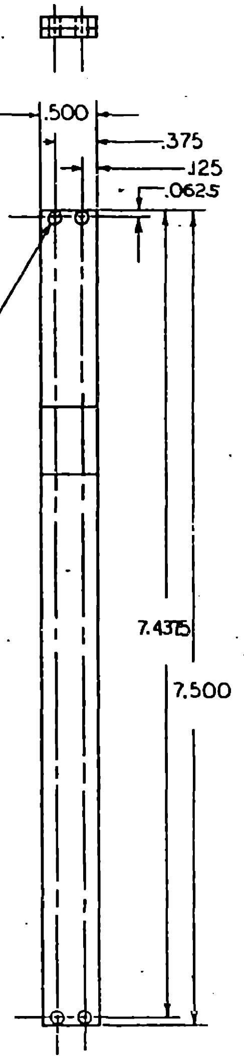

MATERIAL: STAINLESS STEEL,
ANY TYPE

NOTE: ALL TOLERANCES ±.003

MAKE 1.

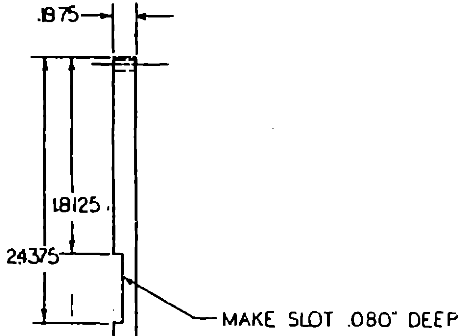

MOLD TOP		
SCALE: 1:1	9-14-85	PAM ADAMS

List of Tables

1 Tin Single Crystal Constants 65

2 Bounds for the elastic constants of tin 65

3 Single Crystal Elastic Constants for Lead 66

4 Calculated Elastic Constants for Lead 66

5 Hashin-Shtrickman bounds for elastic constants of the tin-rich phase (97.5 wt.% tin) 67

6 Hashin-Shtrickman bounds for elastic constants of the lead-rich phase (81.0 wt.% lead) 67

7 Hashin-Shtrickman bounds for the elastic constants of 60/40 tin-lead solder 68

8 Final values of the bulk and shear moduli of 60/40 tin-lead solder . . . 69

9 Test Matrix for Tensile Tests 69

10 Reported Values of Activation Energy 69

11 Reported Values of Strain Rate Sensitivity 70

12 Material Properties Used in Finite Element Model 70

13 Plastic shear strain ranges of the hysteresis loops 70

14 Test matrix for casting experiments listing specimen numbers 71

15 Fatigue-life data from double shear tests 71

T(C)	C_{11}(GPa)	C_{12}(GPa)	C_{13}(GPa)	C_{33}(GPa)	C_{44}(GPa)	C_{66}(GPa)
-130	79.75	58.77	39.59	99.28	24.82	26.49
-55	76.62	59.26	39.36	95.13	23.43	25.21
-35	75.79	59.39	39.29	94.03	23.05	24.86
-15	74.95	59.52	39.23	92.92	22.68	24.52
5	74.12	59.66	39.17	91.82	22.31	24.18
22	73.41	59.77	39.12	90.88	21.99	23.89
50	70.83	58.52	37.46	86.65	21.37	23.51
75	69.51	58.54	37.52	85.11	20.78	22.96
100	68.18	58.56	37.58	83.57	20.18	22.40
125	66.86	58.58	37.65	82.03	19.58	21.84
150	65.53	58.59	37.71	80.51	18.98	21.27

Table 1: Tin Single Crystal Constants

T(C)	μ_V(GPa)	μ_R(GPa)	κ_V(GPa)	κ_R(GPa)
-130	23.28	20.22	59.41	59.41
-55	21.77	18.13	58.27	57.26
-35	21.37	17.54	57.95	57.95
-15	20.97	16.93	57.64	57.64
5	20.56	16.31	57.34	57.33
22	20.22	15.76	57.08	57.07
50	19.57	14.80	55.02	54.98
75	18.94	13.79	54.59	54.54
100	18.30	12.71	54.15	54.10
125	17.66	11.56	53.73	53.67
150	17.02	10.30	53.29	53.23

Table 2: Bounds for the elastic constants of tin

T(C)	C_{11}(GPa)	C_{12}(GPa)	C_{44}(GPa)
-130	52.17	43.22	17.26
-55	50.96	42.69	16.07
-35	50.44	42.38	15.76
-15	49.91	42.06	15.45
5	49.38	41.75	15.14
22	48.93	41.48	14.88
50	48.19	41.04	14.44
75	47.54	40.64	14.05
100	46.88	40.25	13.67
125	46.22	39.86	13.28
150	45.56	39.46	12.89

Table 3: Single Crystal Elastic Constants for Lead

T(C)	μ_H(GPa)	μ_S(GPa)	κ(GPa)
-130	10.81	9.65	46.20
-55	10.05	8.95	45.45
-35	9.84	8.75	45.06
-15	9.63	8.55	44.68
5	9.42	8.35	44.29
22	9.25	8.18	43.96
50	8.95	7.90	43.42
75	8.69	7.64	42.94
100	8.43	7.39	42.46
125	8.17	7.14	41.98
150	7.90	6.88	41.50

Table 4: Calculated Elastic Constants for Lead

T(C)	κ_U^*(GPa)	κ_L^*(GPa)	μ_U^* (GPa)	μ_L^*(GPa)
-130	59.16	59.15	23.02	21.82
-55	58.02	58.01	21.53	20.39
-35	57.70	57.69	21.13	20.00
-15	57.39	57.38	20.73	19.61
5	57.08	57.07	20.33	19.22
22	56.82	56.81	19.99	18.89
50	54.76	54.76	19.35	18.26
75	54.32	54.32	18.73	17.64
100	53.88	53.88	18.10	17.02
125	53.45	53.44	17.46	16.40
150	53.01	53.00	16.83	15.78

Table 5: Hashin-Shtrickman bounds for elastic constants of the tin-rich phase (97.5 wt.% tin)

T(C)	κ_U^*(GPa)	κ_L^*(GPa)	μ_U^* (GPa)	μ_L^*(GPa)
-130	49.21	49.12	13.41	11.98
-55	48.36	48.27	12.50	11.14
-35	47.98	47.89	12.25	10.90
-15	47.60	47.51	12.00	10.65
5	47.23	47.13	11.75	10.42
22	46.91	46.82	11.54	10.21
50	46.05	45.98	11.18	9.86
75	45.57	45.50	10.85	9.54
100	45.09	45.02	10.51	9.22
125	44.61	44.54	10.18	8.91
150	44.13	44.06	9.85	8.58

Table 6: Hashin-Shtrickman bounds for elastic constants of the lead-rich phase (81.0 wt.% lead)

T(C)	κ_U(GPa)	κ_L(GPa)	μ_U (GPa)	μ_L(GPa)
-130	54.96	54.82	18.74	17.17
-55	53.94	53.81	17.51	16.01
-35	53.60	53.46	17.18	15.69
-15	53.24	53.11	16.84	15.36
5	52.90	52.76	16.51	15.04
22	52.61	52.47	16.23	14.77
50	51.09	50.98	15.71	14.27
75	50.63	50.51	15.22	13.80
100	50.16	50.05	14.72	13.32
125	49.70	49.59	14.22	12.84
150	49.24	49.12	13.73	12.36

Table 7: Hashin-Shtrickman bounds for the elastic constants of 60/40 tin-lead solder

T(C)	κ(GPa)	μ(GPa)
-55.	53.87	17.75
-35.	53.53	17.32
-15.	53.17	16.88
5.	52.83	16.32
22.	52.54	15.87
50.	51.03	15.14
75.	50.57	14.39
100.	50.10	13.38
125.	49.65	12.49

Table 8: Final values of the bulk and shear moduli of 60/40 tin-lead solder

	TEMP (C)								
STRAIN RATE (s^{-1})	-55	-35	-15	5	22	50	75	100	125
8.33×10^{-2}					X				
1.67×10^{-2}	X		X		X		X		X
8.33×10^{-3}					X				
1.67×10^{-3}	X	X	X	X	X	X	X	X	X
8.33×10^{-4}					X				
1.67×10^{-4}	X		X		X		X		X
8.33×10^{-5}					X				

Table 9: Test Matrix for Tensile Tests

Q($\frac{KJ}{mol}$)	$\dot{\epsilon}(s^{-1})$	θ(K)	ALLOY tin/lead	REFERENCES
84	1.7×10^{-7}-1.7×10^{-5}	336-422	62/38	Mohammed & Langdon [20]
57	1.7×10^{-5}-1.7×10^{-2}	336-442	62/38	Mohammed & Langdon [20]
55	$10^{-7} - 10^{-3}$	298	61.9/38.1	Schneibel & Hazzledine [21]
44.7	$10^{-7} - 10^{-2}$	298-408	61.9/38.1	Kashyap & Murty [22]
81.1	$10^{-7} - 10^{-2}$	408-443	61.9/38.1	Kashyap & Murty [22]
42	$10^{-6} - 1$	323-413	62/38	Pink, Kutschej, & Stuewe [23]
92.5	$10^{-6} - 1$	443-453	62/38	Pink, Kutschej, & Stuewe [23]
67	$7 \times 10^{-8} - 10^{-9}$	311-363	63/37	Baker [25]
57.32	8.3×10^{-5}-8.3×10^{-2}	218-398	60/40	This work

Table 10: Reported Values of Activation Energy

m	$\dot{\epsilon}(s^{-1})$	θ (K)	ALLOY tin/lead	REFERENCES
0.4	$2.x10^{-7}$-$2.x10^{-4}$	293	61.9/38.1	Murty [24]
0.61	$1.7x10^{-7}$-$1.7x10^{-5}$	336-442	62/38	Mohammed & Langdon [20]
0.33	$1.7x10^{-5}$-$1.7x10^{-2}$	336-442	62/38	Mohammed & Langdon [20]
0.294	$7x10^{-8}$-10^{-9}	311-363	63/37	Baker [25]
0.417	$10^{-10} - 10^{-9}$	298	62.9/38.1	Schneibel & Hazzledine [21]
0.48	$10^{-5} - 1.$	323-413	62/38	Pink, Kutschei, & Stuewe [23]
0.58	$10^{-5} - 1.$	443-453	62/38	Pink, Kutscheh, & Stuewe [23]
0.4118	$8.3x10^{-5}$-$8.3x10^{-2}$	218-398	60/40	This work

Table 11: Reported Values of Strain Rate Sensitivity

	Properties			
Material	E (GPa)		ν	α (1/°C)
6061-T6 Aluminum	68.3 [27]		.34 [27]	$23.6x10^{-6}$ [27]
Copper	110. [26]		.345	$18.9x10^{-6}$ [26]
Metallization	71.0 [28]		.38 [28]	$17x10^{-6}$ [28]
Ceramic	172.		.25	$9.85x10^{-6}$ [29]
Polyimide	E(GPa)	T(C)		
-Glass	34.7 [30]	-55		
Board	34.7 [30]	-25		
	34.2 [30]	0	.3	$17x10^{-6}$ [28]
42.45 wt.%	33.5 [30]	24		
resin	32.0 [30]	100		
content	31.8 [30]	125		
60/40 tin-lead				$26.x10^{-6}$ [31]

Table 12: Material Properties Used in Finite Element Model

Hysteresis Loop	Plastic Shear Strain Range
1	$3.896x10^{-2}$
2	$4.208x10^{-2}$
3	$4.305x10^{-2}$

Table 13: Plastic shear strain ranges of the hysteresis loops

	ultrasonic vibration	no ultrasonic vibration
no additional heat treatment	# 860327	# 860302
2 hrs. at 170° C	# 860312	# 860305
45 min. at 170° C	# 860406	

Table 14: Test matrix for casting experiments listing specimen numbers

$\Delta\gamma$ (%)	$\Delta\gamma^p$(%)	N_f (.100")	N_f (.250")
1.50	.73	638	1325
2.00	.98	540	2190
2.50	1.32	241	287
3.00	1.72	229	504
14.98	14.94	.25	.25

Table 15: Fatigue-life data from double shear tests

List of Figures

1 Chip capacitors mounted on a double-sided test board used for thermal cycle testing. 78

2 Schematic of cross-sectioned electronic assembly 79

3 Some published values of the Young's modulus for near-eutectic tin-lead solders. 80

4 Bounds for the elastic moduli of tin 81

5 Bounds for the elastic moduli of lead 82

6 Tin-Lead Phase Diagram, from Barry and Thwaites [15] 83

7 SEM micrograph of 60/40 tin-lead solder; magnification 1000×. 83

8 Young's Modulus of Near-Eutectic Tin-Lead 84

9 Results of the calculations of the shear and bulk moduli of 60/40 tin-lead solder. 85

10 Strain rate dependence of stress-strain curves for 60/40 tin-lead solder at 22 C 86

11 Temperature dependence of stress-strain curves for 60/40 tin-lead solder at 1.67x10^{-2} s^{-1} 87

12 Temperature dependence of stress-strain curves for 60/40 tin-lead solder at 1.67x10^{-3} s^{-1} 88

13 Temperature dependence of stress-strain curves for 60/40 tin-lead solder at 1.67×10^{-4} s^{-1} 89

14 Fit of the stress-strain data to the hyperbolic sine model 90

15 Comparison between the model and the data at 125 C 91

16 Comparison between the model and the data at 75 C 92

17 Comparison between the model and the data at 22 C 93

18 Comparison between the model and the data at 22 C 94

19 Comparison between the model and the data at -15 C 95

20 Comparison between the model and the data at -55 C 96

21 Comparison between the model and the data at 1.67×10^{-3} s^{-1} 97

22 Cross-sectioned capacitor mounted on a board. 98

23 SEM micrograph of the solder joint on the right side of the capacitor shown above at a magnification of 50x 99

24 Micrograph of a cross-sectioned chip capacitor after 200 thermal cycles. 99

25 SEM micrograph of the cracked solder joint shown in the above photograph. 100

26 An actual thermal cycle showing the difference between the ambient temperature and the temperature of the assembly. 100

27 Temperature history input 101

28 Finite element mesh of electronic assembly 102

29 Finite element mesh of solder joint 103

30 Equivalent plastic shear strain contours in the solder joint 104

31 Equivalent plastic shear strain contours in the solder joint under the chip capacitor 104

32 Equivalent plastic shear strain contours in solder joint under the chip capacitor, leftmost eight elements 105

33 Data from the integration point shown in the contour plot of equivalent plastic strain. 106

34 Equivalent stress-strain curve 107

35 Comparison of the equivalent plastic shear strain and the signed equivalent plastic shear strain. 108

36 Equivalent stress-strain curve with added data points at zero stress . 109

37 Hysteresis loops for an integration point in the solder joint during thermal cycling. 110

38 View of specimen showing placement of extensometer 111

39 Front view of specimen ready for testing 112

40 Definition of the reference axes and dimensions of a parallelopedic piece of material deformed in simple shear, from Ref. [30]. 113

41 Deformed shear mesh 113

42 σ_{11} contours 114

43 σ_{22} contours 114

44 SEM micrograph of the solder joint shown in Figure 21 at 253×. . . . 115

45 Same solder joint as shown above; the magnification is 500×. 115
46 Specimen #860312, magnification 25.2× 116
47 Specimen #860305, magnification 19.8×. 117
48 Specimen #860312, magnification 127×. 118
49 Specimen #860305; magnification 125×. 118
50 Specimen #860206; magnification 15.2×. 119
51 Specimen #860327; air cooled; magnification 250×. 120
52 Specimen #860312; air cooled followed by 2 hours at 170° C; magnification 250×. 120
53 Specimen #860327; air cooled; magnification 1000×. 121
54 Specimen #860312; air cooled followed by 2 hours at 170° C; magnification 1000×. 121
55 Specimen #860302; air cooled. The magnification is 200×. 122
56 Specimen #860305; air cooled followed by 2 hours at 170° C. The magnification is 200×. 122
57 Specimen #860302; air cooled. The magnification is 500×. 123
58 Specimen #860305; air cooled followed by 2 hours at 170° C. The magnification is 500×. 123
59 Specimen #860302; air cooled. The magnification is 1000×. 124
60 Specimen #860305; air cooled followed by 2 hours at 170° C. The magnification is 1000×. 124

61 Specimen #860406; air cooled followed by 45 minutes at 170° C. The magnification is 200×. 125

62 Specimen #860406; magnification 500×. 125

63 Specimen #860406; magnification 1000×. 126

64 Fixture with clamps to keep solder joints from being strained before testing. 127

65 Hysteresis loops, shear strain range 3.0% 128

66 Hysteresis loops, shear strain range 2.5% 129

67 Hysteresis loops, shear strain range 2.0% 130

68 Hysteresis loops, shear strain range 1.5% 131

69 Stress range variation during the test, shear strain range 3.0% 132

70 Stress range variation during the test, shear strain range 2.5% 133

71 Stress range variation during the test, shear strain range 2.0% 134

72 Stress range variation during the test, shear strain range 1.5% 135

73 Plastic strain hysteresis loop, cycle 10, shear strain range 3.0% 136

74 Plastic strain hysteresis loop, cycle 10, shear strain range 2.5% 137

75 Plastic strain hysteresis loop, cycle 10, shear strain range 2.0% 138

76 Plastic strain hysteresis loop, cycle 10, shear strain range 1.5% 139

77 Stress-strain curve from monotonic shear test. 140

78 Shear fatigue life curve for a .100" crack 141

79 Shear fatigue life curve for a .250" crack 141

80 Thinnest section of solder joint 142

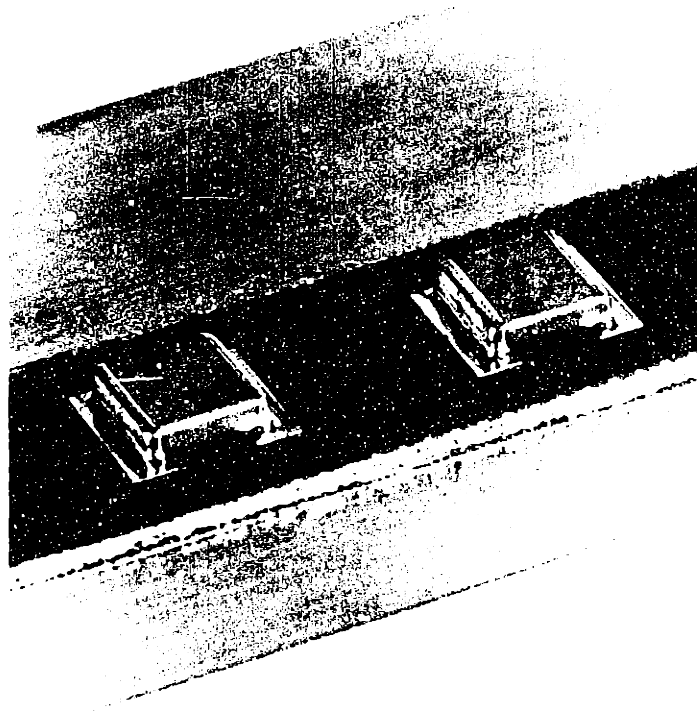

Figure 1: Chip capacitors mounted on a double-sided test board used for thermal cycle testing. These capacitors are .250" by .225" and about .060" thick.

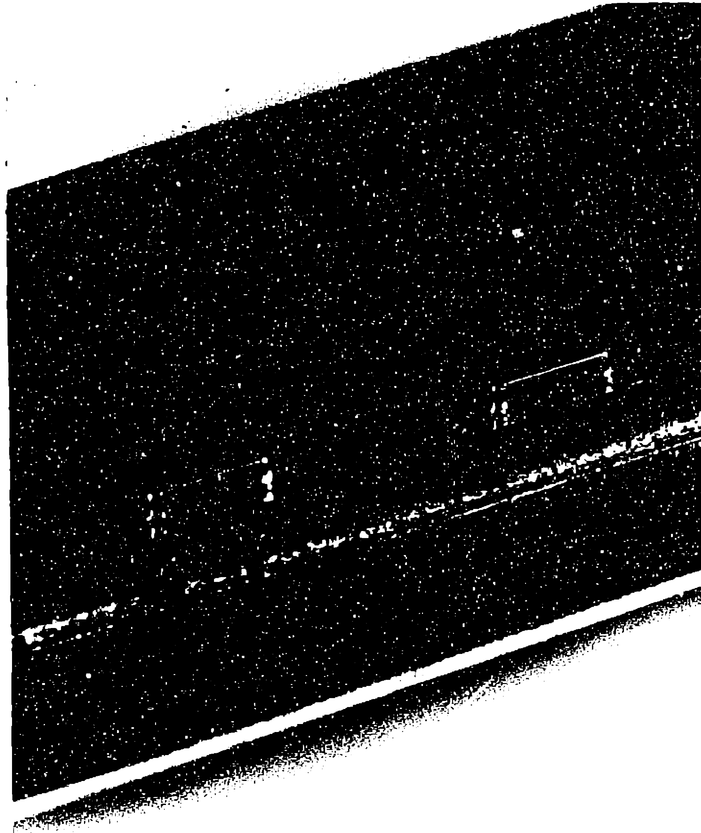

Figure 1: Chip capacitors mounted on a double-sided test board used for thermal cycle testing. These capacitors are .250" by .225" and about .060" thick.

INTENTIONAL DUPLICATE EXPOSURE

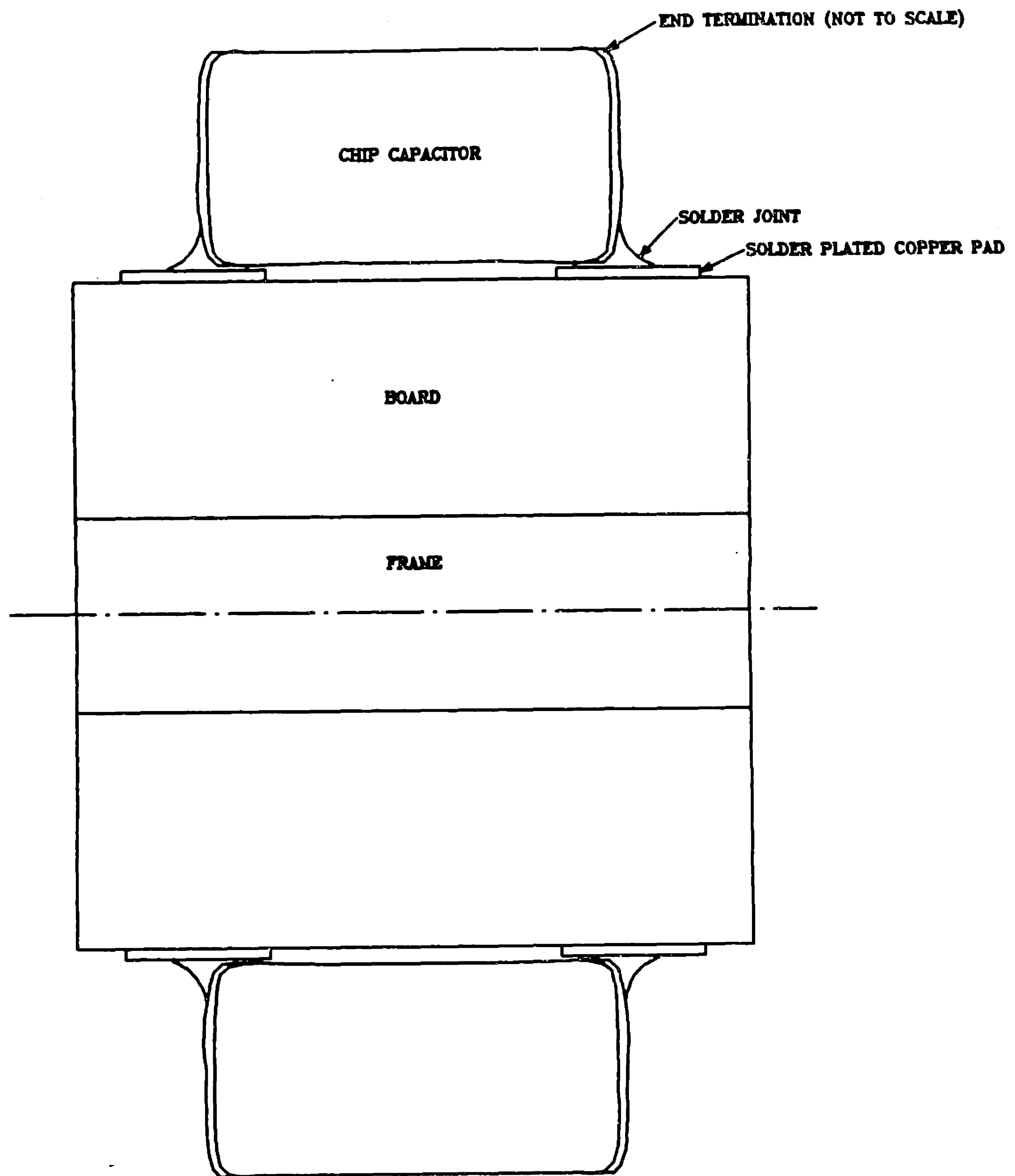

Figure 2: Schematic of cross-sectioned electronic assembly

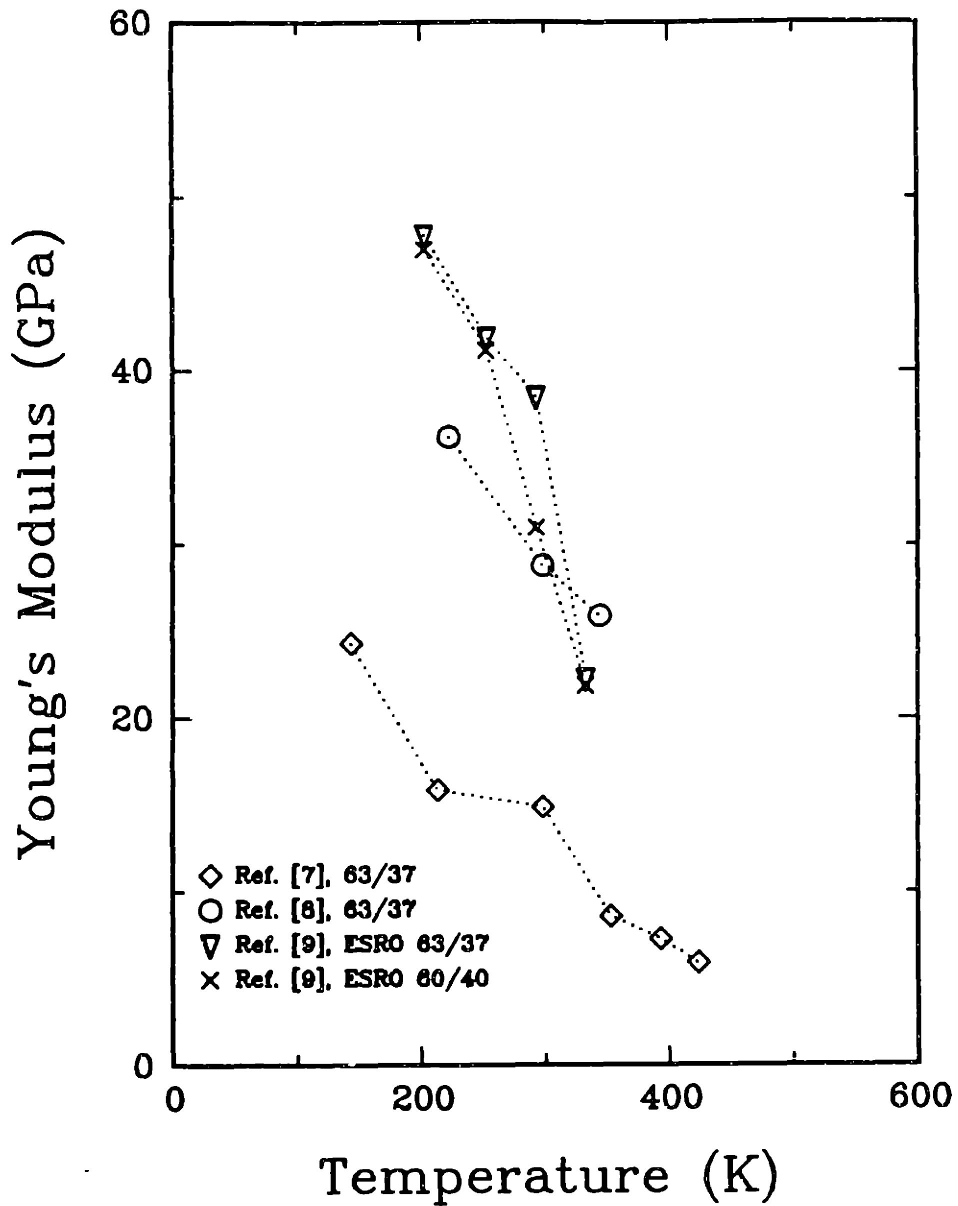

Figure 3: Some published values of the Young's modulus for near-eutectic tin-lead solders. The data from References 7 and 9 were obtained from monotonic tensile test results, while that from Reference 8 was obtained from the initial unloading of stress-relaxation specimens.

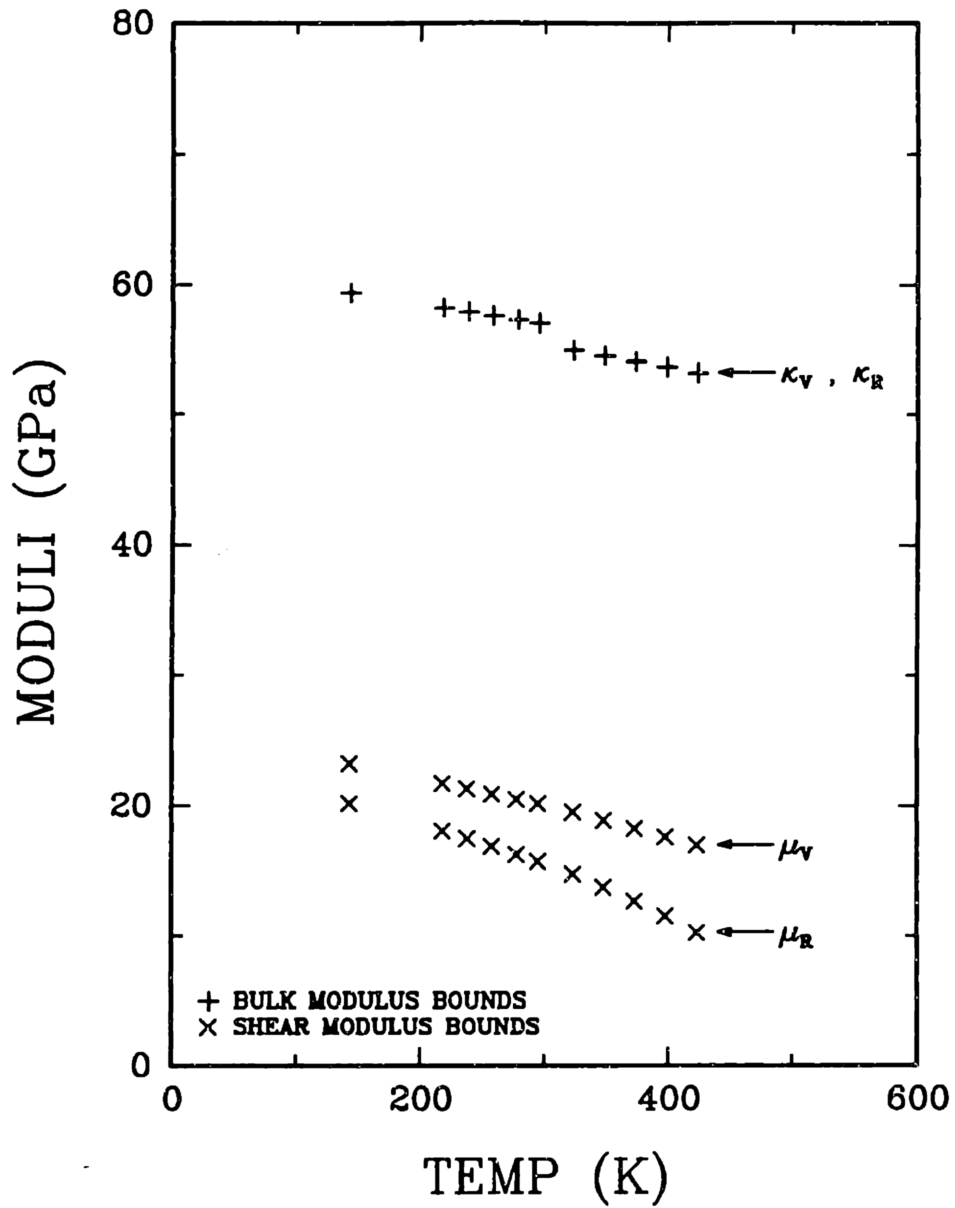

Figure 4: Bounds for the elastic moduli of tin

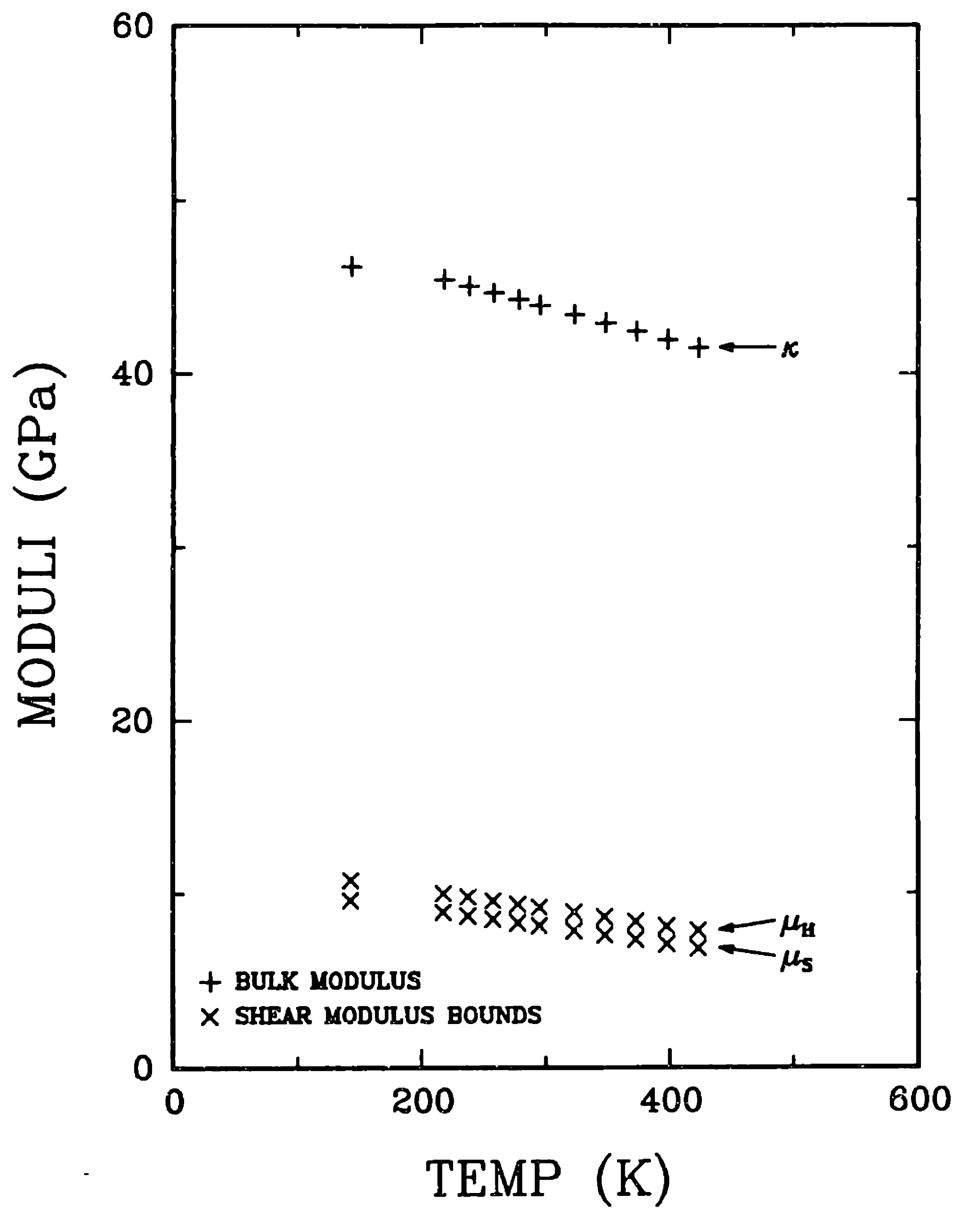

Figure 5: Bounds for the elastic moduli of lead

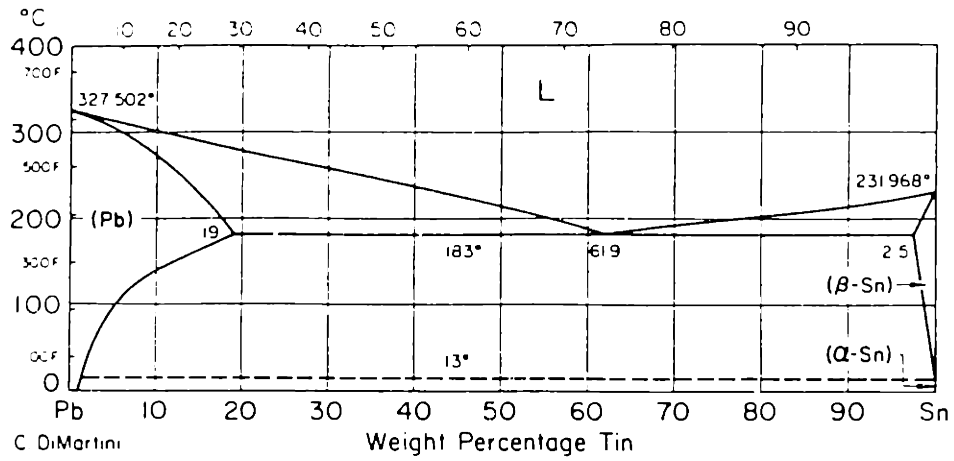

Figure 6: Tin-Lead Phase Diagram, from Barry and Thwaites [15]

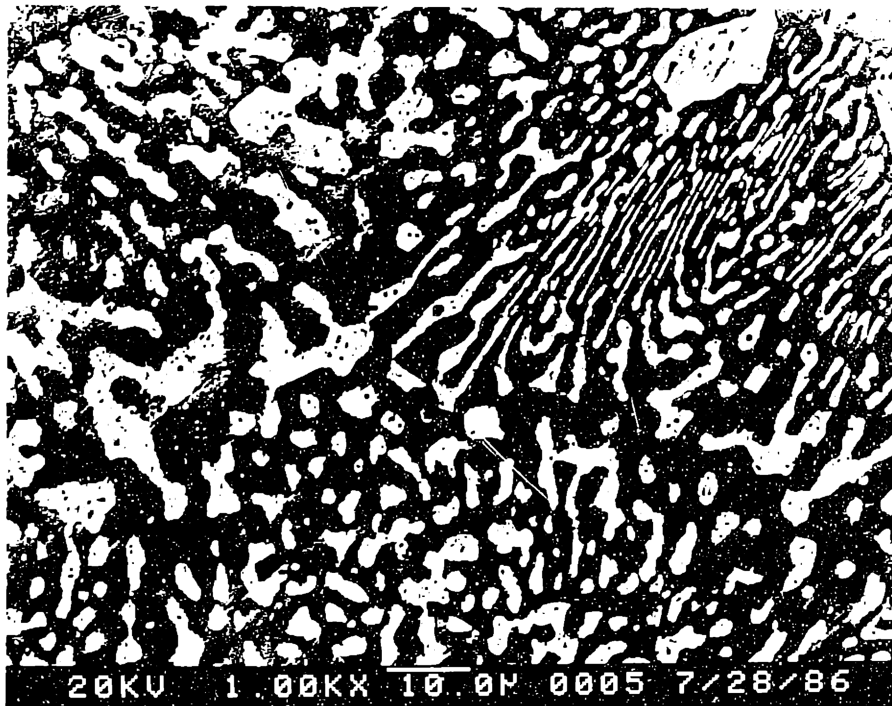

Figure 7: SEM micrograph of 60/40 tin-lead solder; magnification 1000×. The lighter areas are lead-rich regions; the darker areas are the tin-rich matrix.

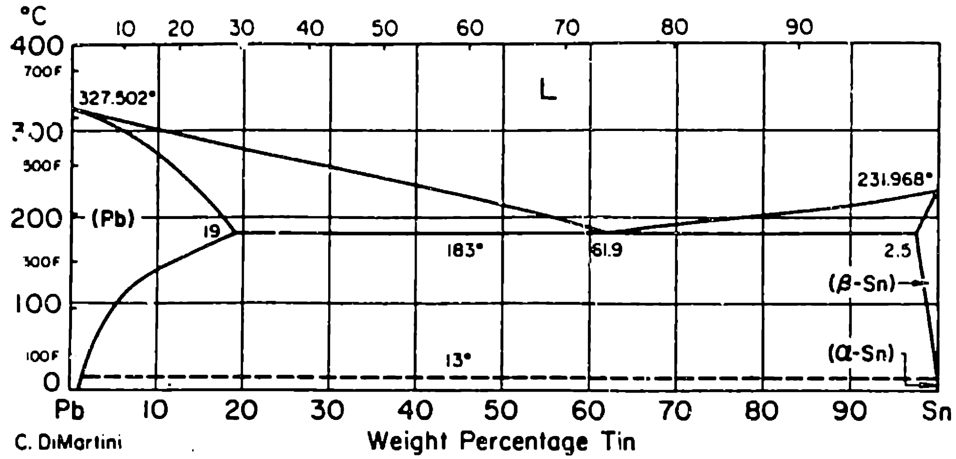

Figure 6: Tin-Lead Phase Diagram, from Barry and Thwaites [15]

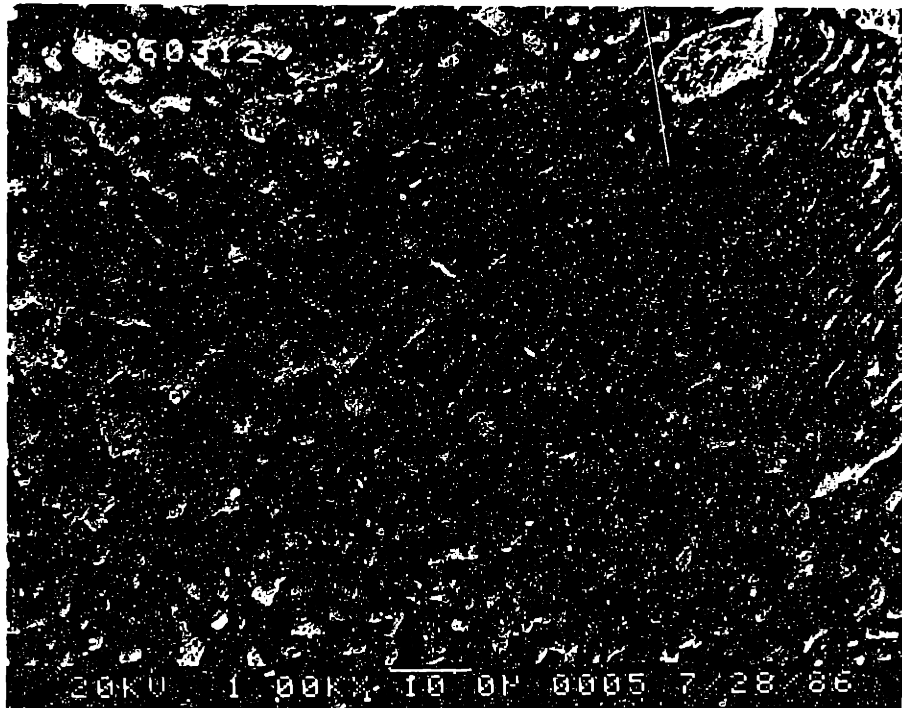

Figure 7: SEM micrograph of 60/40 tin-lead solder; magnification 1000×. The lighter areas are lead-rich regions; the darker areas are the tin-rich matrix.

INTENTIONAL DUPLICATE EXPOSURE

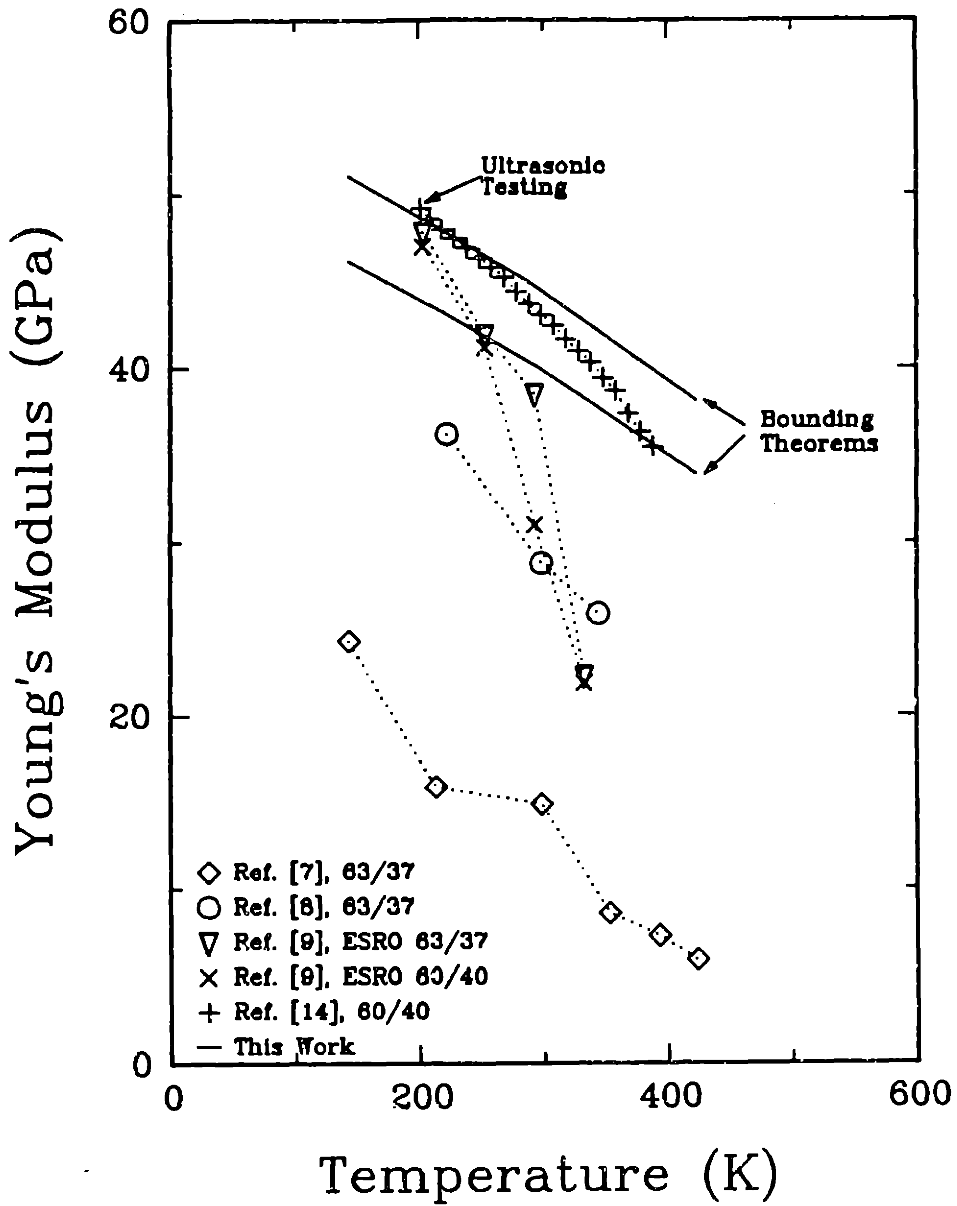

Figure 8: Young's Modulus of Near-Eutectic Tin-Lead

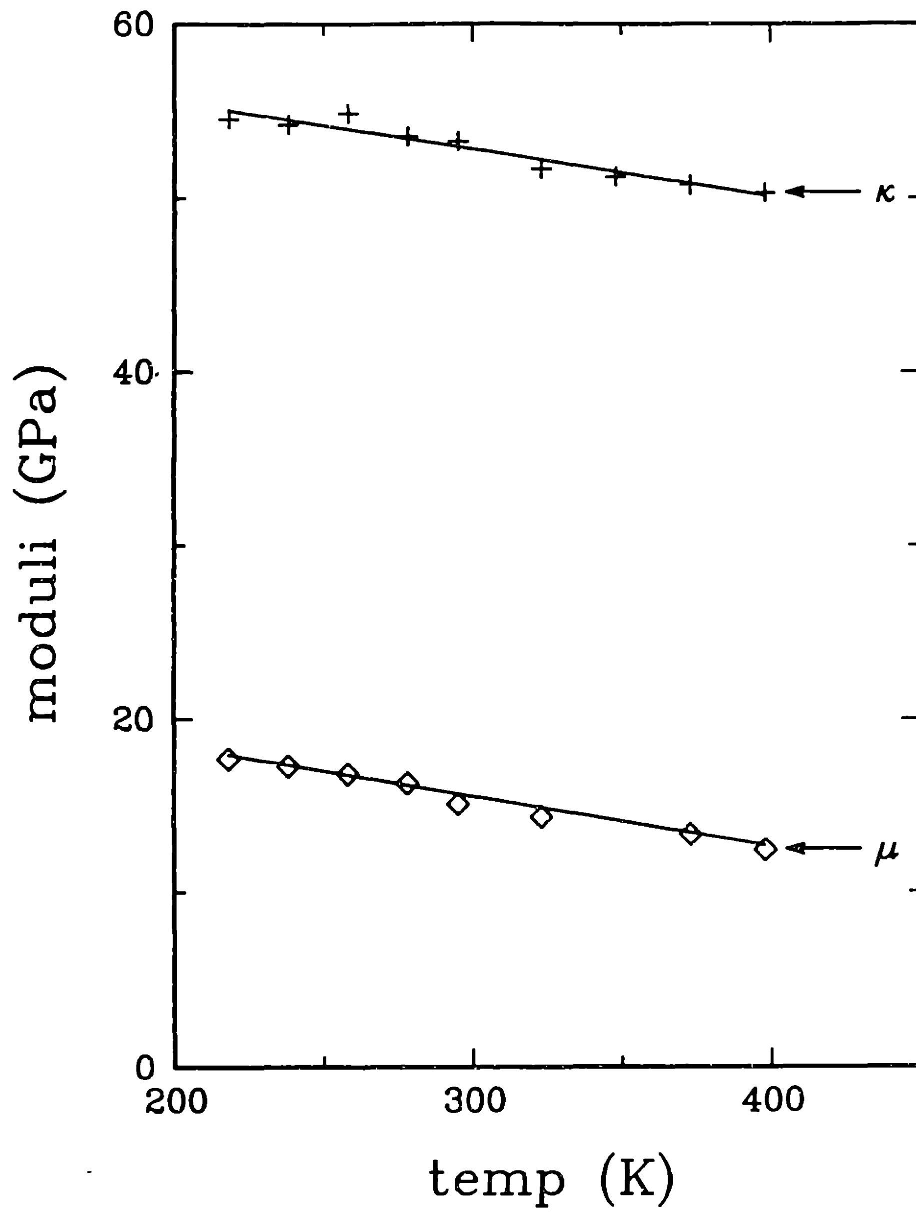

Figure 9: Results of the calculations of the shear and bulk moduli of 60/40 tin-lead solder.

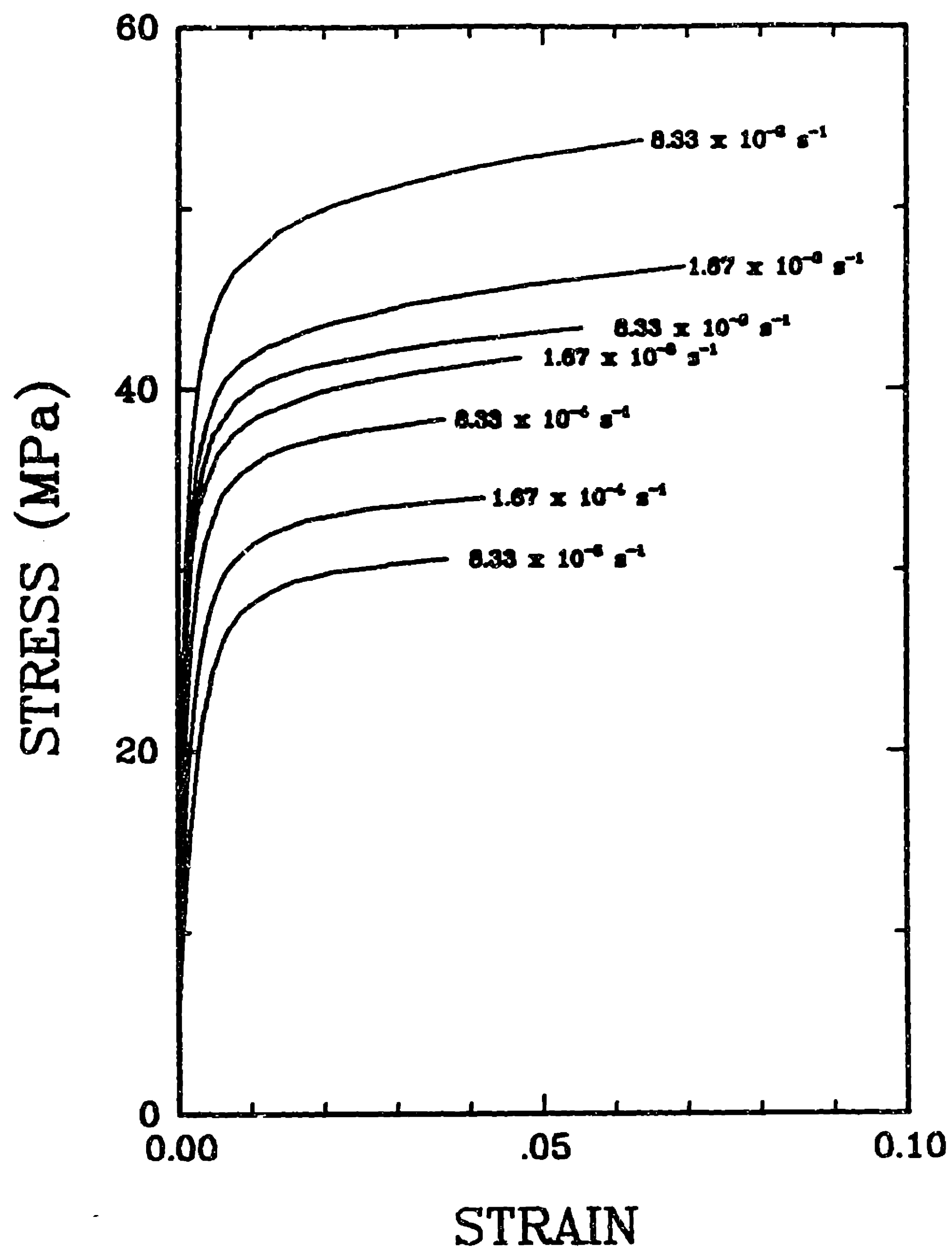

Figure 10: Strain rate dependence of stress-strain curves for 60/40 tin-lead solder at 22 C

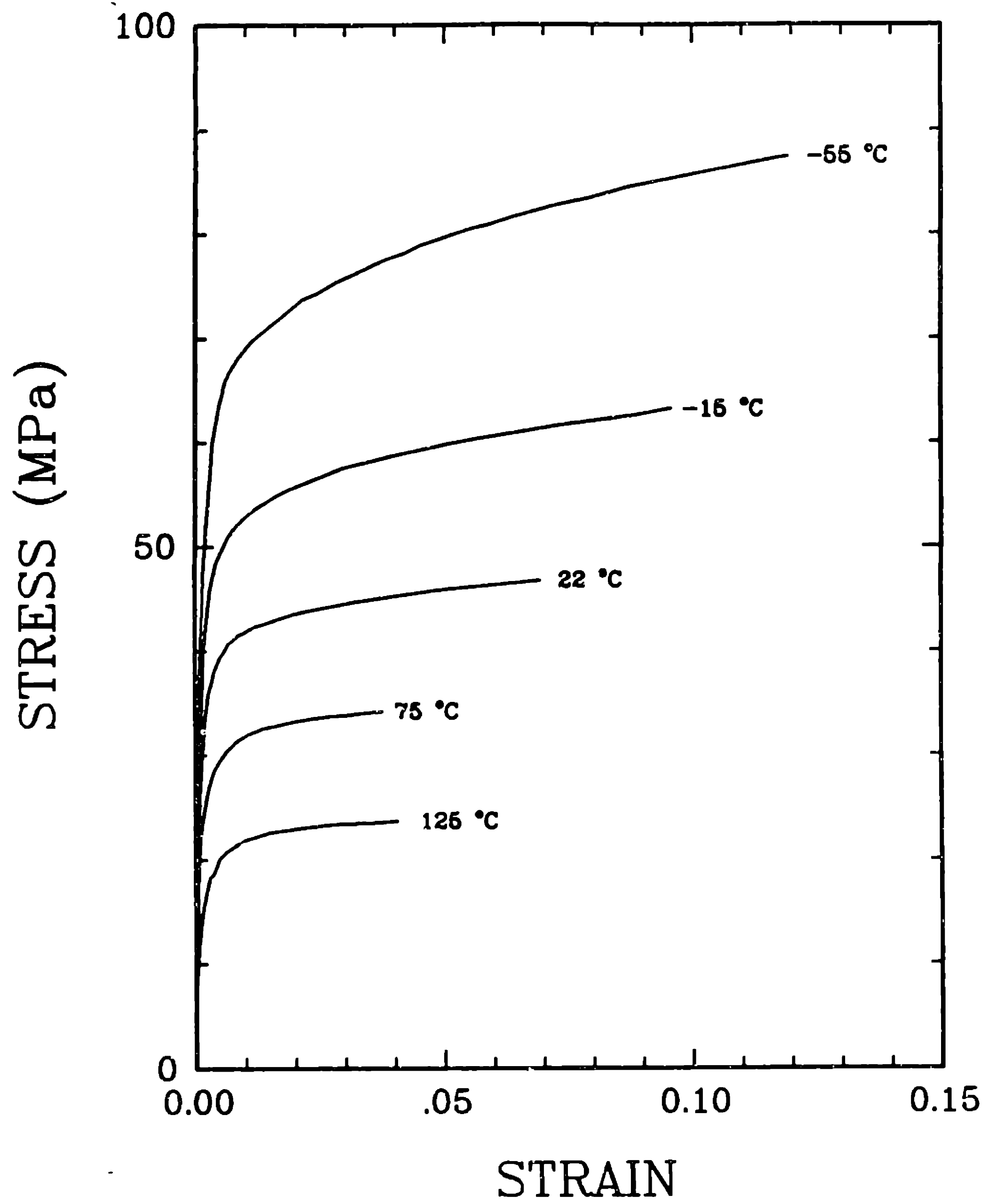

Figure 11: Temperature dependence of stress-strain curves for 60/40 tin-lead solder at 1.67×10^{-2} s^{-1}

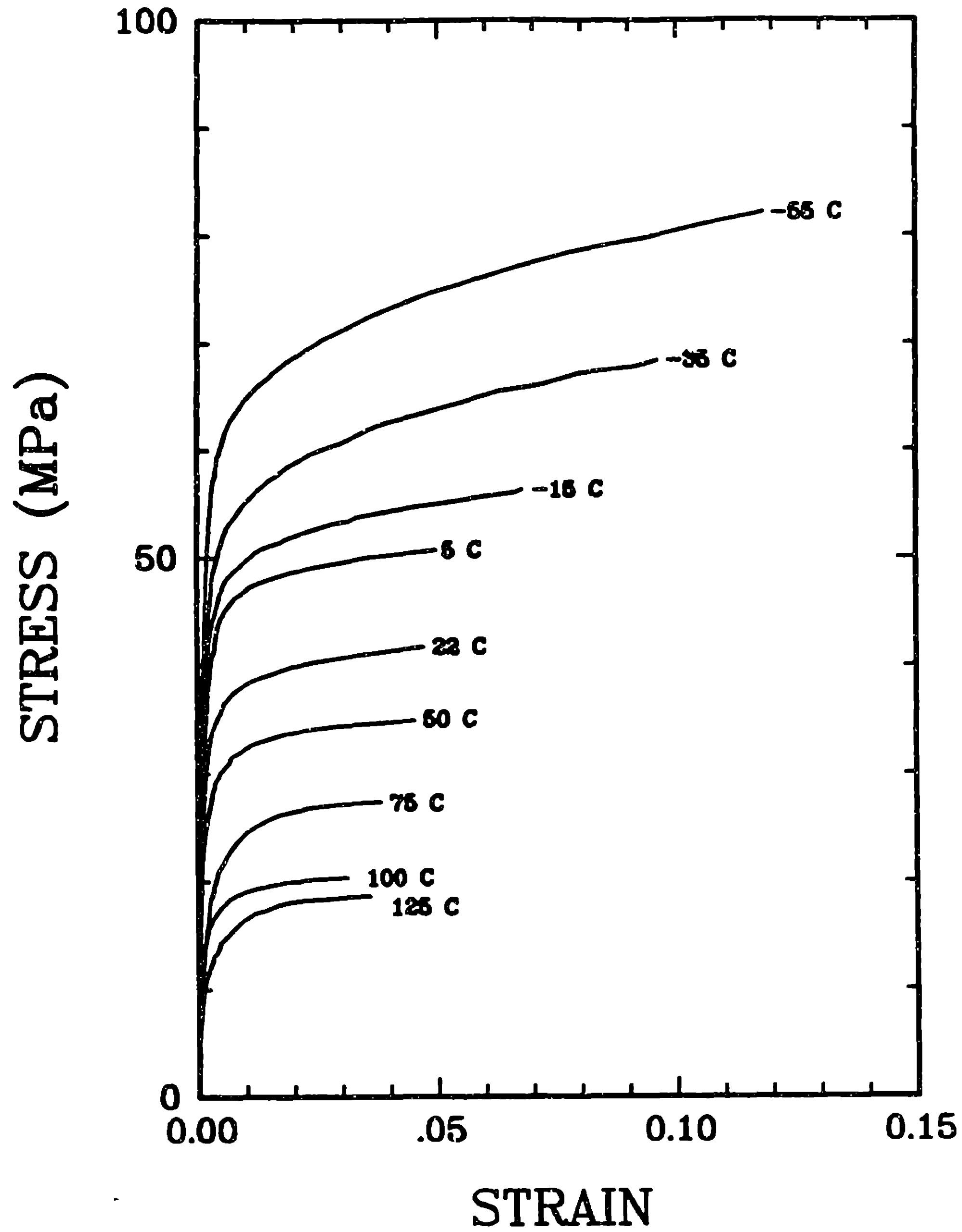

Figure 12: Temperature dependence of stress-strain curves for 60/40 tin-lead solder at 1.67×10^{-3} s^{-1}

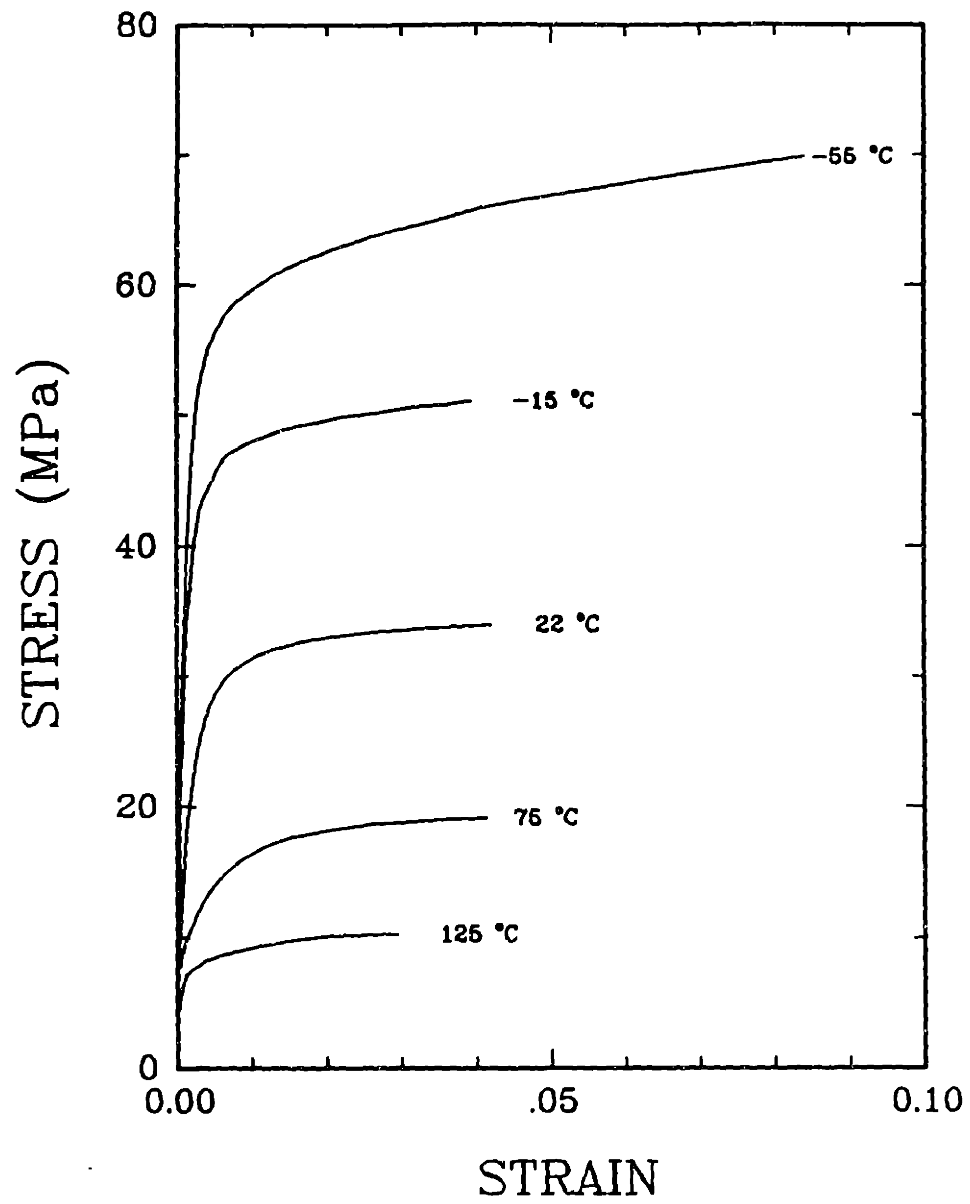

Figure 13: Temperature dependence of stress-strain curves for 60/40 tin-lead solder at 1.67×10^{-4} s^{-1}

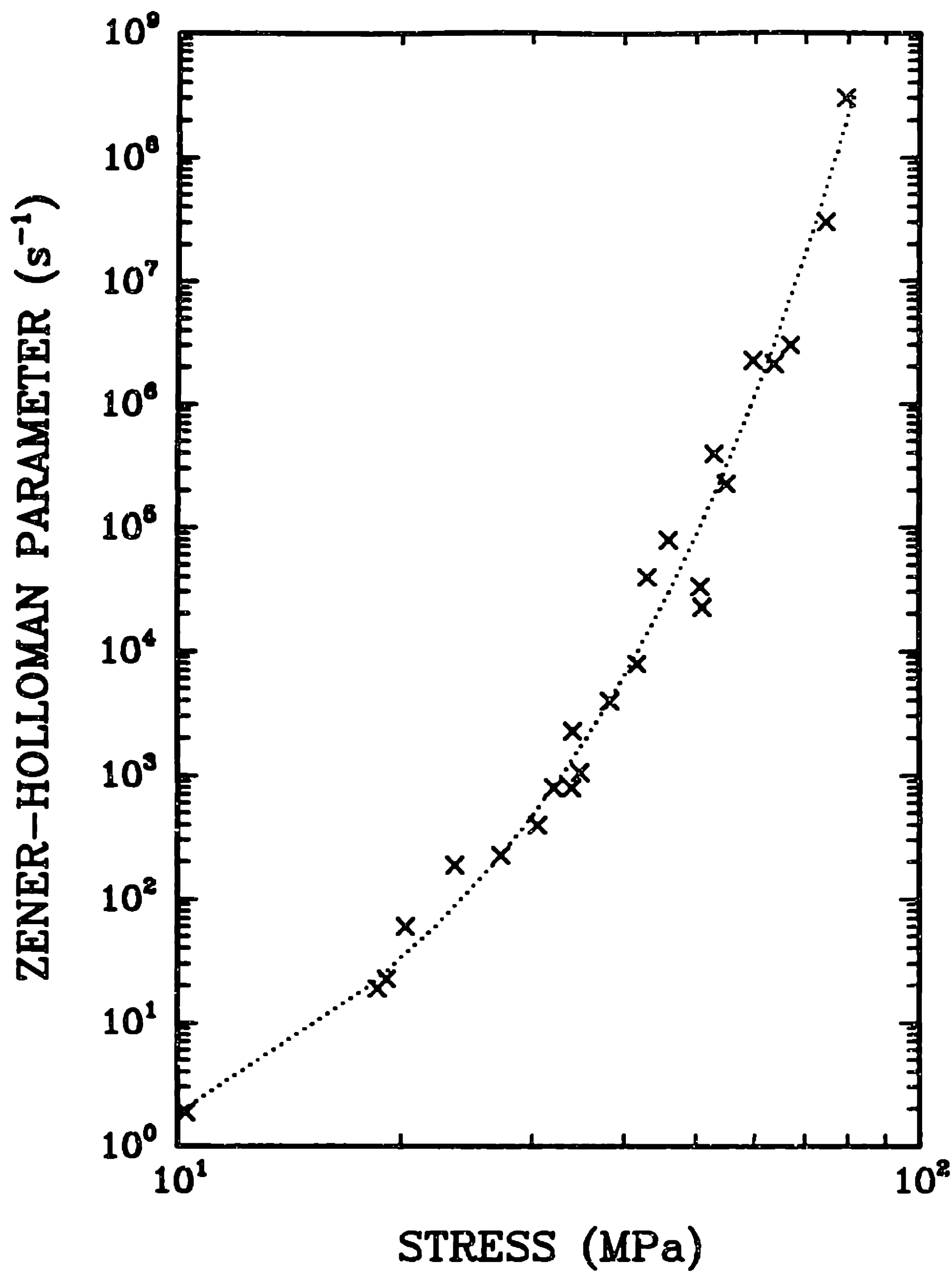

Figure 14: Fit of the stress-strain data to the hyperbolic sine model

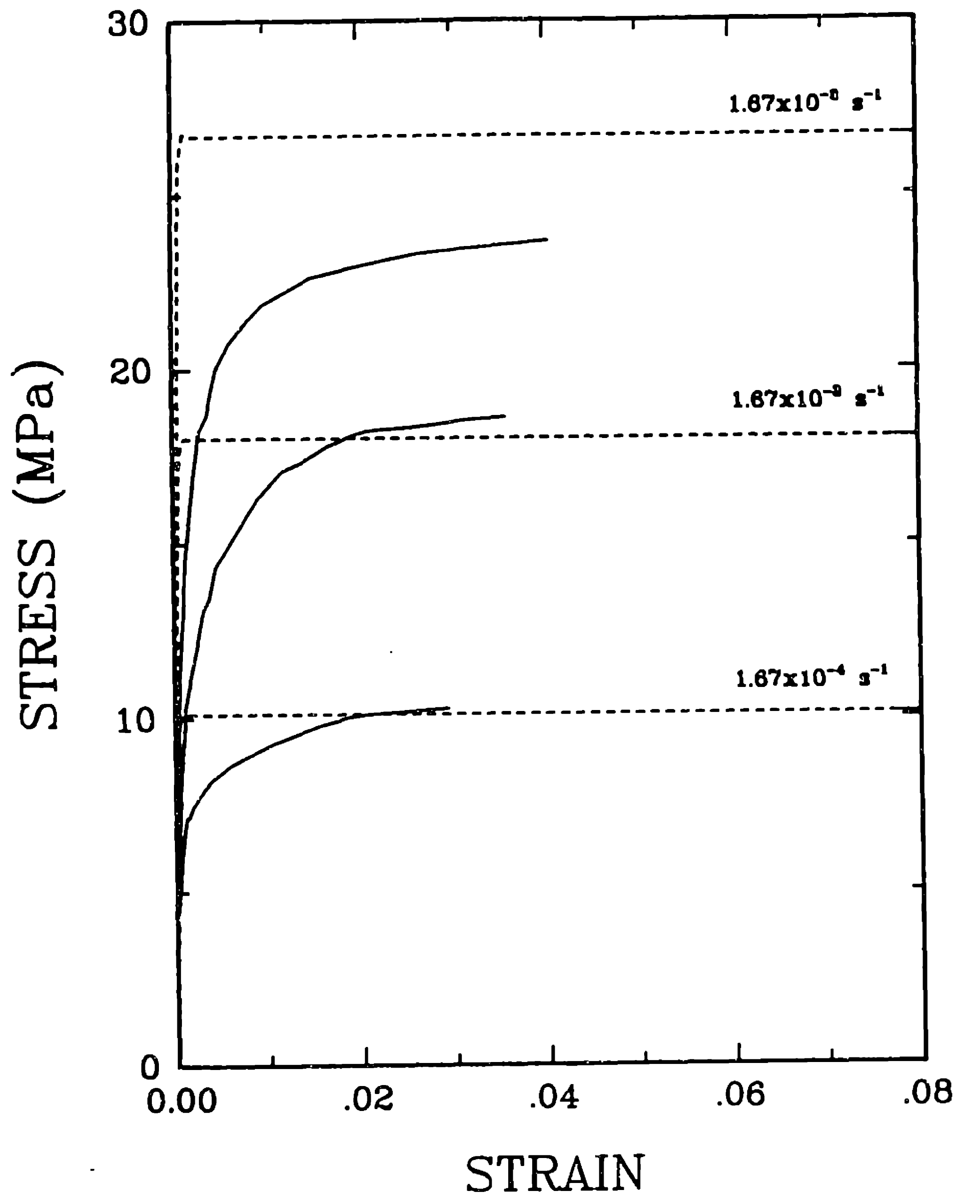

Figure 15: Comparison between the model and the data at 125 C

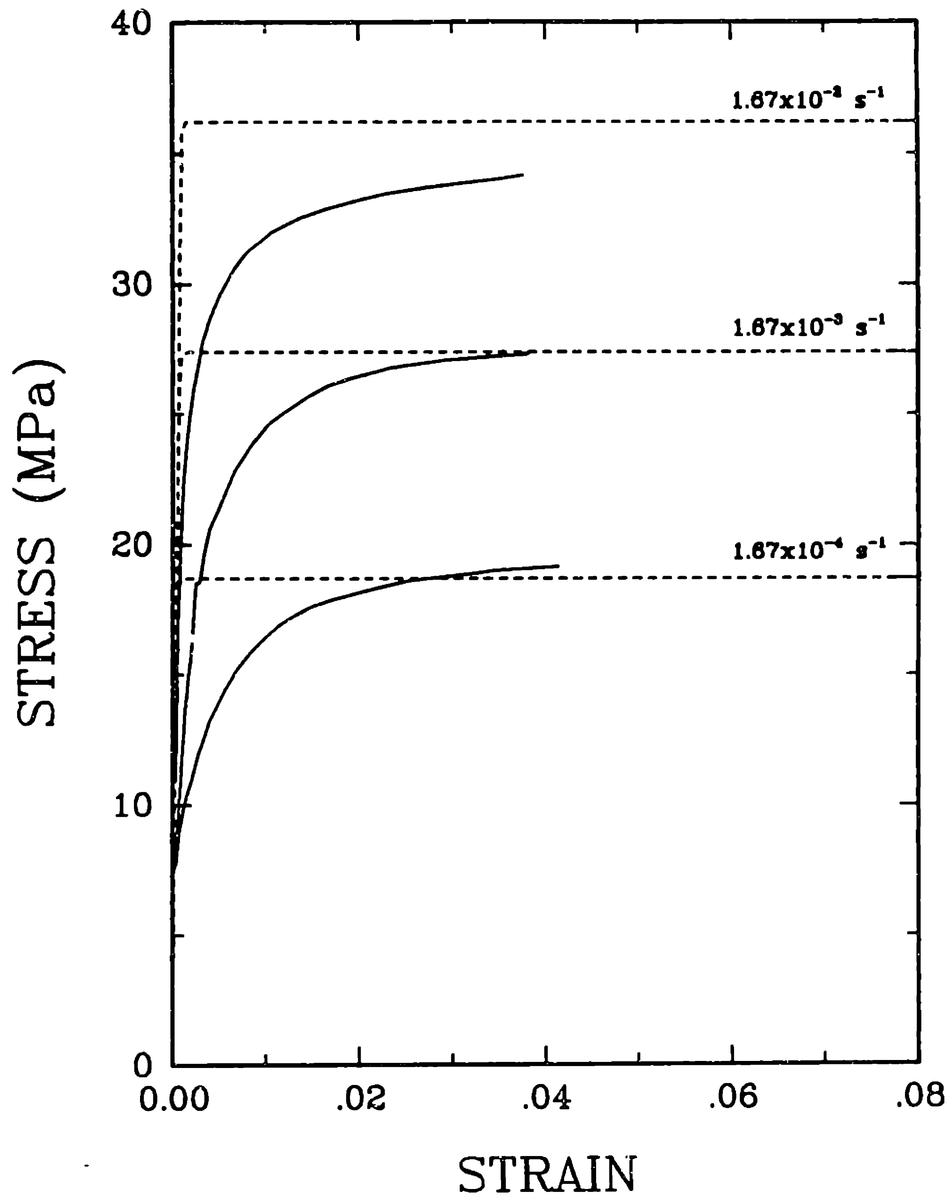

Figure 16: Comparison between the model and the data at 75 C

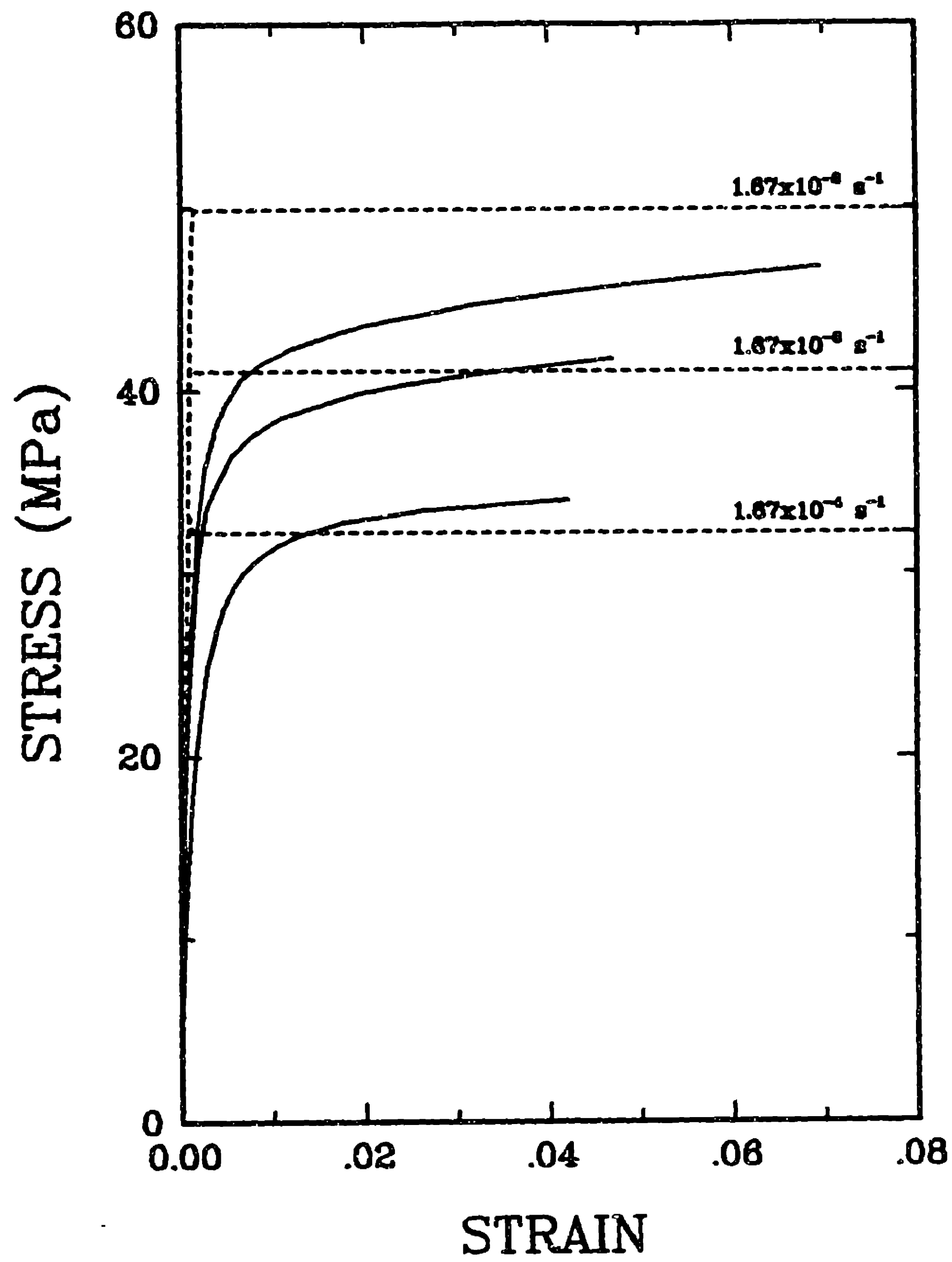

Figure 17: Comparison between the model and the data at 22 C

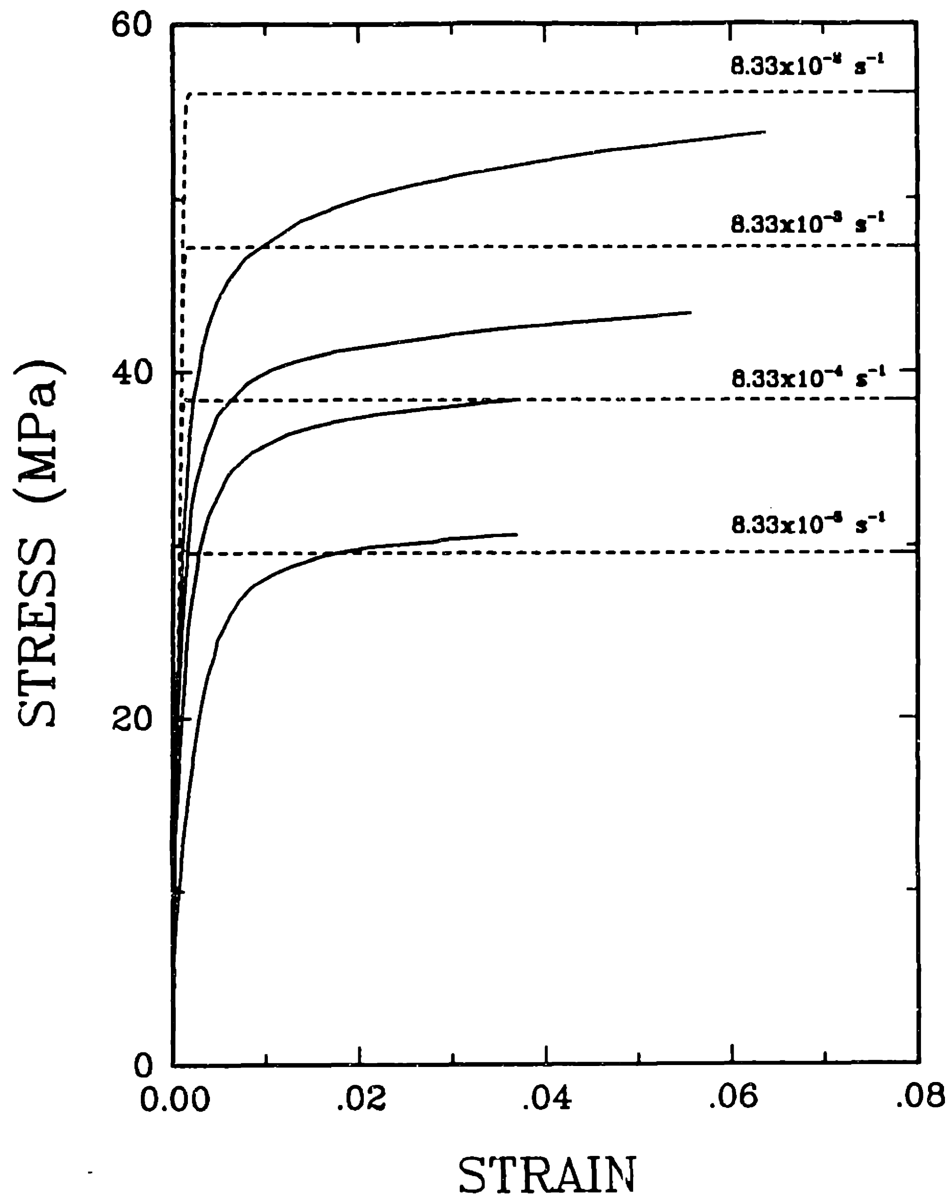

Figure 18: Comparison between the model and the data at 22 C

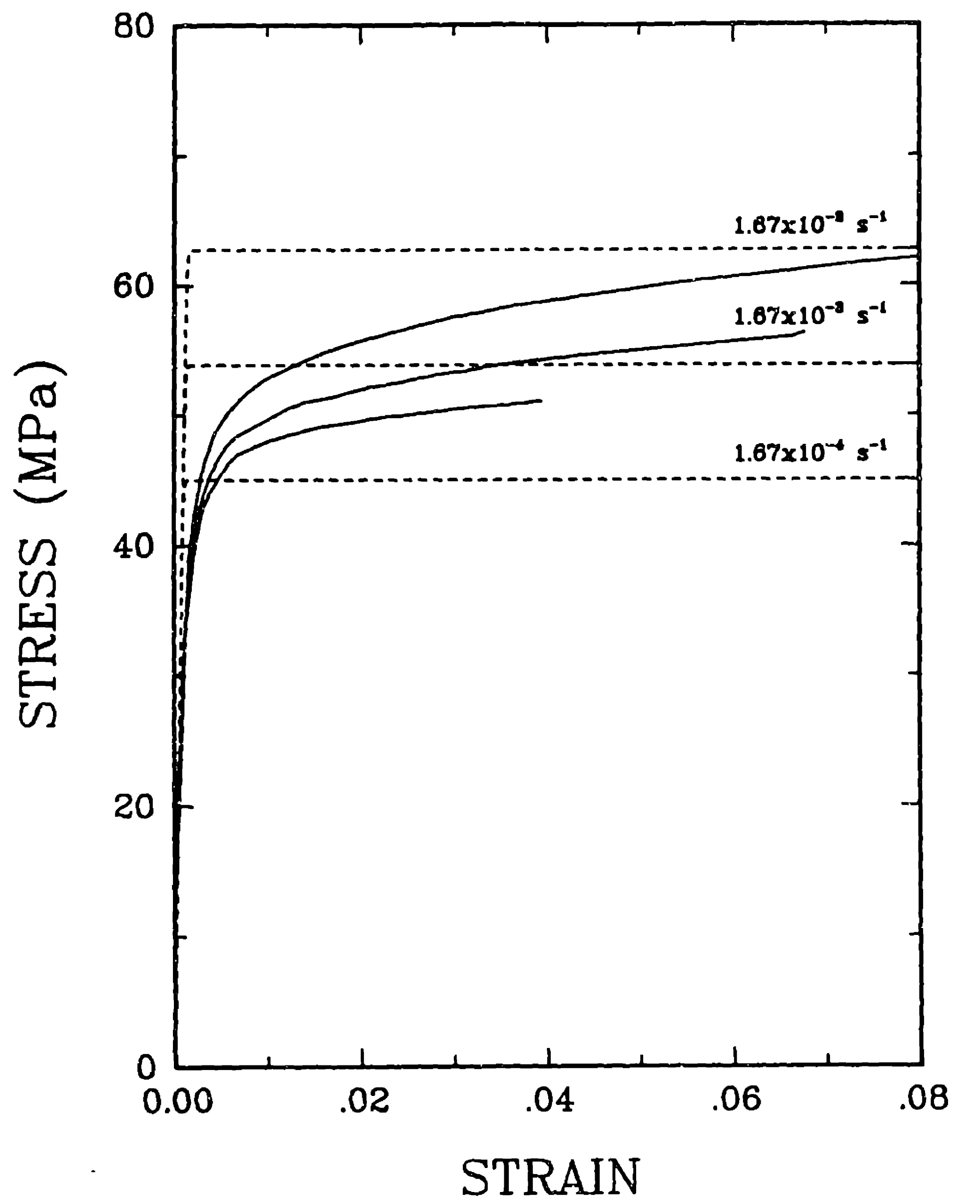

Figure 19: Comparison between the model and the data at -15 C

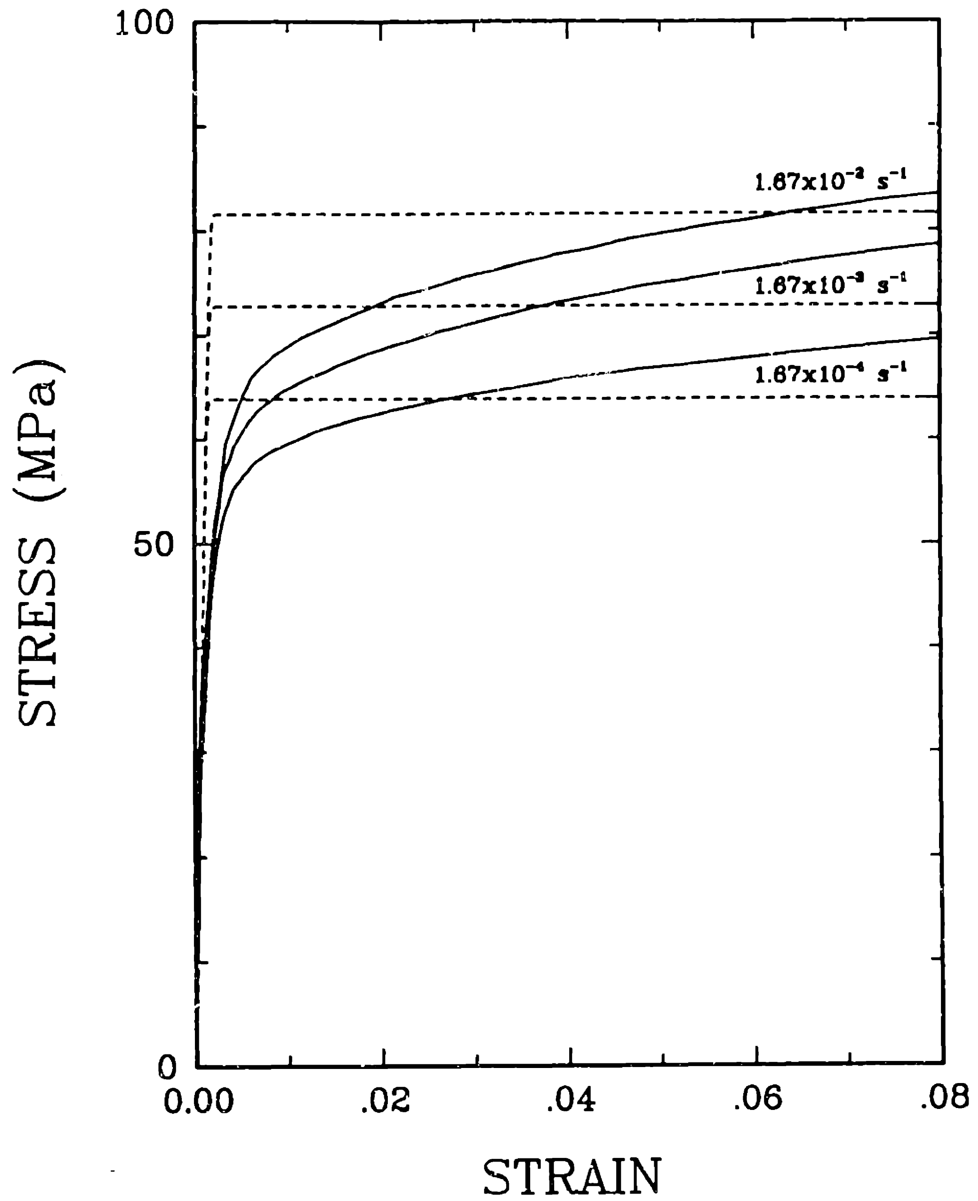

Figure 20: Comparison between the model and the data at -55 C

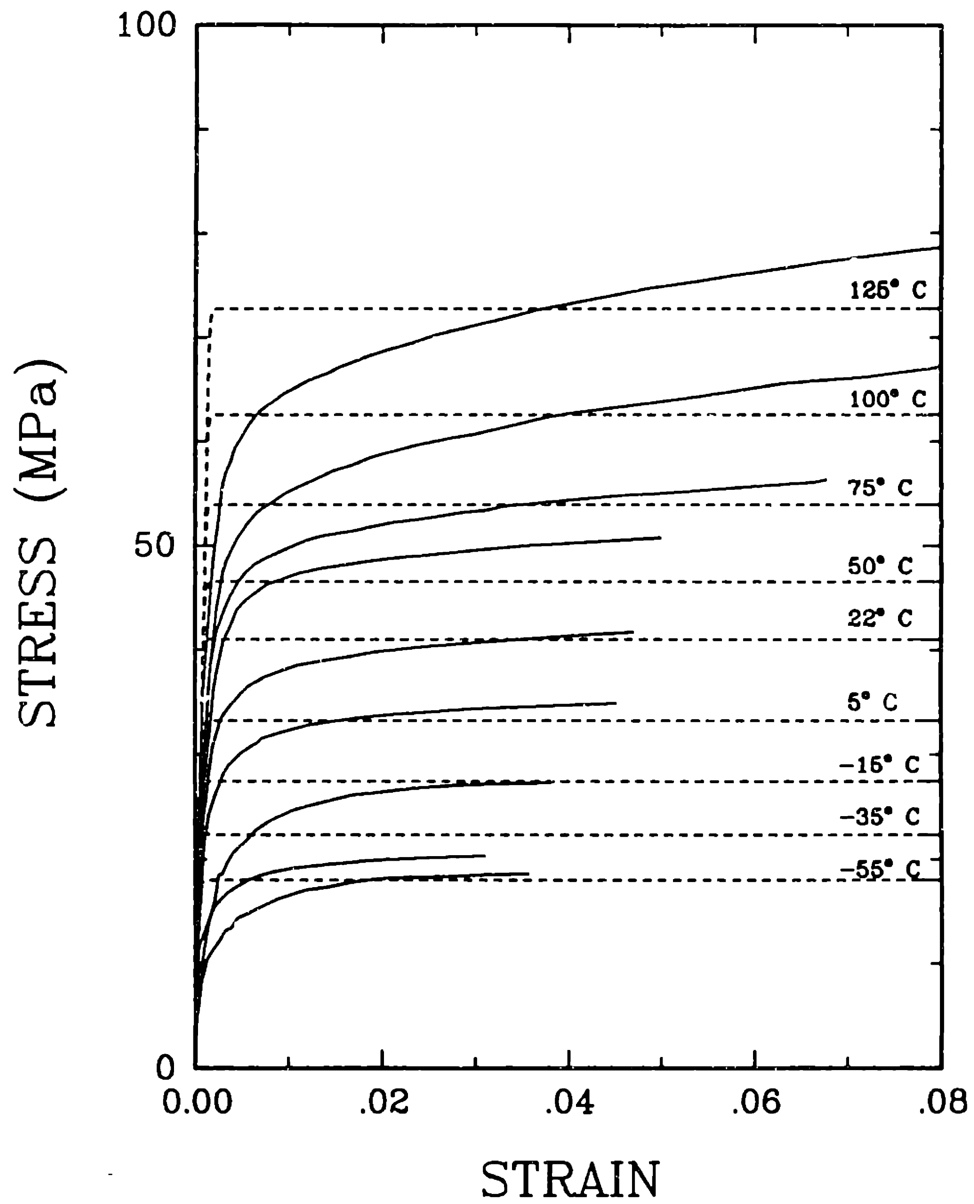

Figure 21: Comparison between the model and the data at 1.67×10^{-3} s^{-1}

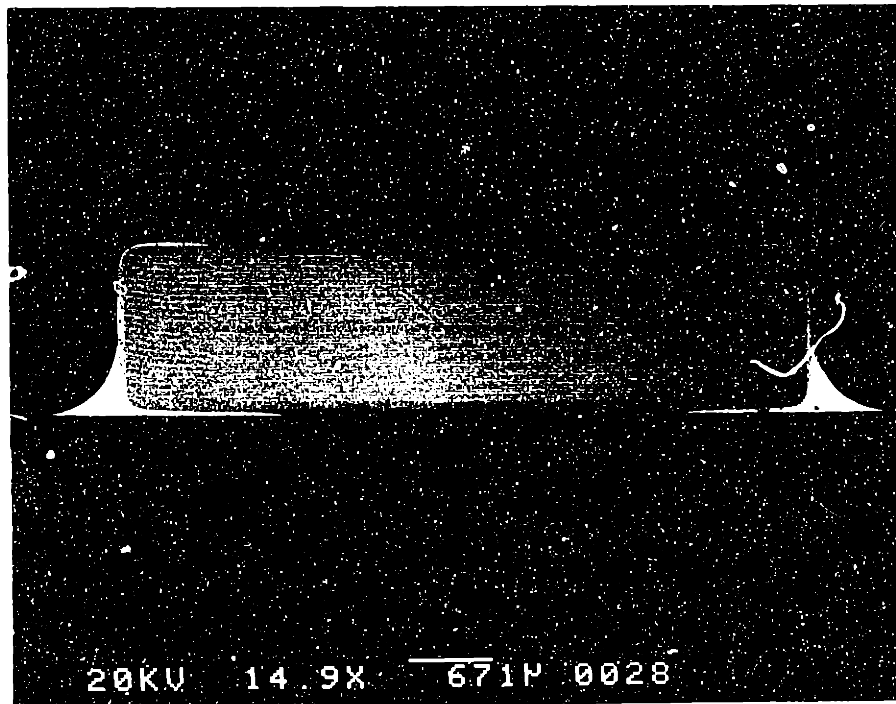

Figure 22: Cross-sectioned capacitor mounted on a board. The specimen was metallographically prepared, but not etched. This is a backscatter electron image, in which differences in atomic number show up as differences in contrast, with the materials with the highest atomic number the lightest. The magnification is 14.9x.

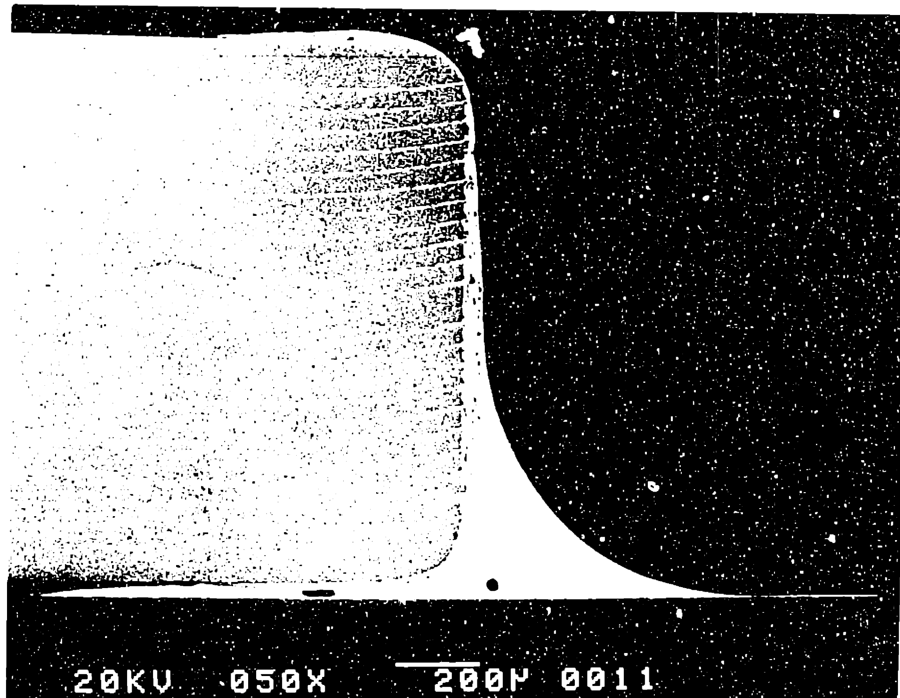

Figure 23: SEM micrograph of the solder joint on the right side of the capacitor shown above at a magnification of 50x

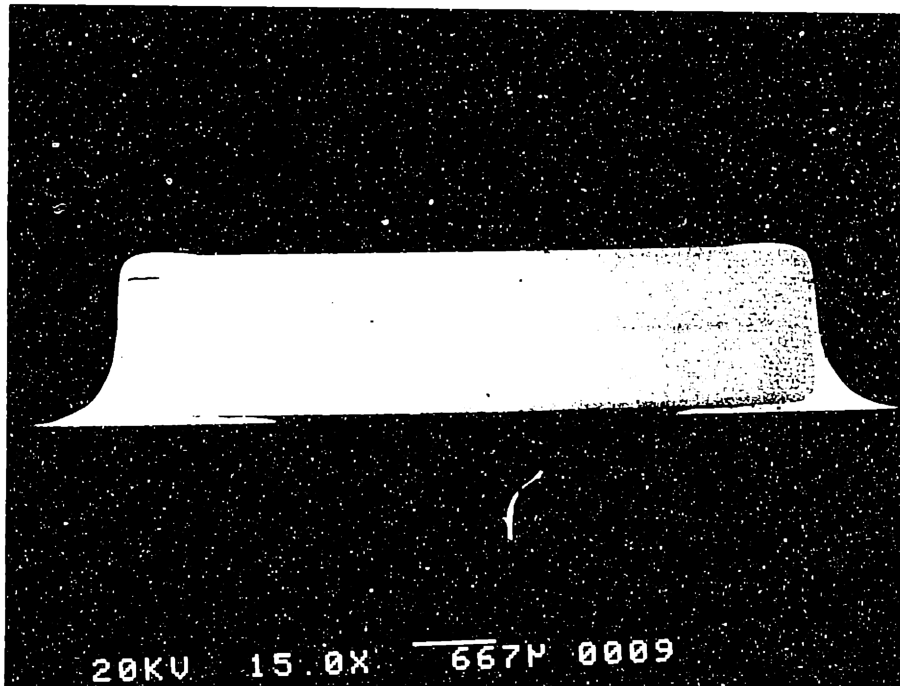

Figure 24: Micrograph of a cross-sectioned chip capacitor after 200 thermal cycles. The specimen was metallographically prepared but not etched. Magnification is 15.0x.

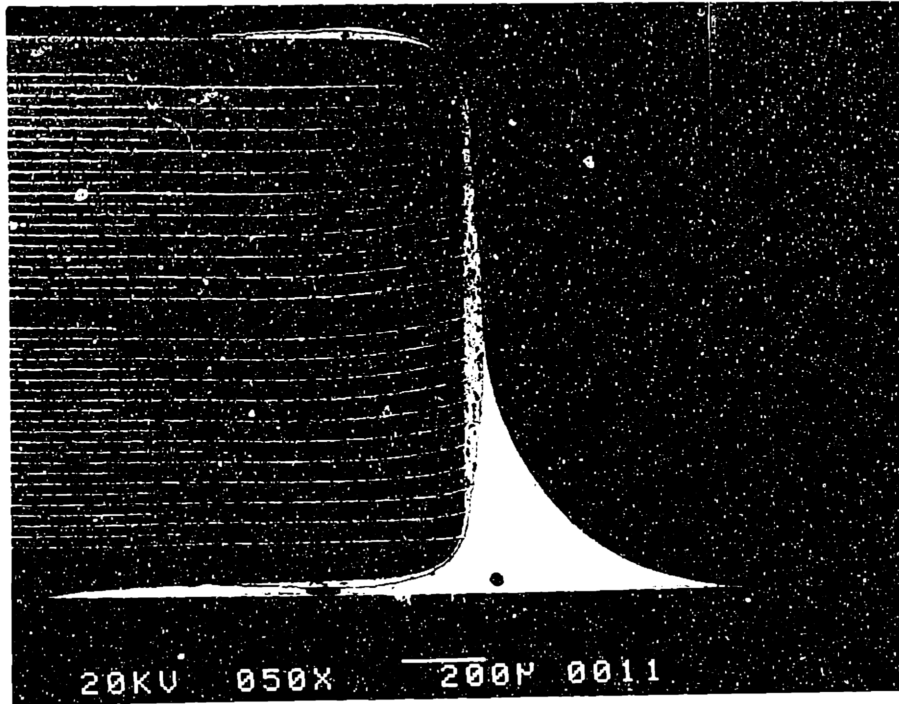

Figure 23: SEM micrograph of the solder joint on the right side of the capacitor shown above at a magnification of 50x

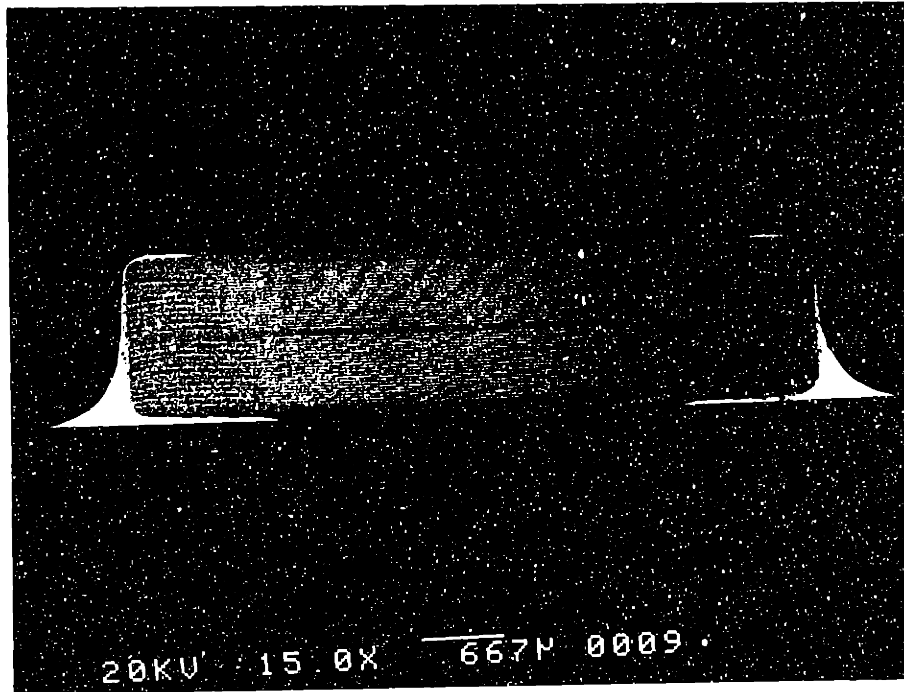

Figure 24: Micrograph of a cross-sectioned chip capacitor after 200 thermal cycles. The specimen was metallographically prepared but not etched. Magnification is 15.0x.

INTENTIONAL DUPLICATE EXPOSURE

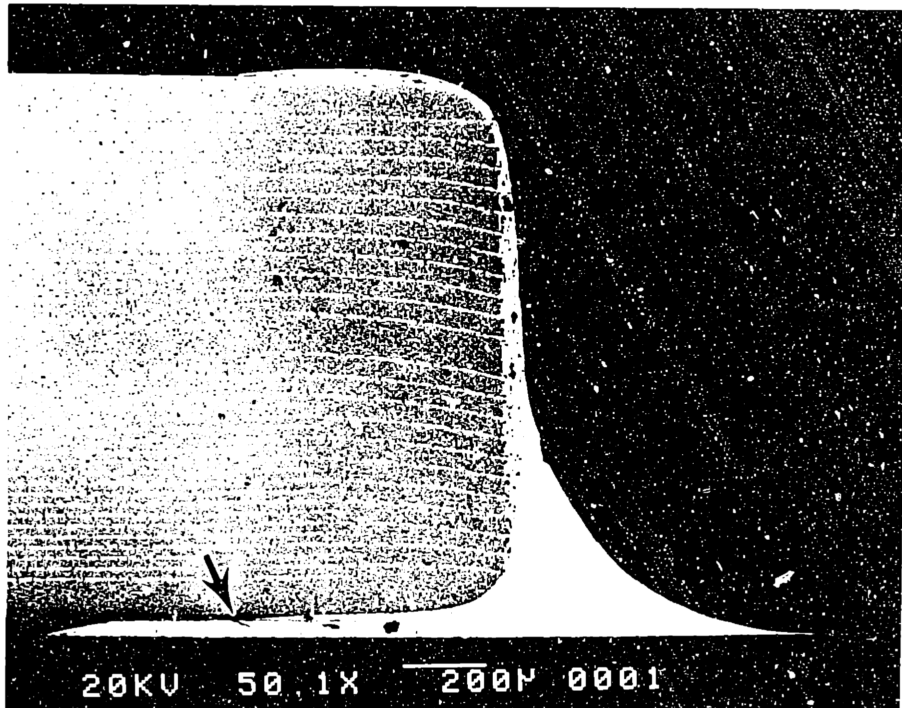

Figure 25: SEM micrograph of the cracked solder joint shown in the above photograph. The specimen was metallographically prepared, but not etched. The magnification is 50.1x; the crack is indicated by an arrow.

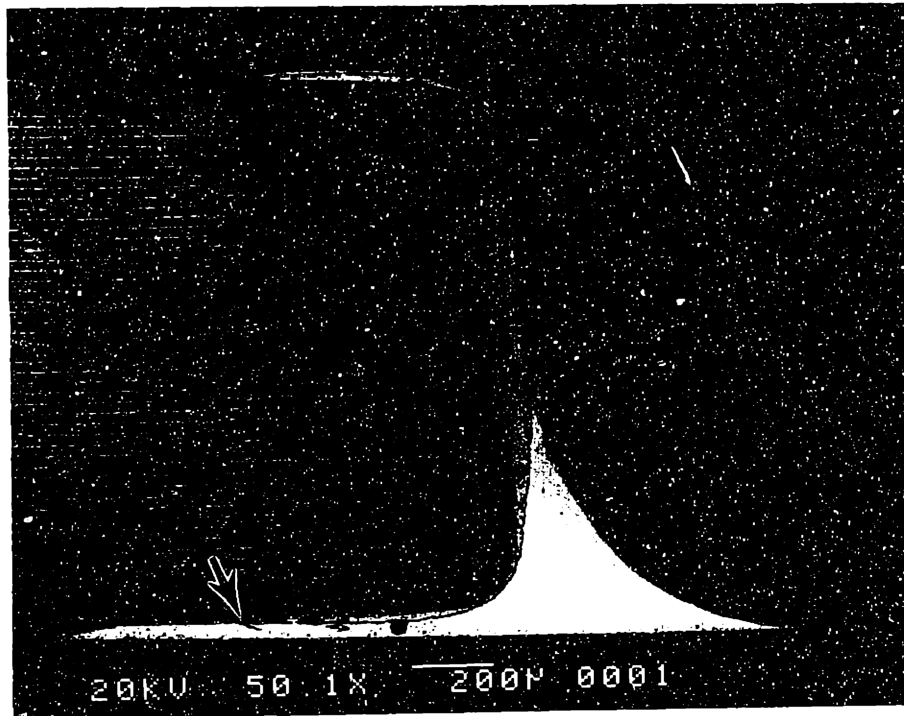

Figure 25: SEM micrograph of the cracked solder joint shown in the above photograph. The specimen was metallographically prepared, but not etched. The magnification is 50.1x; the crack is indicated by an arrow.

INTENTIONAL DUPLICATE EXPOSURE

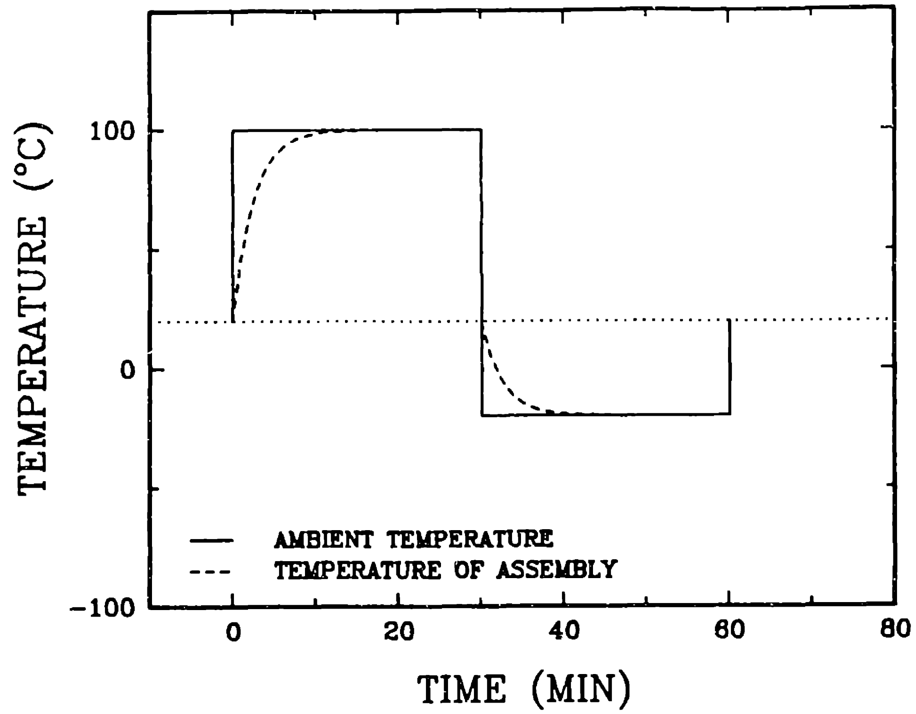

Figure 26: An actual thermal cycle showing the difference between the ambient temperature and the temperature of the assembly.

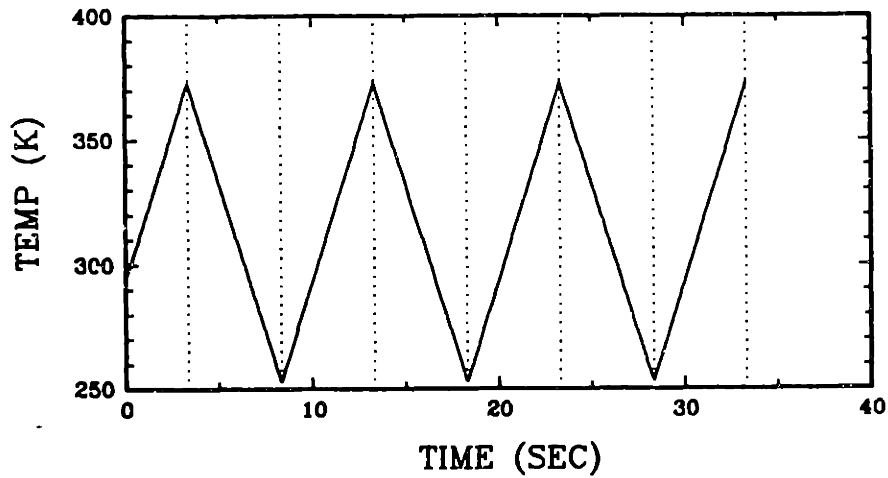

Figure 27: Temperature history input

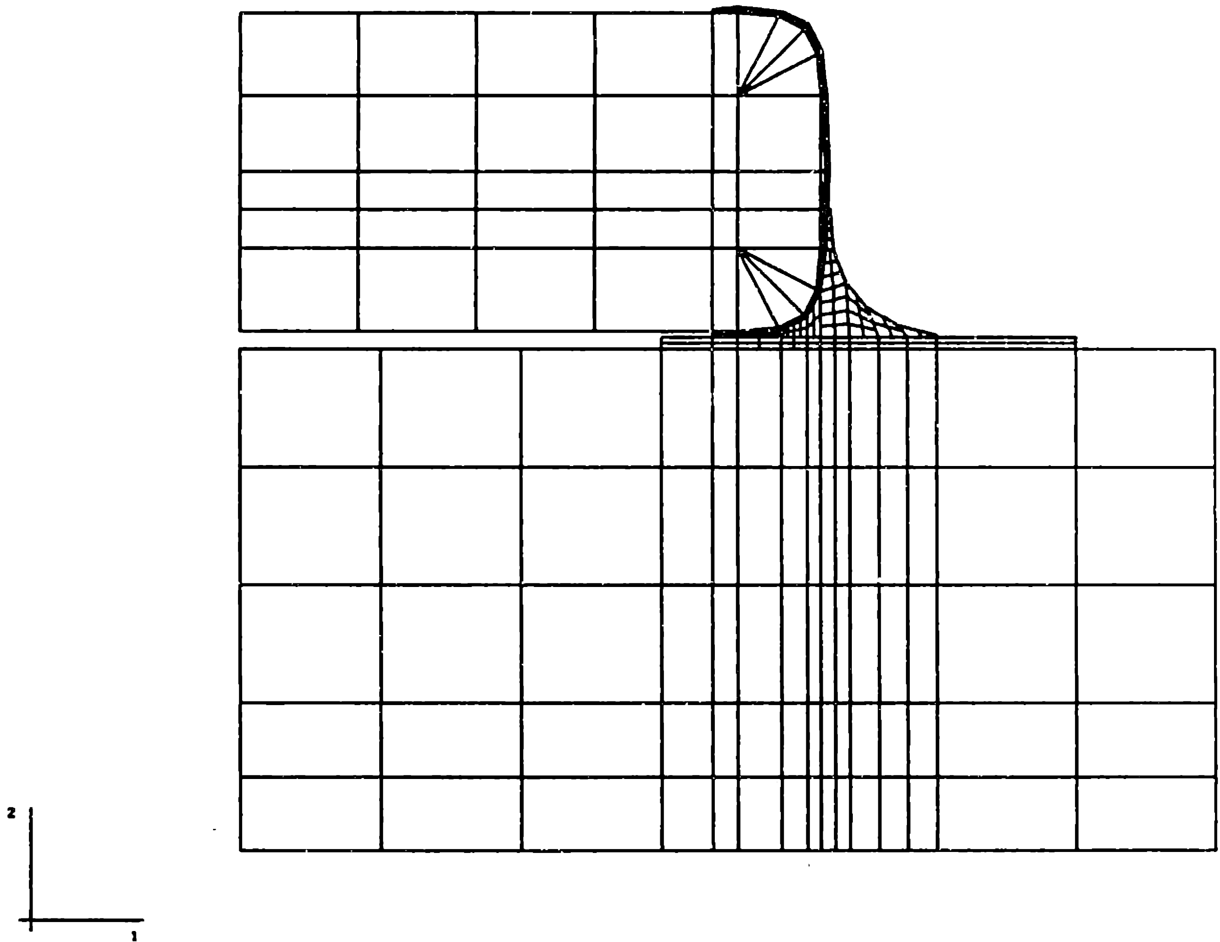

Figure 28: Finite element mesh of electronic assembly

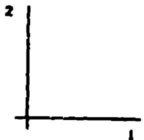

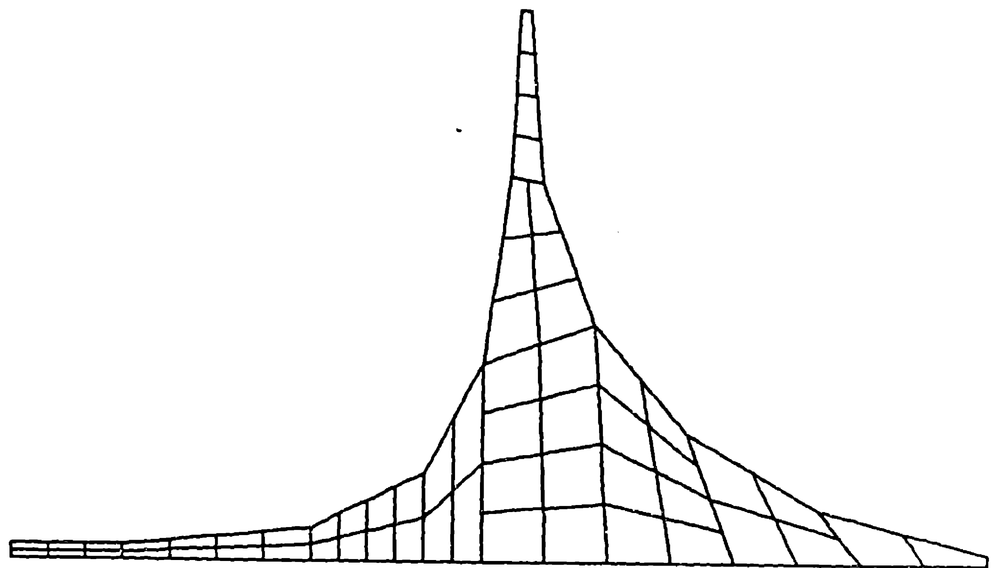

Figure 29: Finite element mesh of solder joint

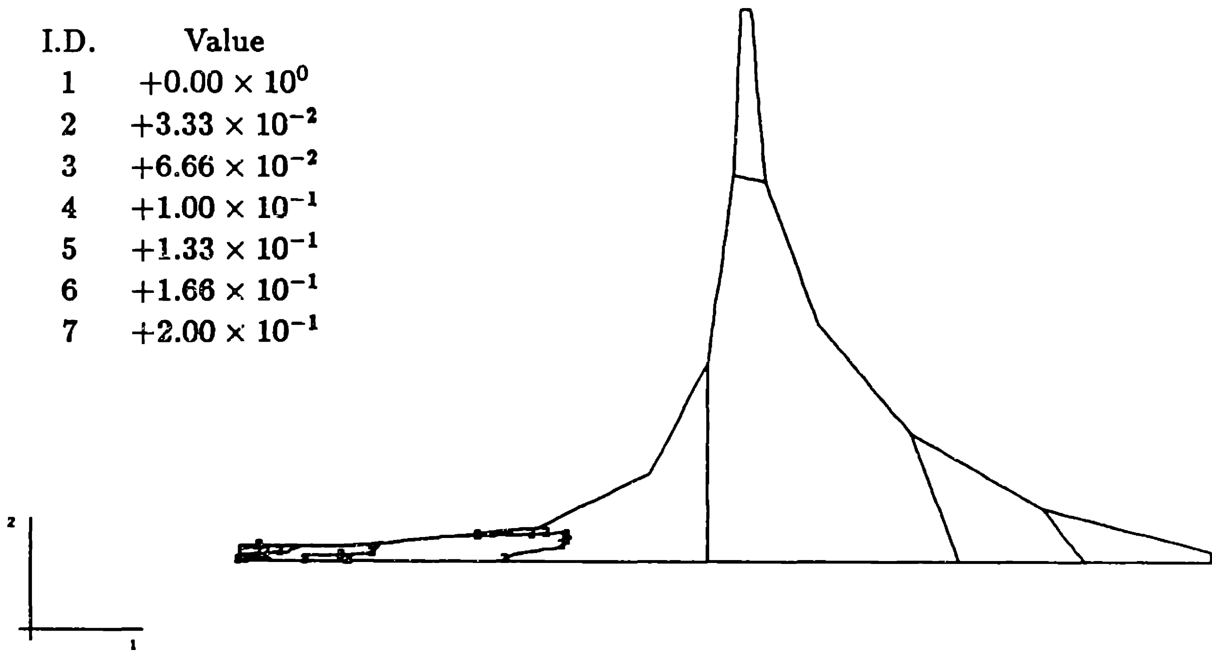

SOLDER JOINT AT 100 C. FIRST HYSTERESIS LOOP

STEP 5 INCREMENT 13

Figure 30: Equivalent plastic shear strain contours in the solder joint

I.D.	Value
1	$+0.00 \times 10^{0}$
2	$+3.33 \times 10^{-2}$
3	$+6.66 \times 10^{-2}$
4	$+1.00 \times 10^{-1}$
5	$+1.33 \times 10^{-1}$
6	$+1.66 \times 10^{-1}$
7	$+2.00 \times 10^{-1}$

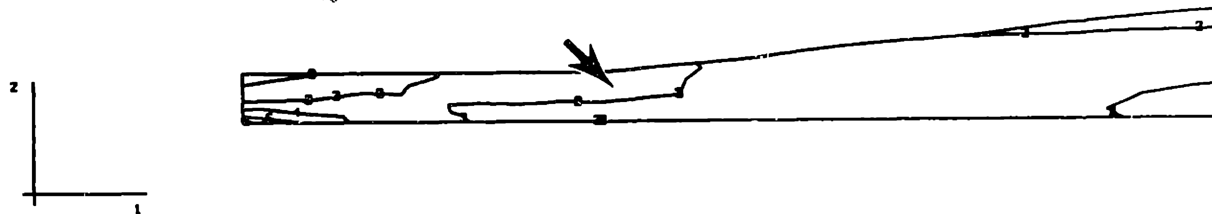

SOLDER JOINT AT 100 C. FIRST HYSTERESIS LOOP

STEP 5 INCREMENT 13

Figure 31: Equivalent plastic shear strain contours in the solder joint under the chip capacitor

I.D.	Value
1	$+0.00 \times 10^{0}$
2	$+3.33 \times 10^{-2}$
3	$+6.66 \times 10^{-2}$
4	$+1.00 \times 10^{-1}$
5	$+1.33 \times 10^{-1}$
6	$+1.66 \times 10^{-1}$
7	$+2.00 \times 10^{-1}$

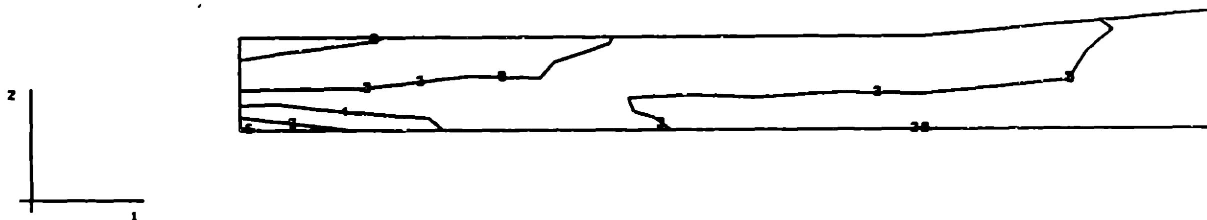

SOLDER JOINT AT 100 C, FIRST HYSTERESIS LOOP

Figure 32: Equivalent plastic shear strain contours in solder joint under the chip capacitor, leftmost eight elements .

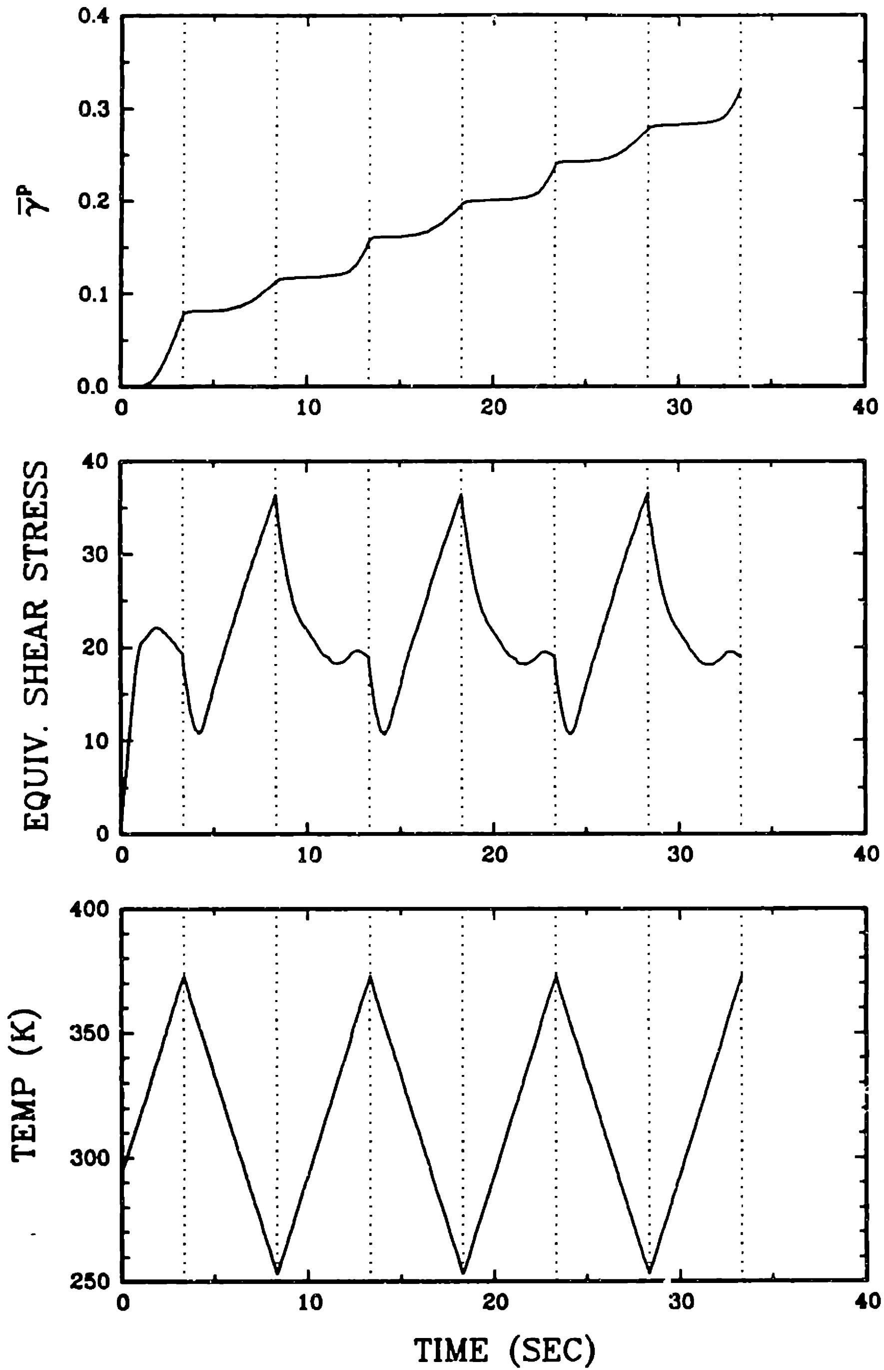

Figure 33: Data from the integration point shown in the contour plot of equivalent plastic strain.

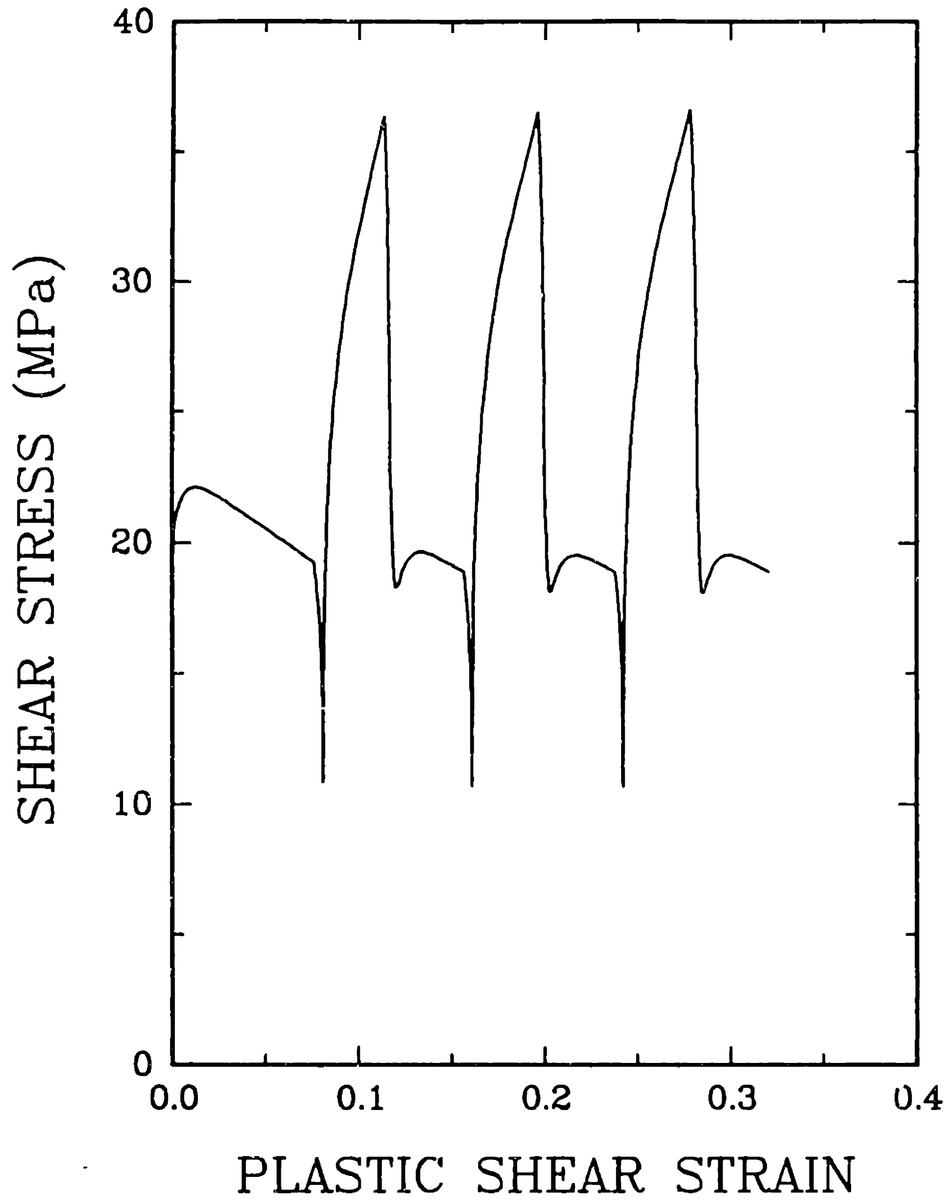

Figure 34: Equivalent stress-strain curve

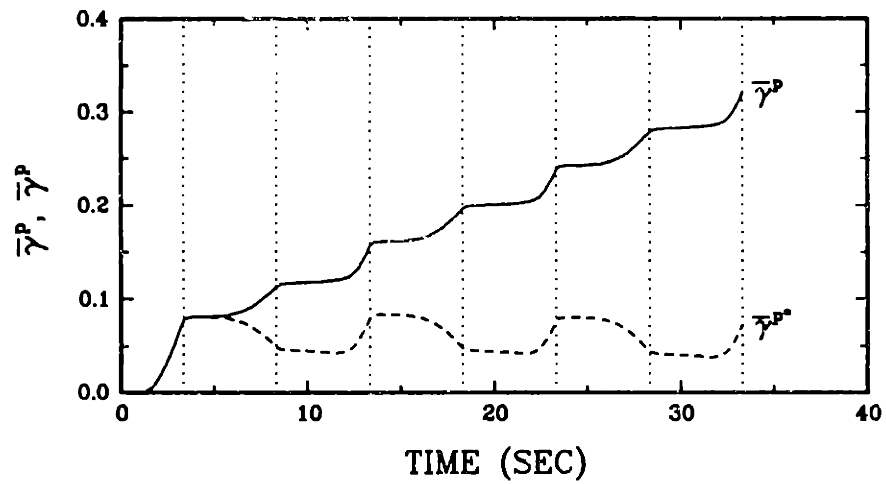

Figure 35: Comparison of the equivalent plastic shear strain and the signed equivalent plastic shear strain. The dotted line is the signed equivalent shear strain γ^{p*}.

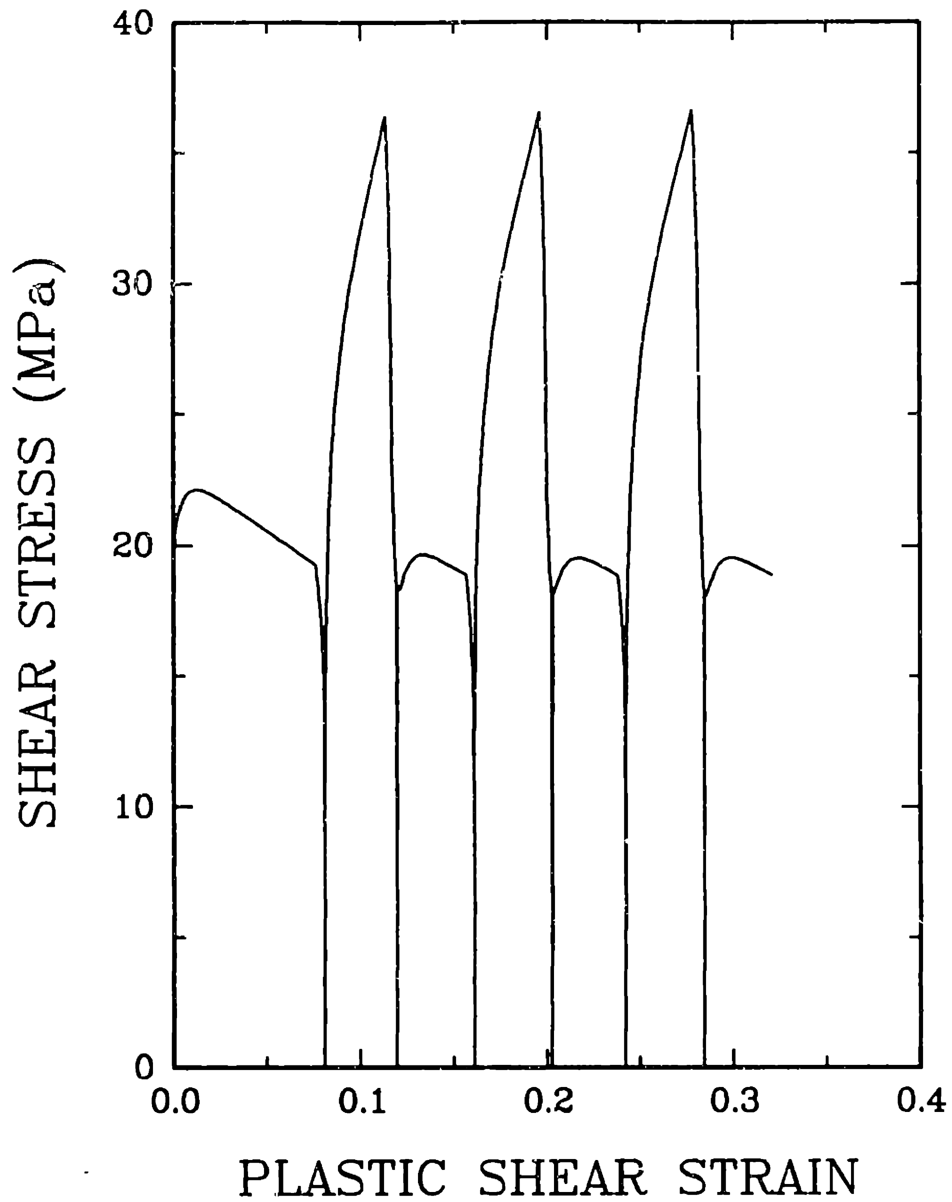

Figure 36: Equivalent stress-strain curve with added data points at zero stress

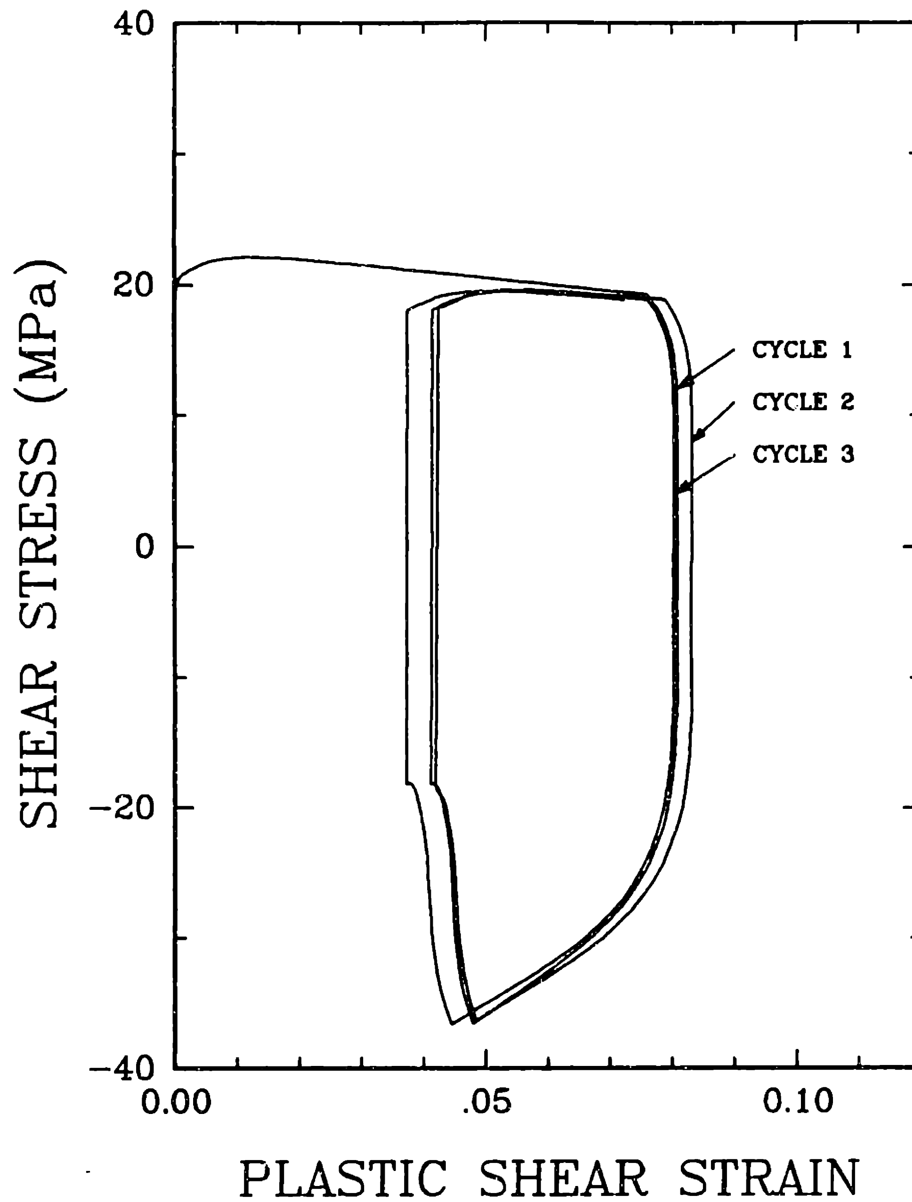

Figure 37: Hysteresis loops for an integration point in the solder joint during thermal cycling.

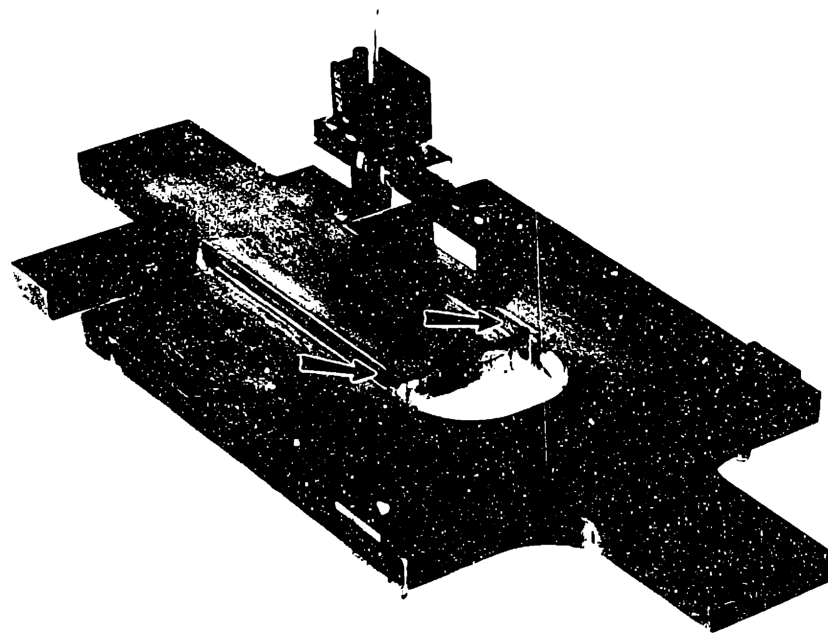

Figure 38: View of specimen showing placement of extensometer

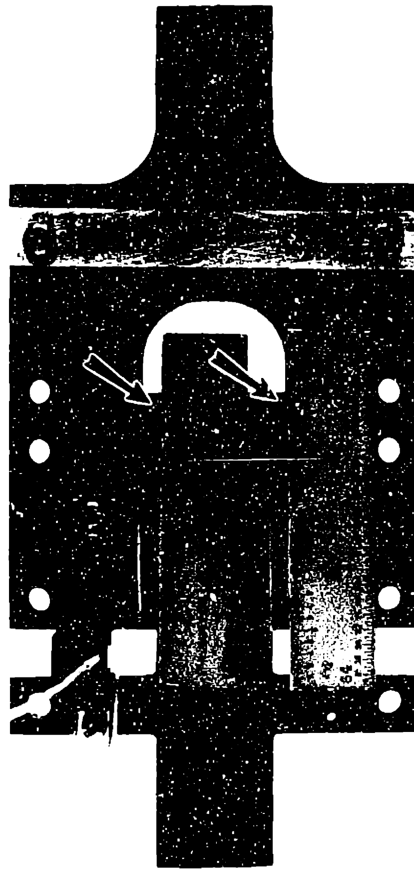

Figure 39: Front view of specimen ready for testing

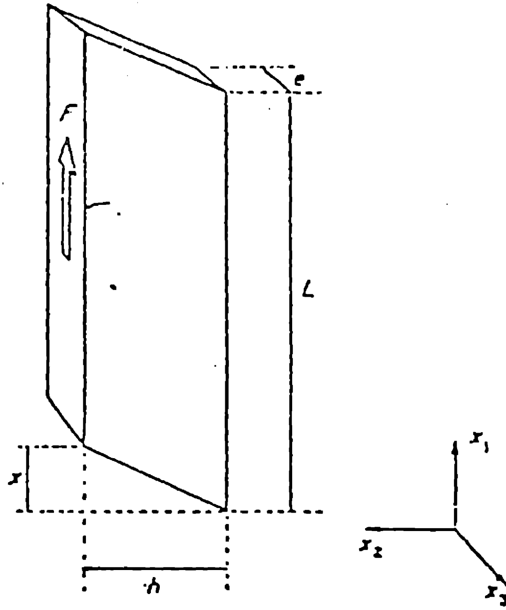

Figure 40: Definition of the reference axes and dimensions of a parallelopedic piece of material deformed in simple shear, from Ref. [30].

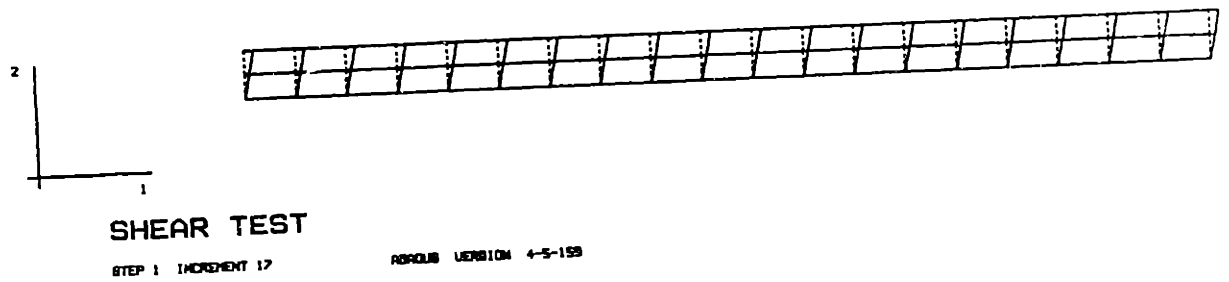

Figure 41: Deformed shear mesh: the original mesh is shown in dotted lines; the displacement magnification is 10x

I.D.	Value
1	$-2.00 \times 10^{+1}$
2	$-1.00 \times 10^{+1}$
3	$+0.00 \times 10^{0}$
4	$+1.00 \times 10^{+1}$
5	$+2.00 \times 10^{+1}$

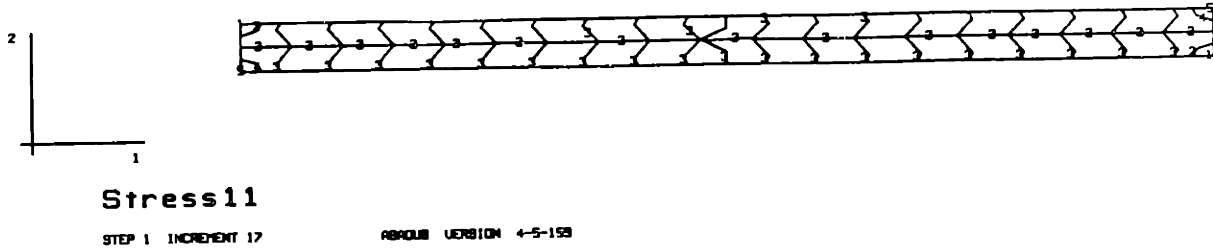

Figure 42: σ_{11} contours

I.D.	Value
1	$-2.00 \times 10^{+1}$
2	$-1.00 \times 10^{+1}$
3	$+0.00 \times 10^{0}$
4	$+1.00 \times 10^{+1}$
5	$+2.00 \times 10^{+1}$

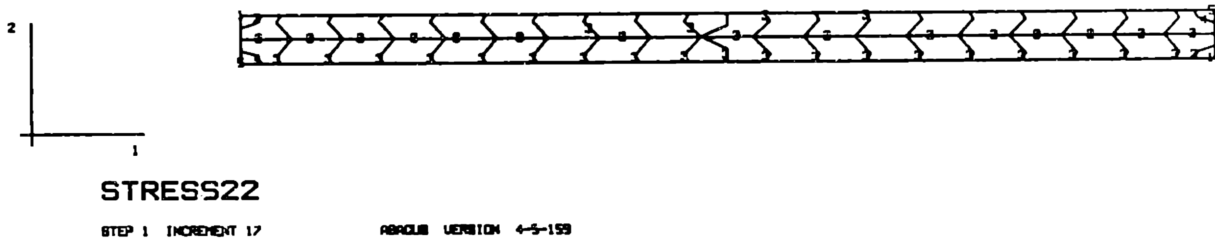

Figure 43: σ_{22} contours

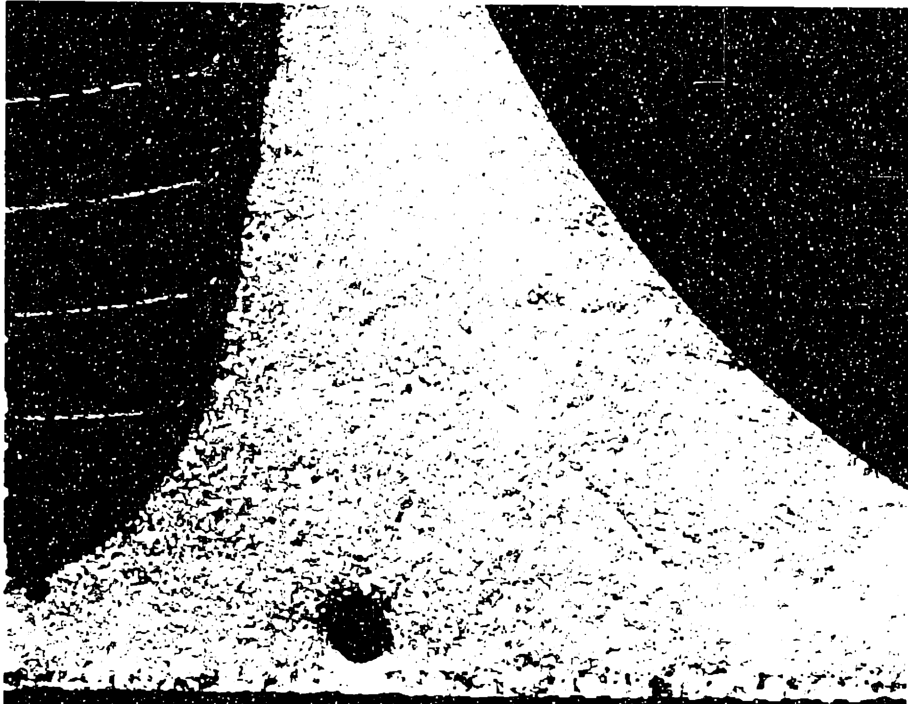

Figure 44: SEM micrograph of the solder joint shown in Figure 21. Compare this microstructure to the following micrographs of the shear fatigue specimens. The magnification is 253×.

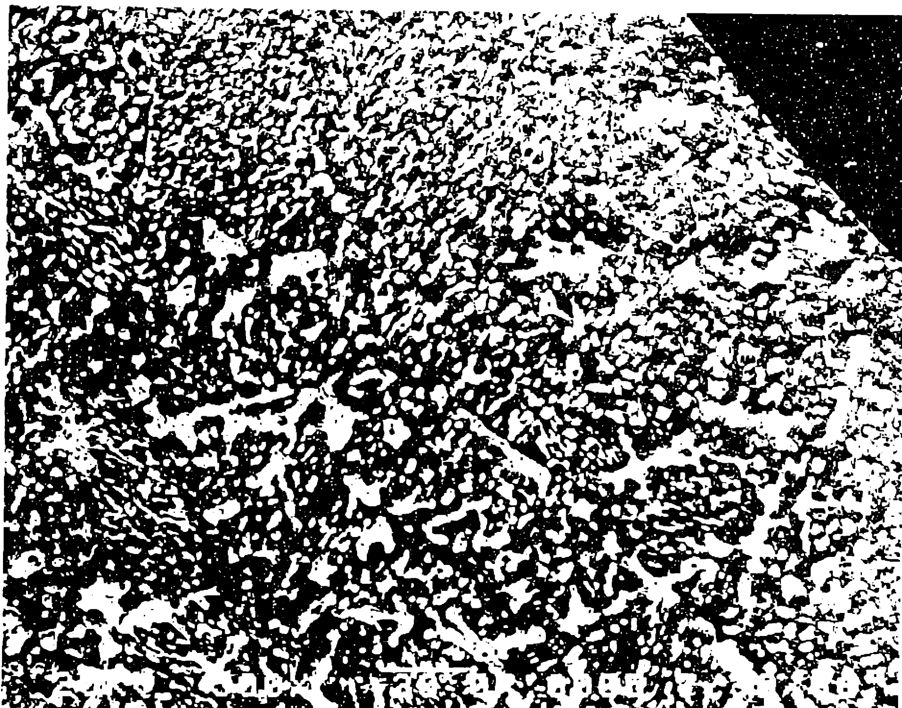

Figure 45: Same solder joint as shown above; the magnification is 500×.

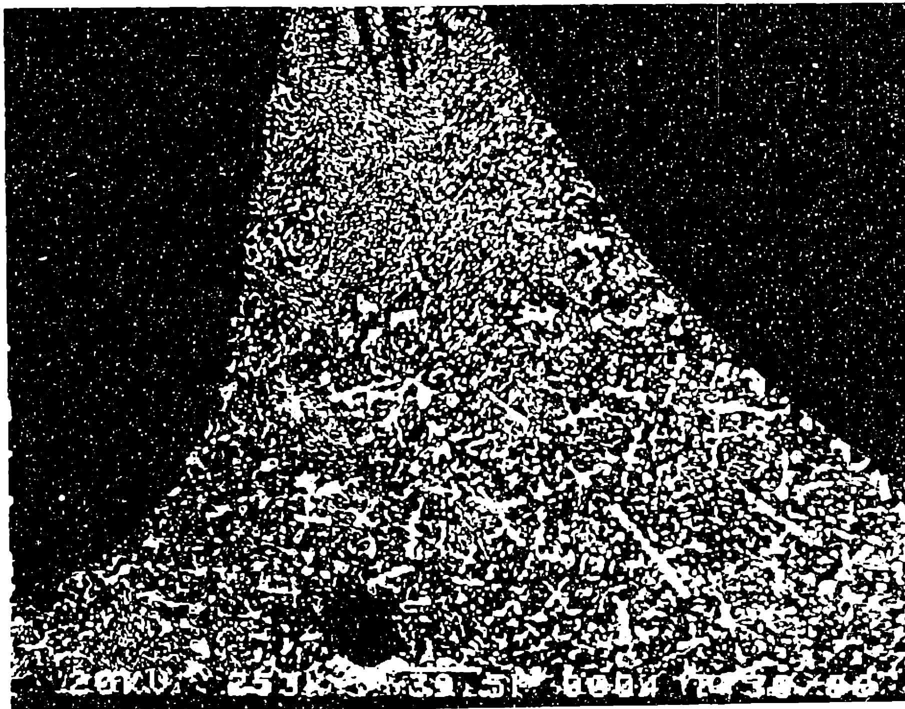

Figure 44: SEM micrograph of the solder joint shown in Figure 21. Compare this microstructure to the following micrographs of the shear fatigue specimens. The magnification is 253×.

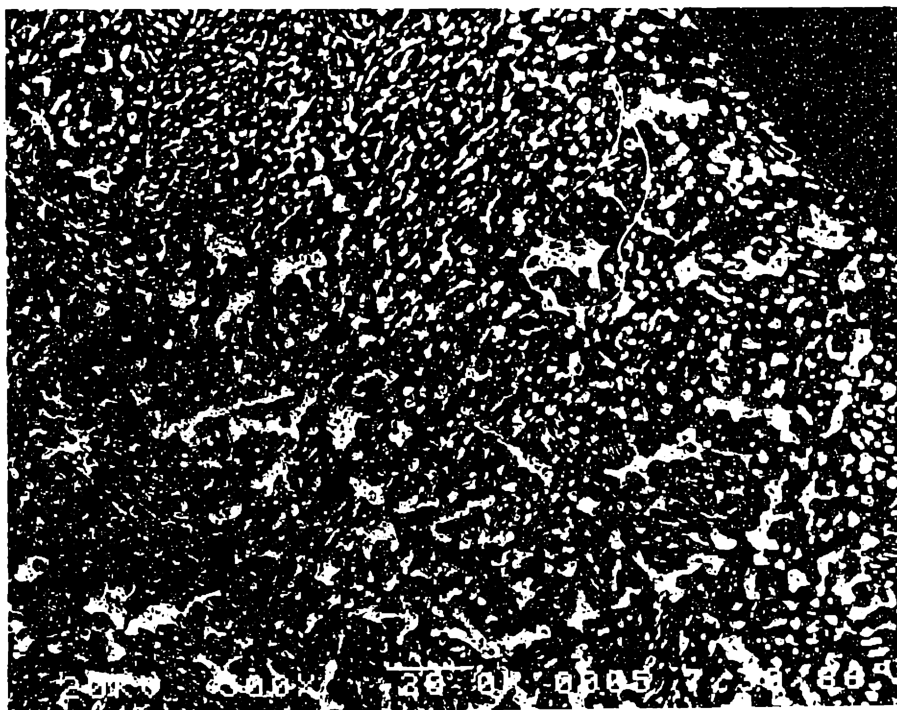

Figure 45: Same solder joint as shown above; the magnification is 500×.

INTENTIONAL DUPLICATE EXPOSURE

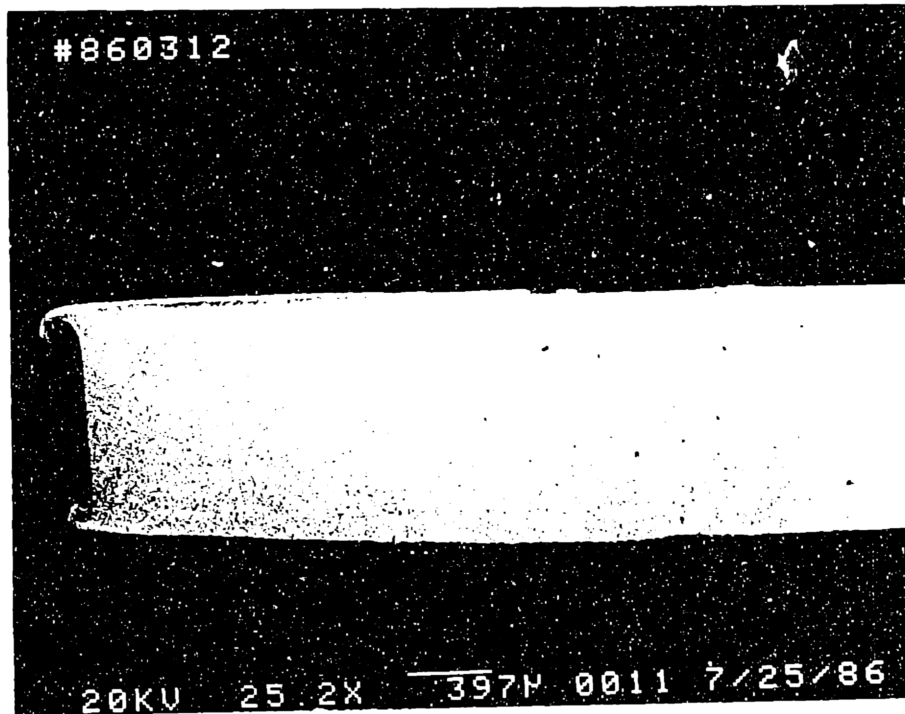

Figure 46: Specimen #860312; received ultrasonic vibration during solidification. Air cooled to room temperature and then heat treated at 170 ° C for 2 hours. Magnification is 25.2×.

Figure 46: Specimen #860312; received ultrasonic vibration during solidification. Air cooled to room temperature and then heat treated at 170 ° C for 2 hours. Magnification is 25.2×.

INTENTIONAL DUPLICATE EXPOSURE

Figure 47: Specimen #860305; received no ultrasonic vibration during solidification. Air cooled to room temperature; heat treated at 170° C for 2 hours. Magnification 19.8×.

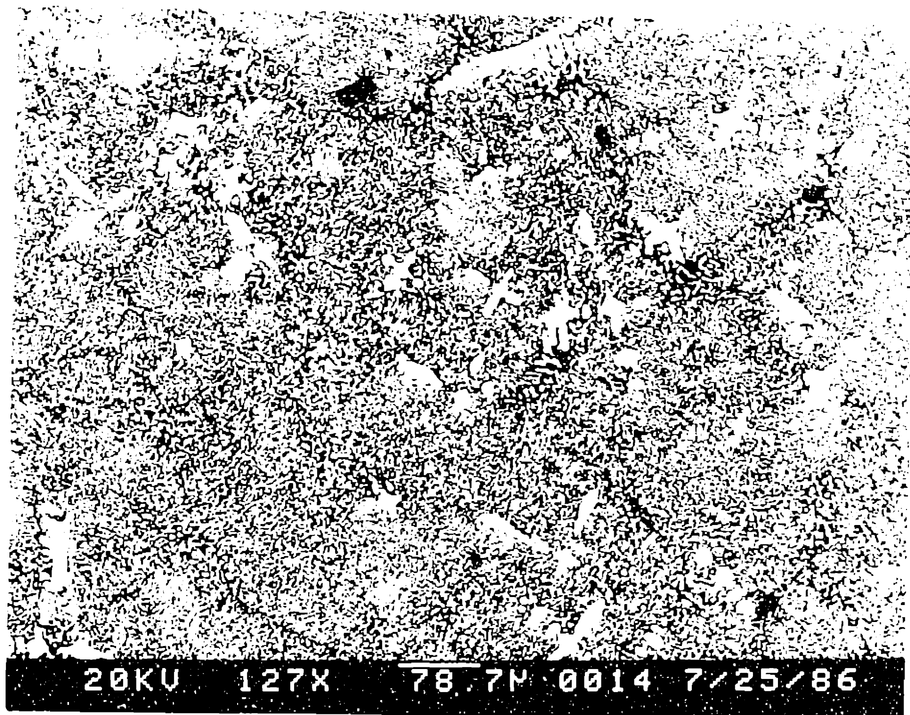

Figure 48: Specimen #860312; received ultrasonic vibration during solidification. Air cooled to room temperature; heat treated at 170 ° C for 2 hours. Magnification is 127×.

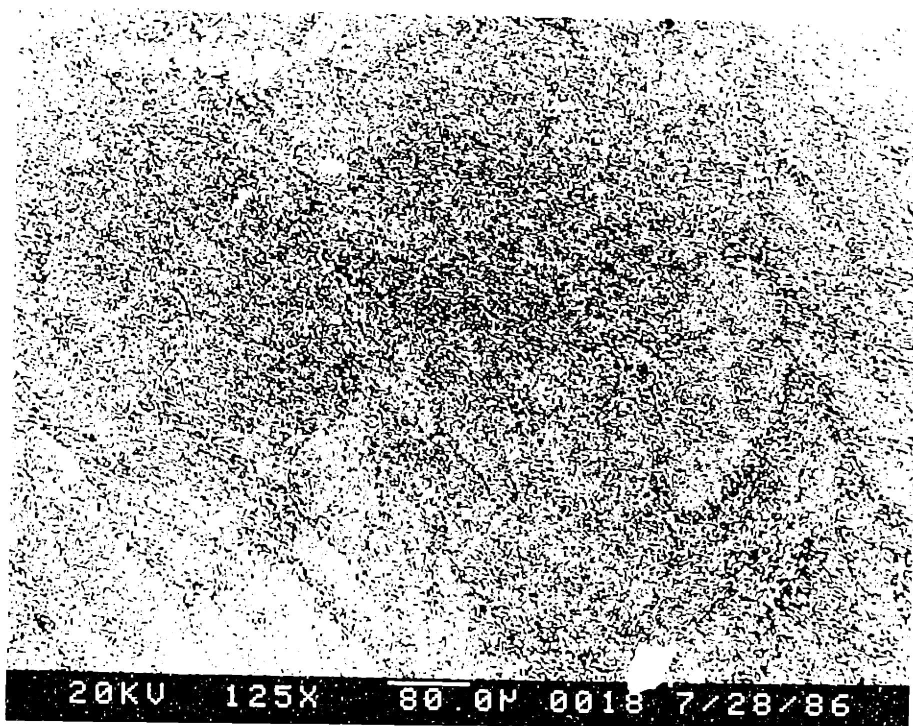

Figure 49: Specimen #860305; no ultrasonic vibration during solidification. Air cooled to room temperature; heat treated at 170° C for 2 hours. Magnification 125×.

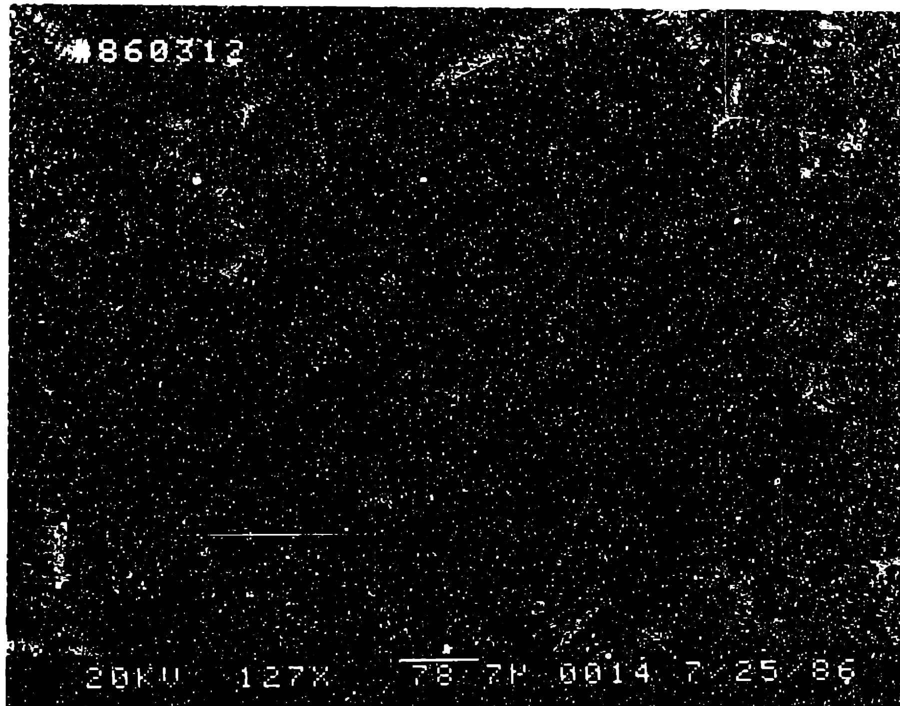

Figure 48: Specimen #860312; received ultrasonic vibration during solidification. Air cooled to room temperature; heat treated at 170 ° C for 2 hours. Magnification is 127×.

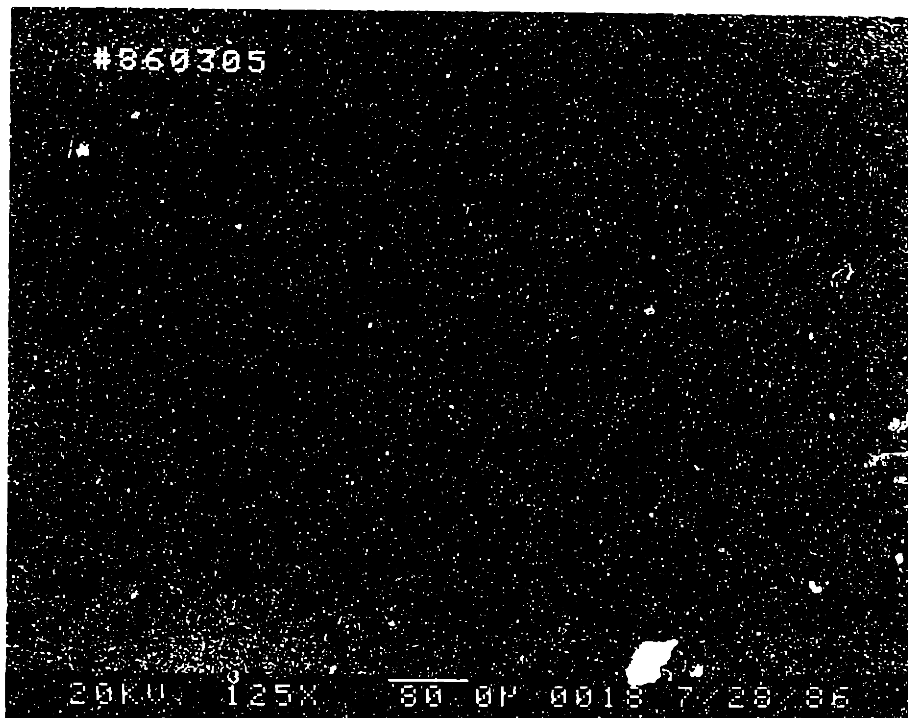

Figure 49: Specimen #860305; no ultrasonic vibration during solidification. Air cooled to room temperature; heat treated at 170° C for 2 hours. Magnification 125×.

INTENTIONAL DUPLICATE EXPOSURE

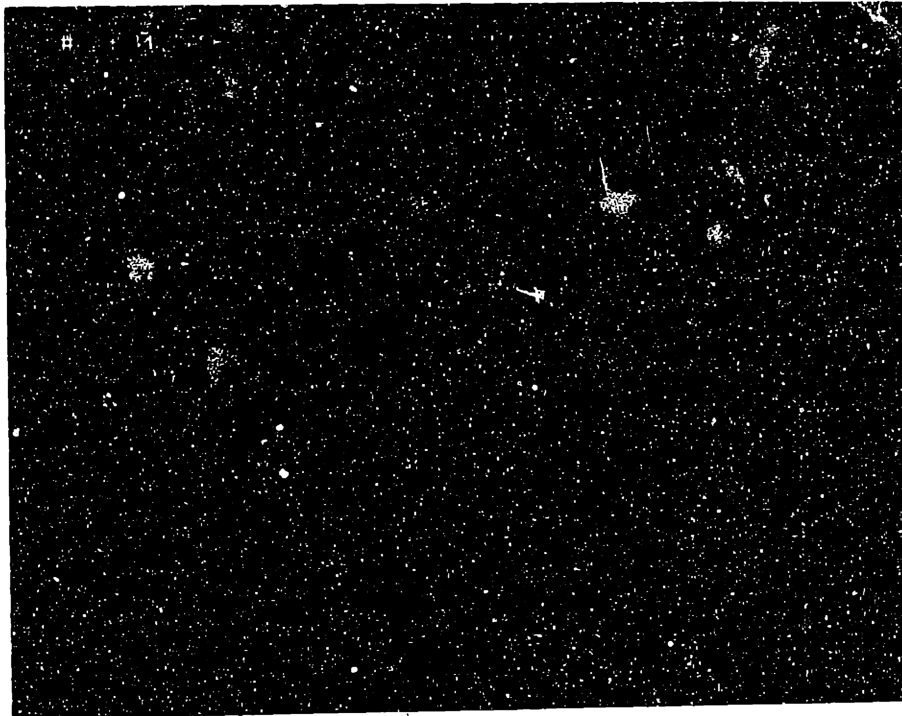

Figure 50: Specimen #860206; no ultrasonic vibration during solidification. Air cooled to room temperature. No solder was removed from the top or bottom of this sample. The bottom of the joint during casting is to the right. Magnification 15.2×.

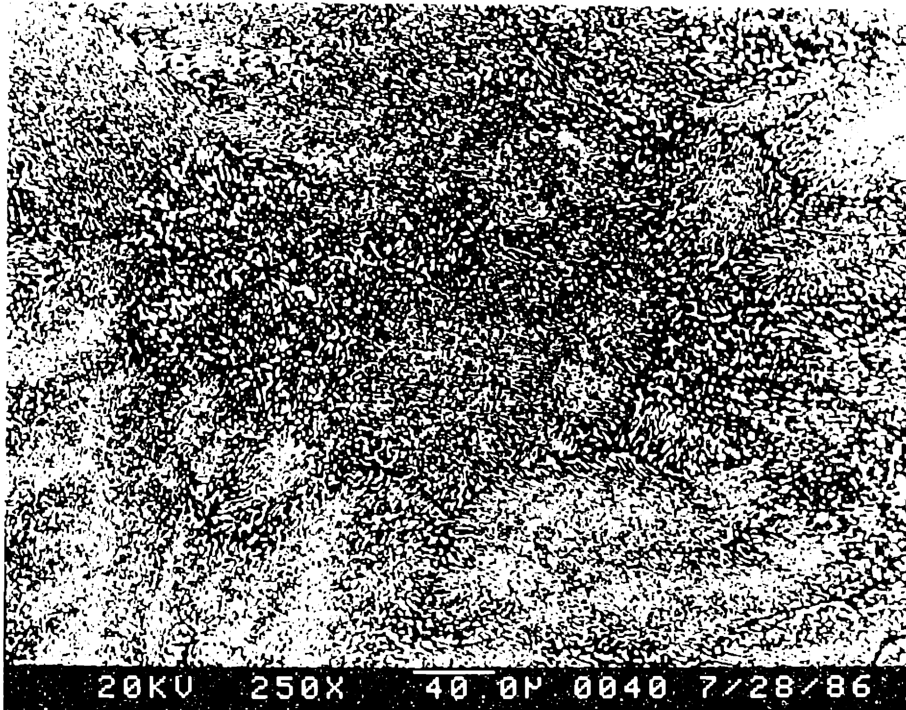

Figure 51: Specimen #860327; air cooled; magnification 250×.

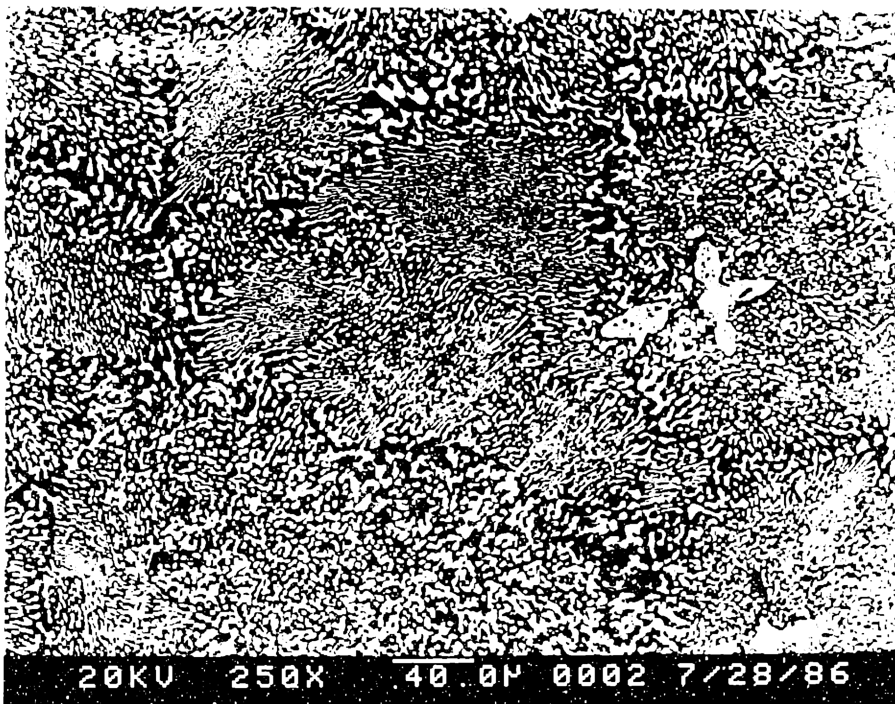

Figure 52: Specimen #860312; air cooled followed by 2 hours at 170° C; magnification 250×. Both of these specimens were ultrasonically vibrated. The photos were taken from areas with few dendrites so that the eutectic matrix could be compared.

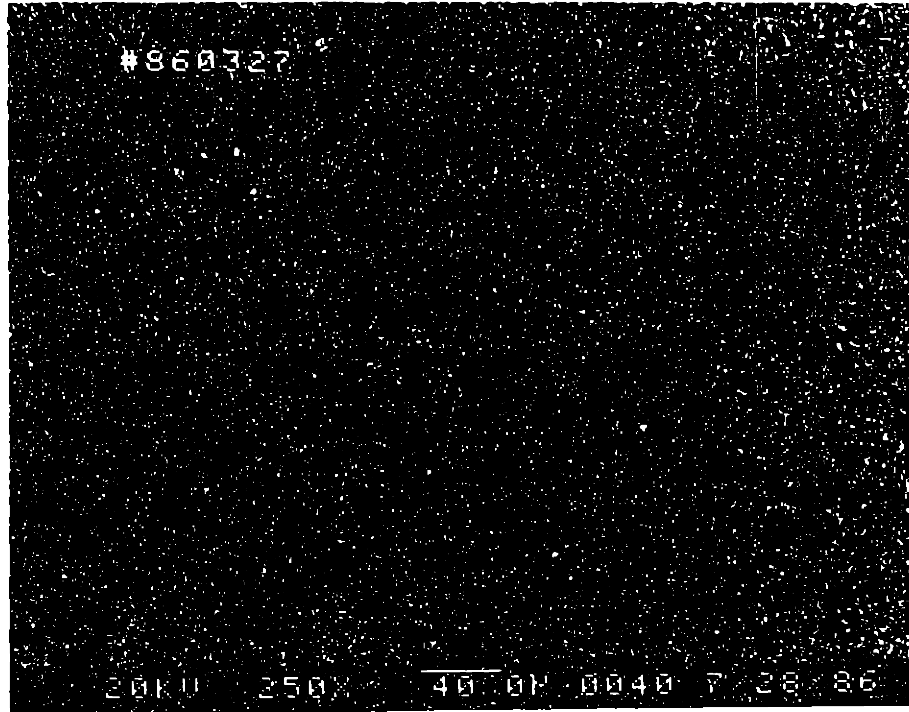

Figure 51: Specimen #860327; air cooled; magnification 250×.

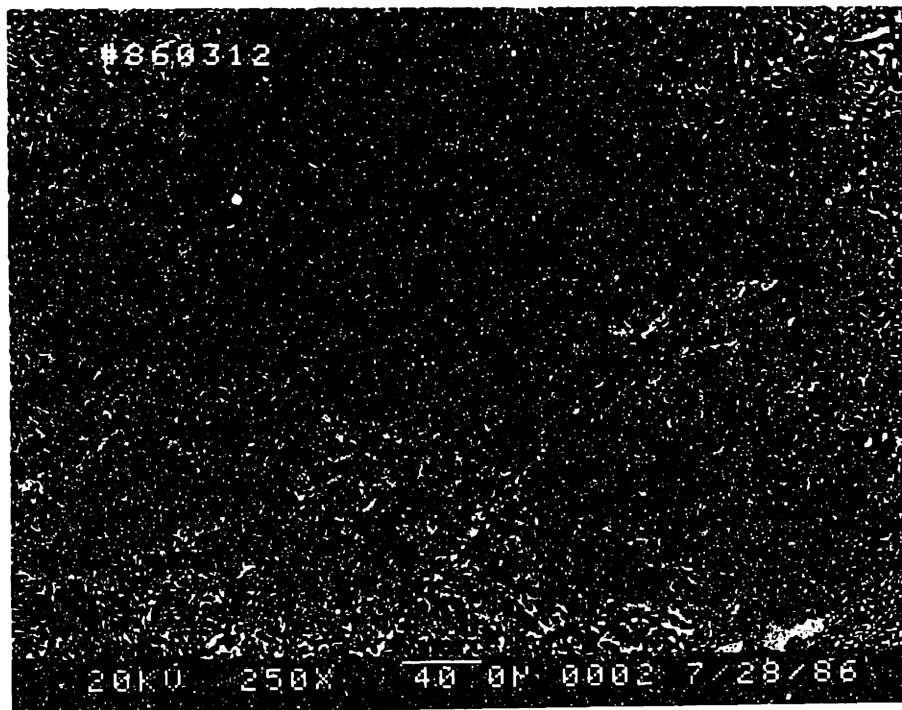

Figure 52: Specimen #860312; air cooled followed by 2 hours at 170° C; magnification 250×. Both of these specimens were ultrasonically vibrated. The photos were taken from areas with few dendrites so that the eutectic matrix could be compared.

INTENTIONAL DUPLICATE EXPOSUR

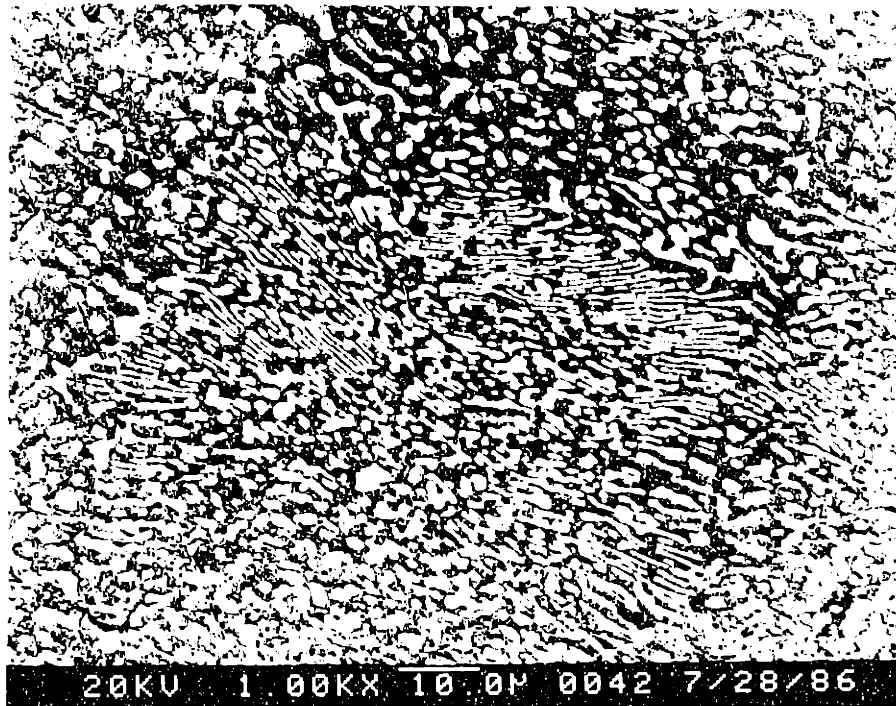

Figure 53: Specimen #860327; air cooled; magnification 1000×.

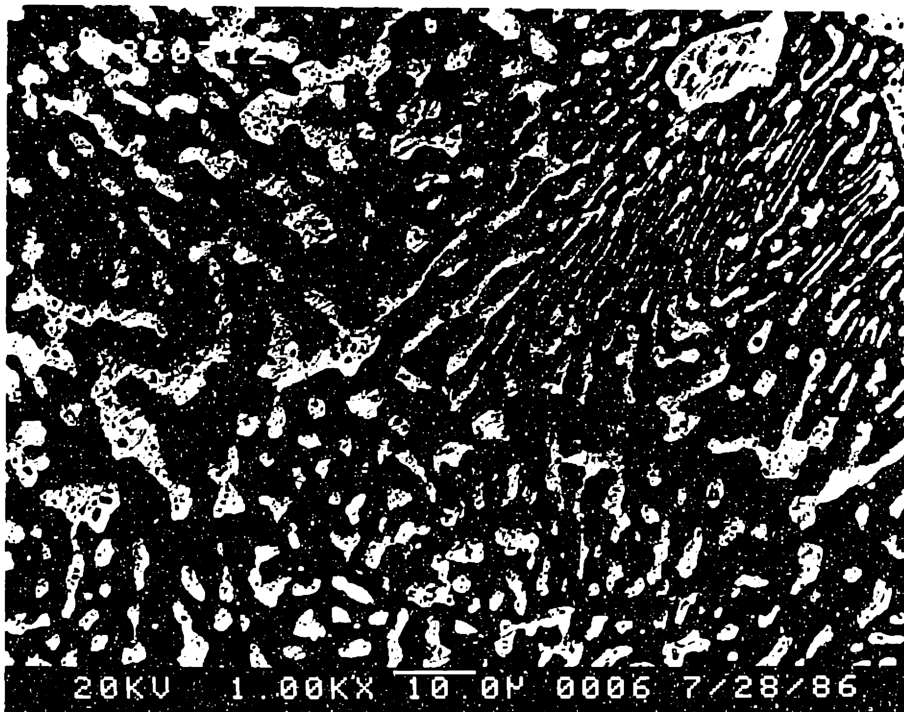

Figure 54: Specimen #860312; air cooled followed by 2 hours at 170° C; magnification 1000×. The specimens are the same as those on the previous page.

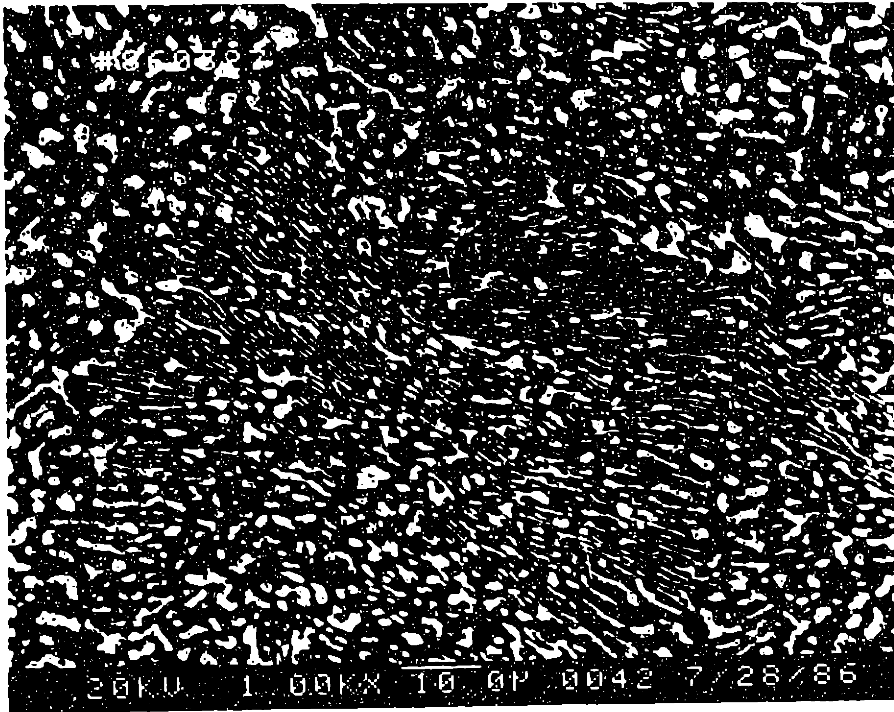

Figure 53: Specimen #860327; air cooled; magnification 1000×.

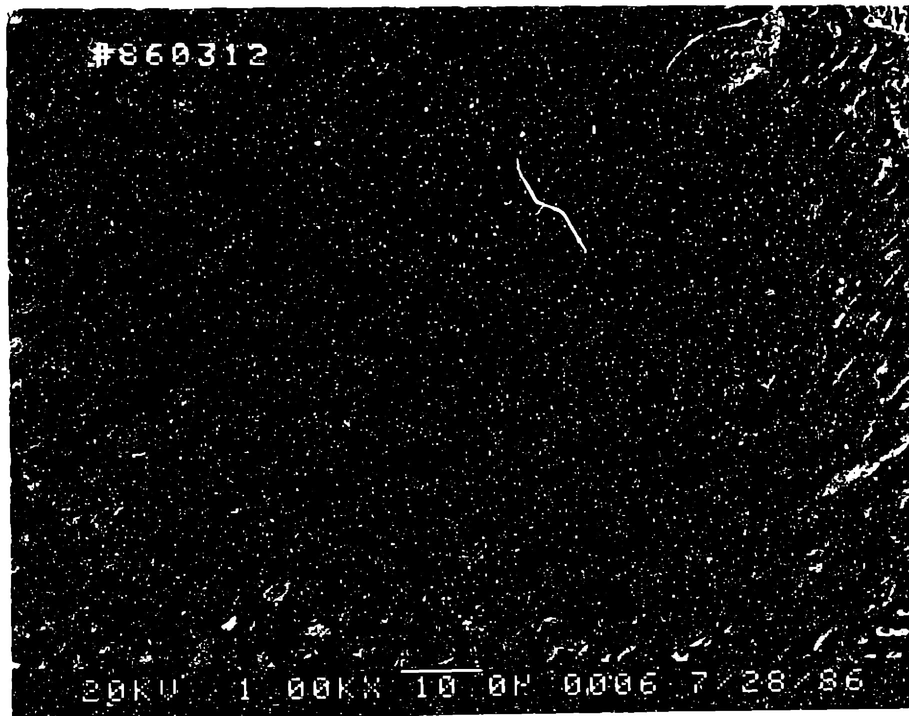

Figure 54: Specimen #860312; air cooled followed by 2 hours at 170° C; magnification 1000×. The specimens are the same as those on the previous page.

INTENTIONAL DUPLICATE EXPOSURE

Figure 55: Specimen #860302; air cooled. The magnification is 200×.

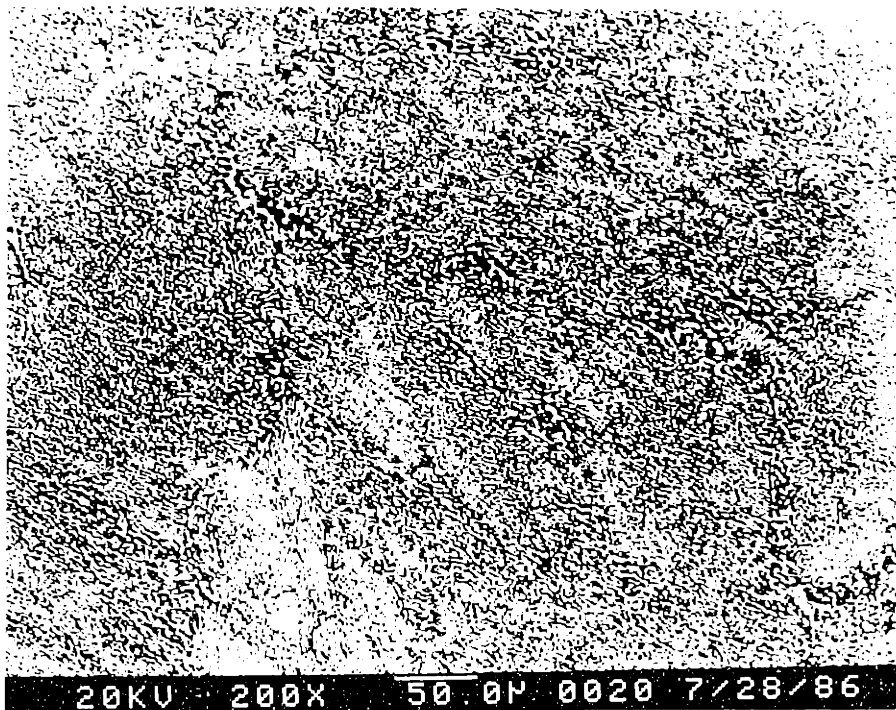

Figure 56: Specimen #860305; air cooled followed by 2 hours at 170° C. The magnification is 200×. These specimens received no ultrasonic vibration during solidification.

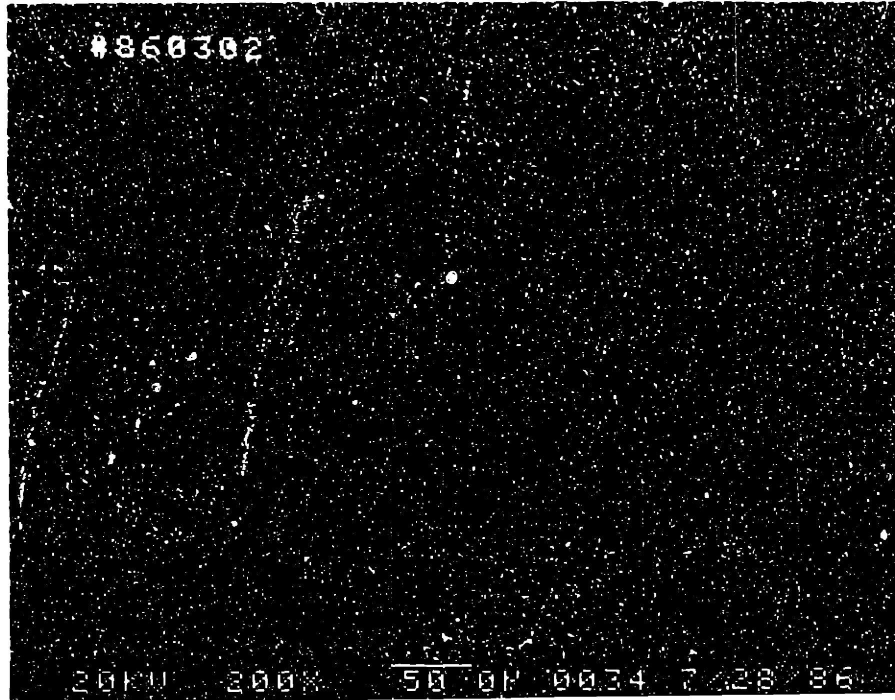

Figure 55: Specimen #860302; air cooled. The magnification is 200×.

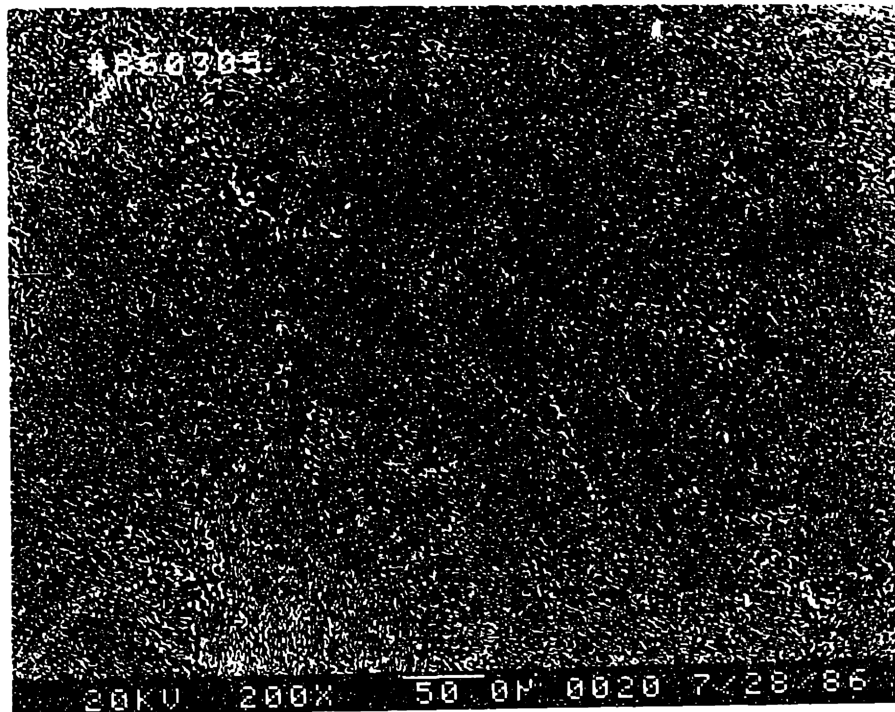

Figure 56: Specimen #860305; air cooled followed by 2 hours at 170° C. The magnification is 200×. These specimens received no ultrasonic vibration during solidification.

INTENTIONAL DUPLICATE EXPOSURE

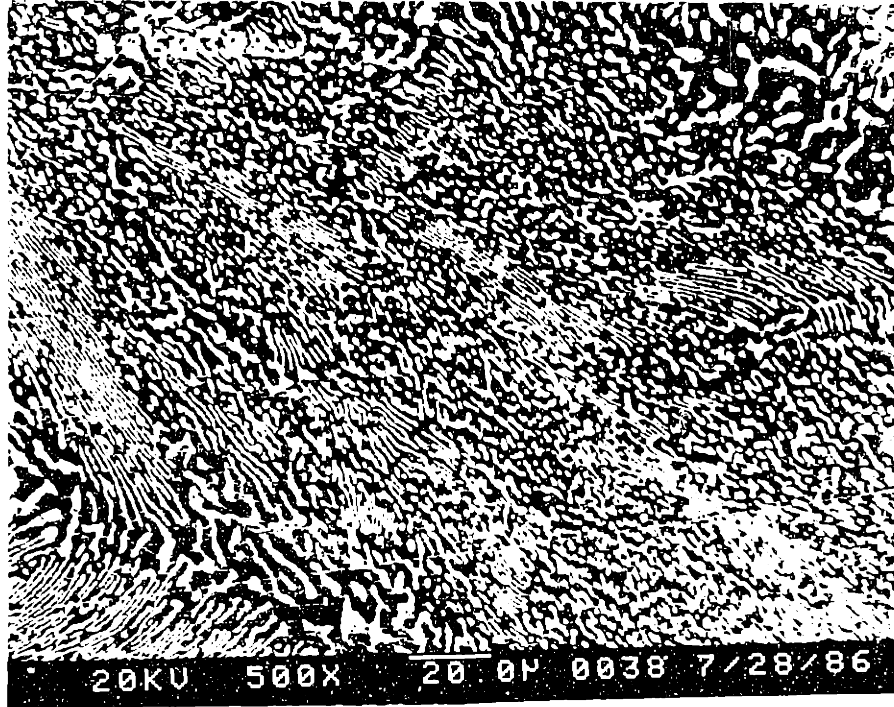

Figure 57: Specimen #860302; air cooled. The magnification is 500×.

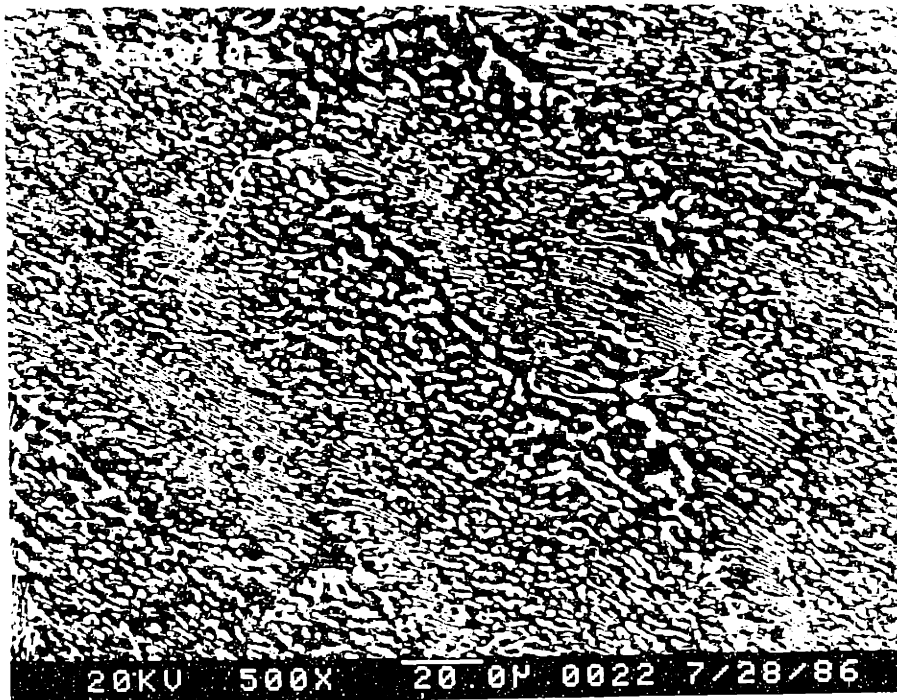

Figure 58: Specimen #860305; air cooled followed by 2 hours at 170° C. The magnification is 500×. These specimens are the same as those on the previous page.

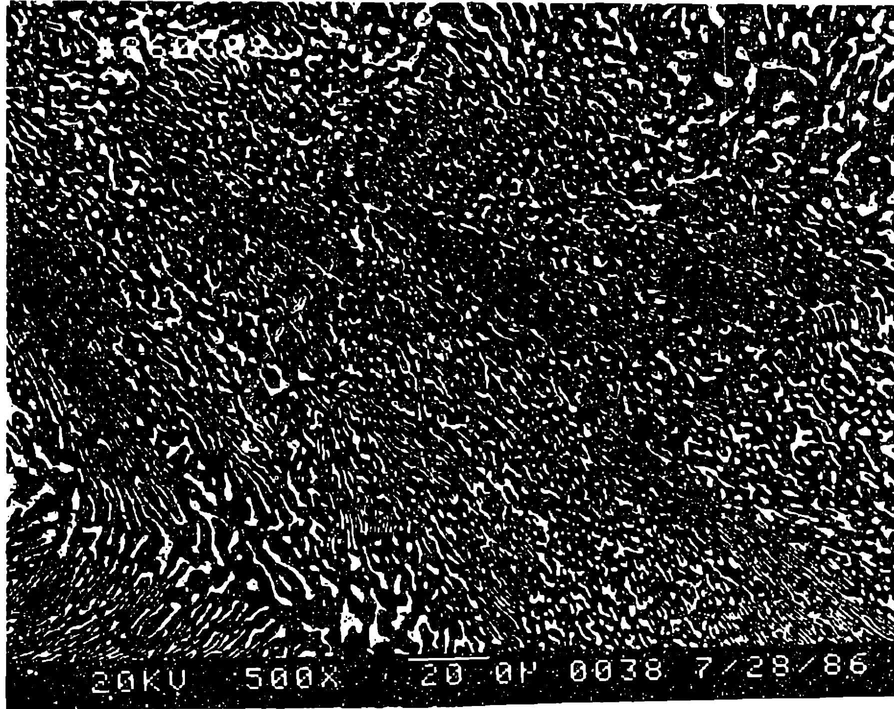

Figure 57: Specimen #860302; air cooled. The magnification is 500×.

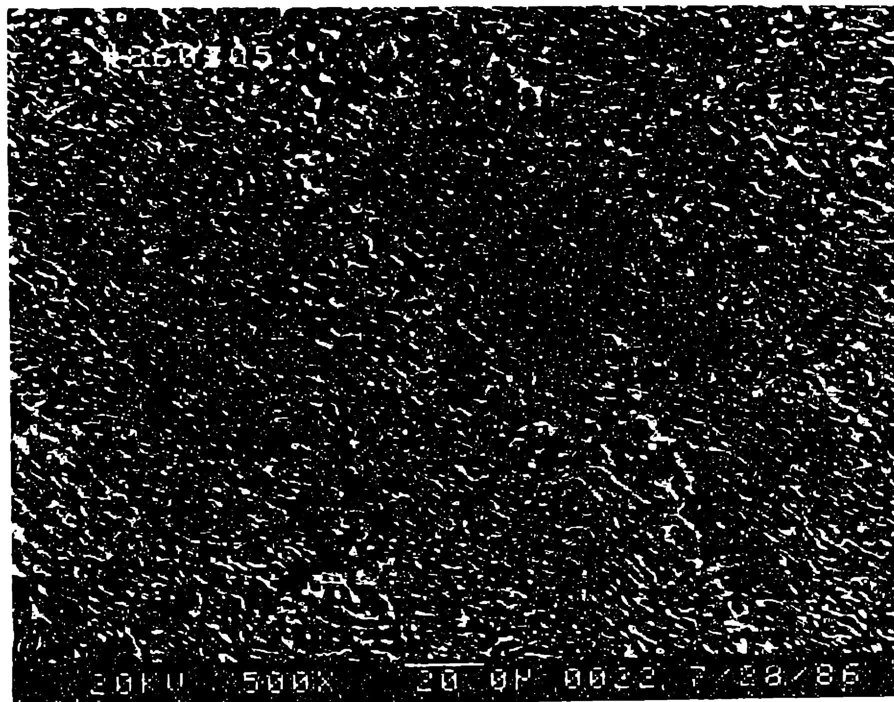

Figure 58: Specimen #860305; air cooled followed by 2 hours at 170° C. The magnification is 500×. These specimens are the same as those on the previous page.

INTENTIONAL DUPLICATE EXPOSURE

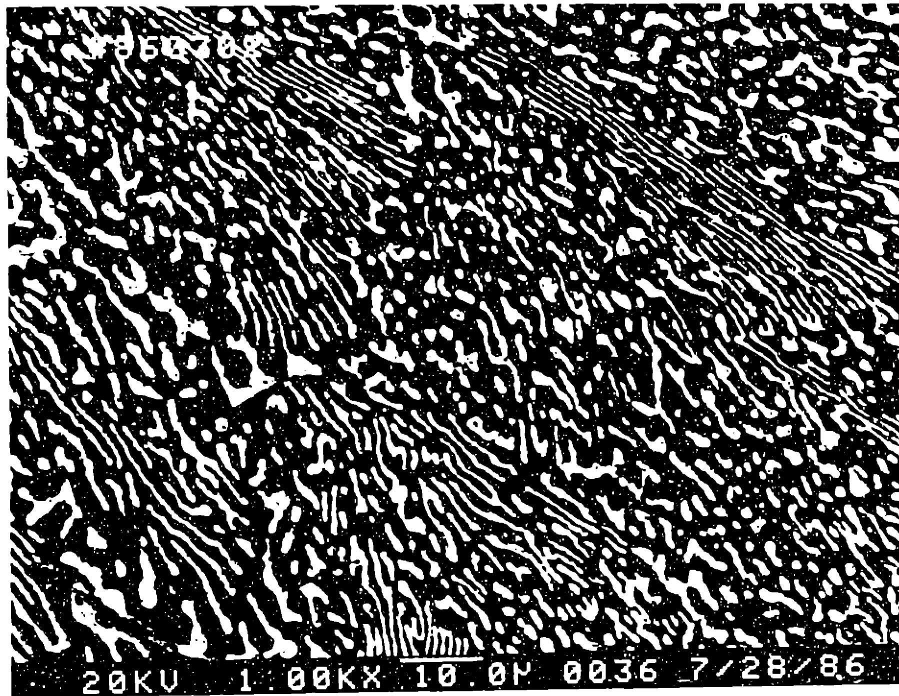

Figure 59: Specimen #860302; air cooled. The magnification is 1000×.

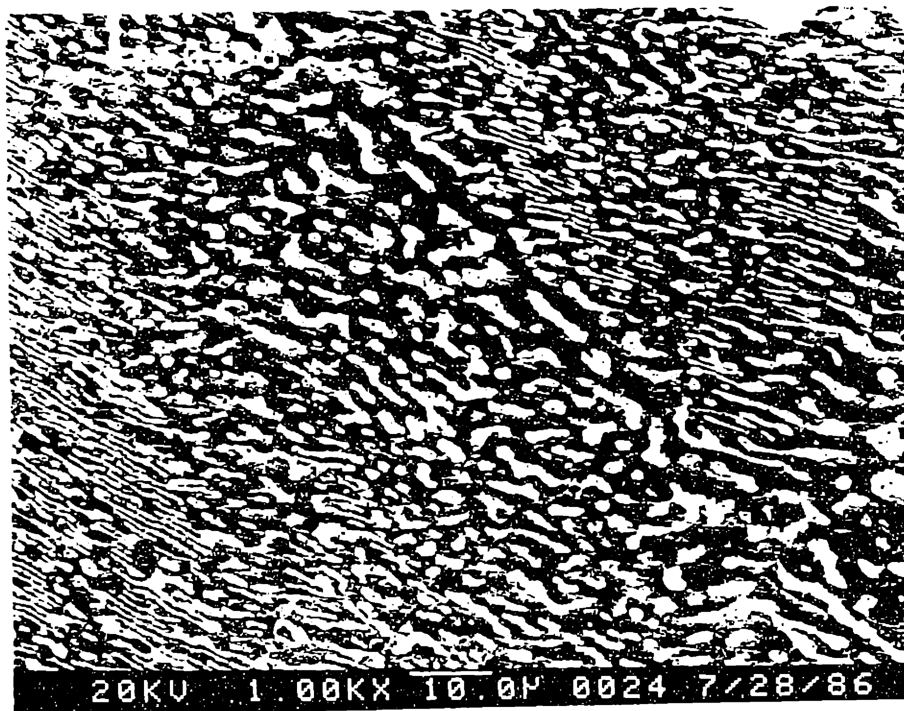

Figure 60: Specimen #860305; air cooled followed by 2 hours at 170° C. The magnification is 1000×. These specimens are the same as those on the previous page.

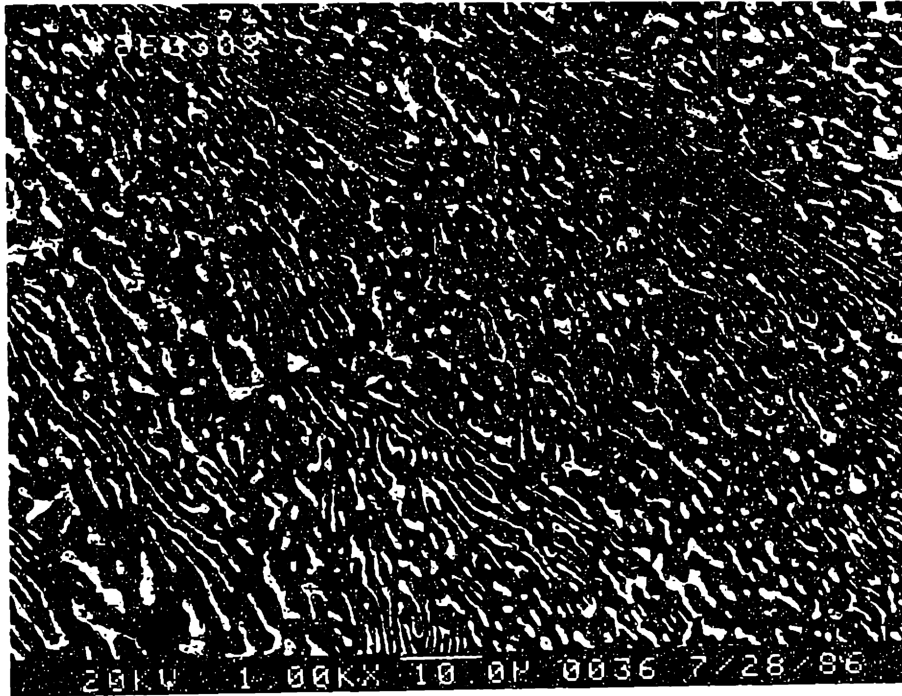

Figure 59: Specimen #860302; air cooled. The magnification is 1000×.

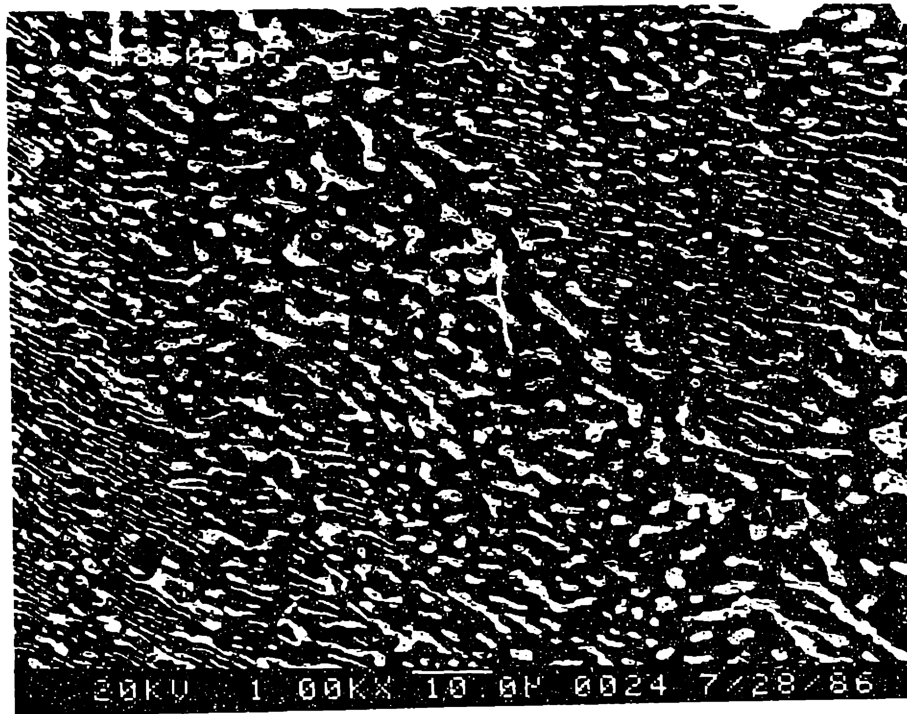

Figure 60: Specimen #860305; air cooled followed by 2 hours at 170° C. The magnification is 1000×. These specimens are the same as those on the previous page.

INTENTIONAL DUPLICATE EXPOSU

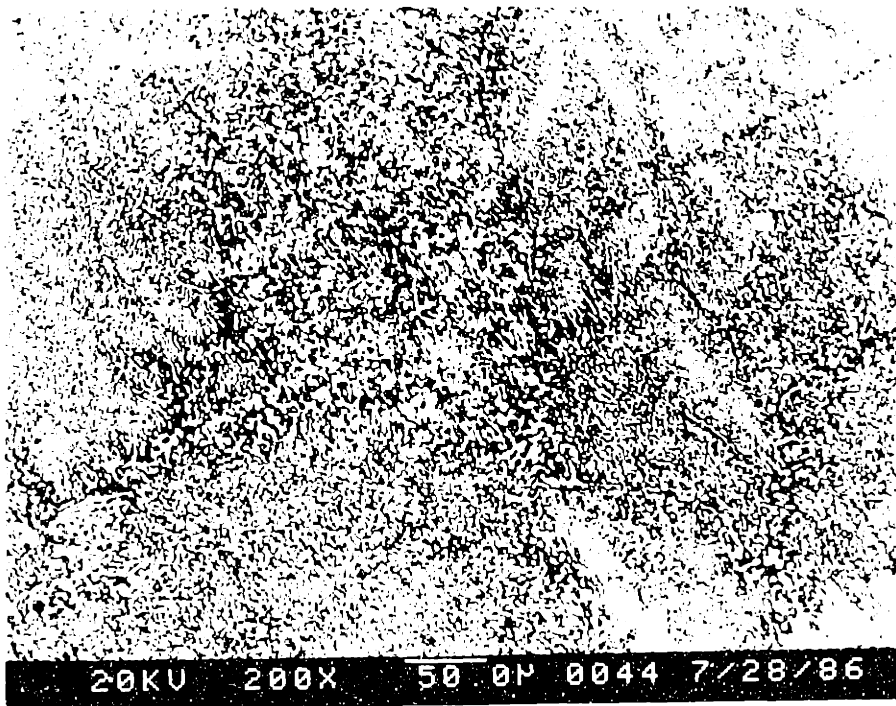

Figure 61: Specimen #860406; air cooled followed by 45 minutes at 170° C. The magnification is 200×.

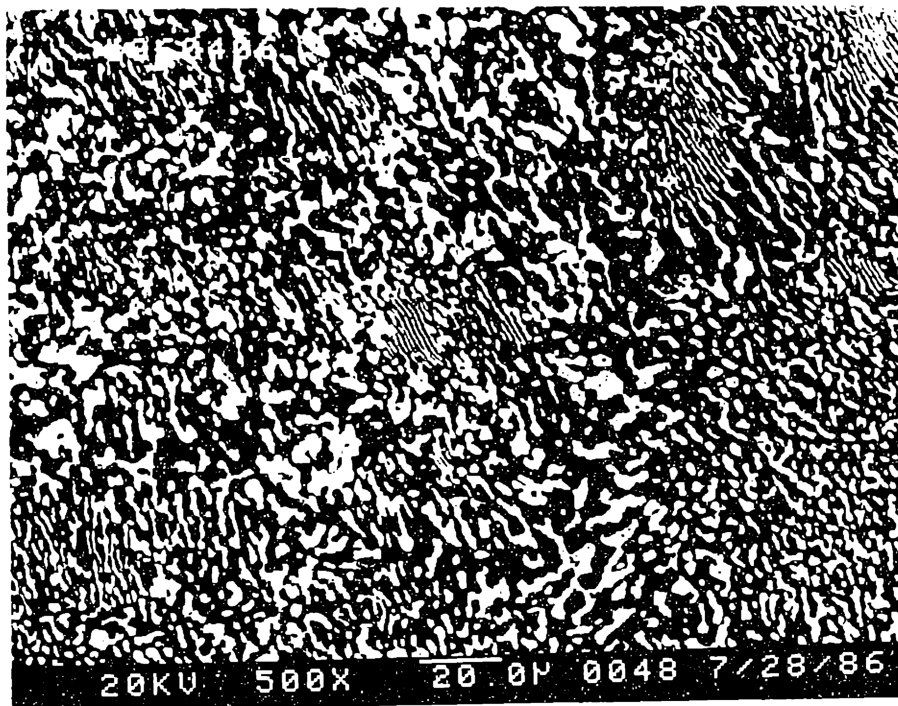

Figure 62: Specimen #860406; magnification 500×.

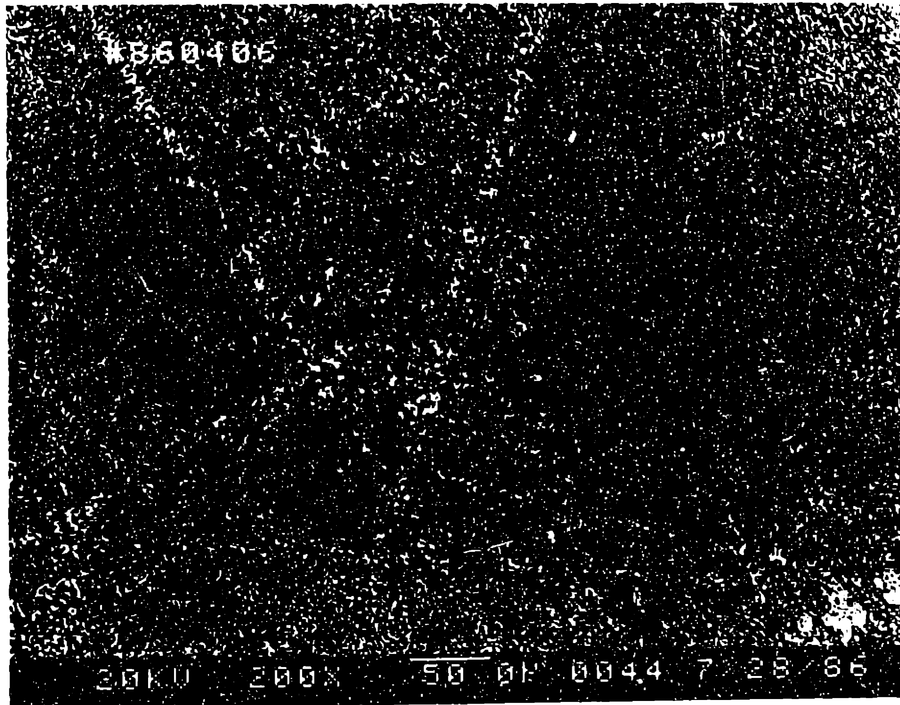

Figure 61: Specimen #860406; air cooled followed by 45 minutes at 170° C. The magnification is 200×.

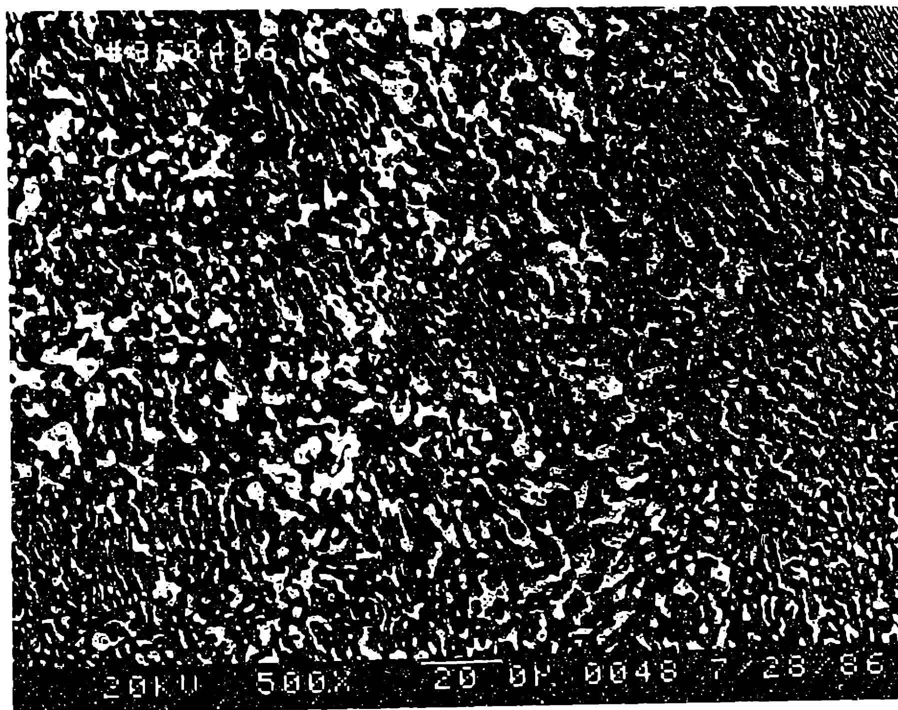

Figure 62: Specimen #860406; magnification 500×.

INTENTIONAL DUPLICATE EXPOSURE

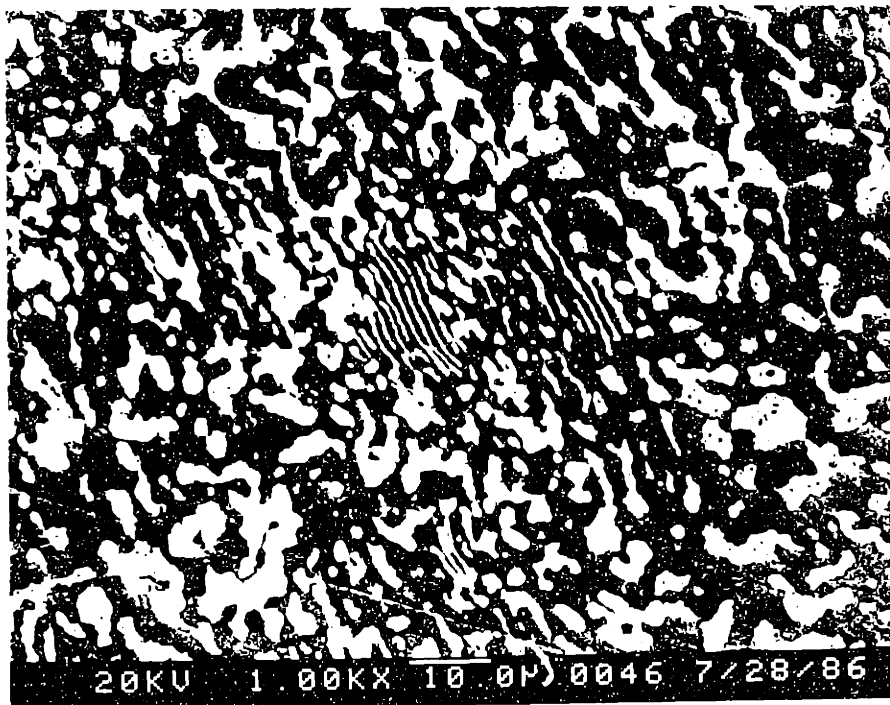

Figure 63: Specimen #860406; magnification 1000×.

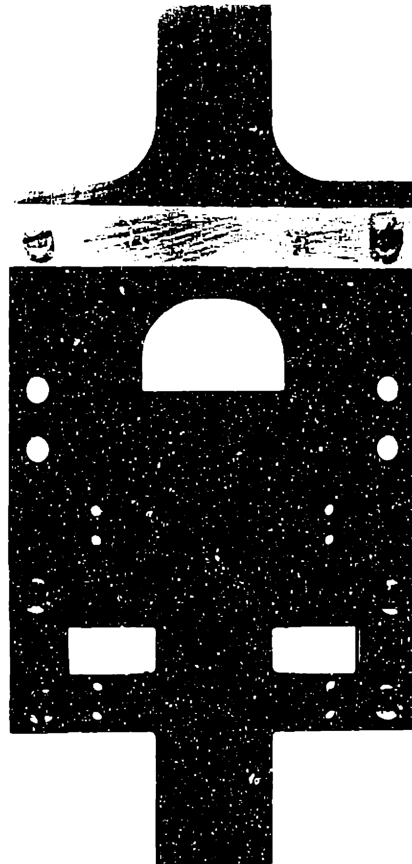

Figure 64: Fixture with clamps to keep solder joints from being strained before testing. The specimen is clamped together until it is mounted in the test machine and is at zero load.

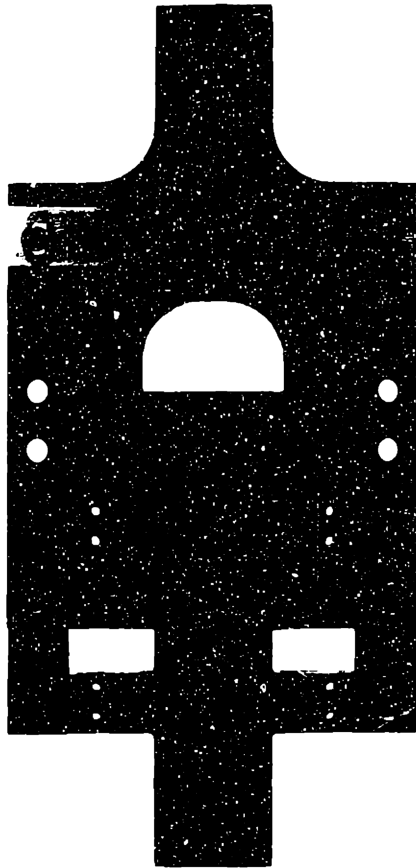

Figure 64: Fixture with clamps to keep solder joints from being strained before testing. The specimen is clamped together until it is mounted in the test machine and is at zero load.

INTENTIONAL DUPLICATE EXPOSURE

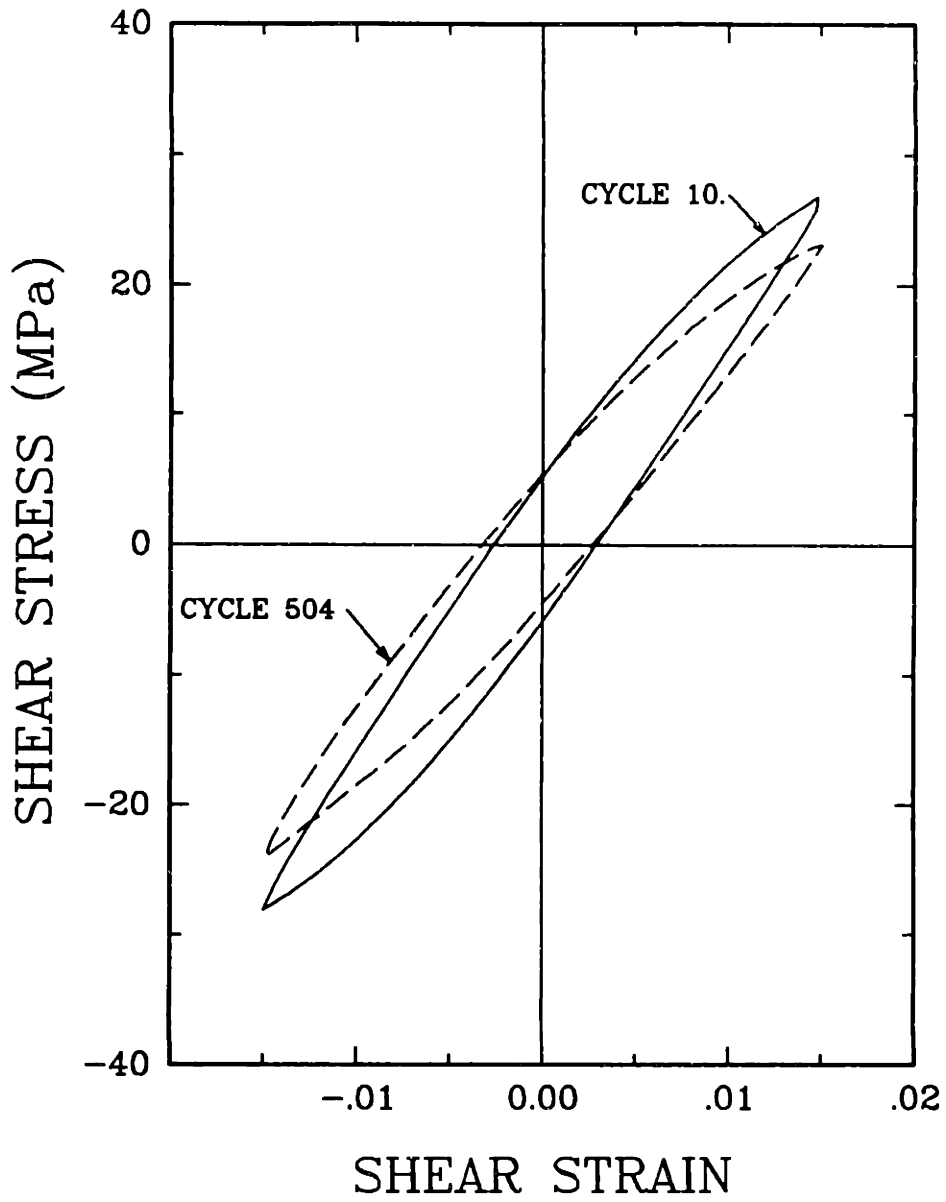

Figure 65: Hysteresis loops, shear strain range 3.0%

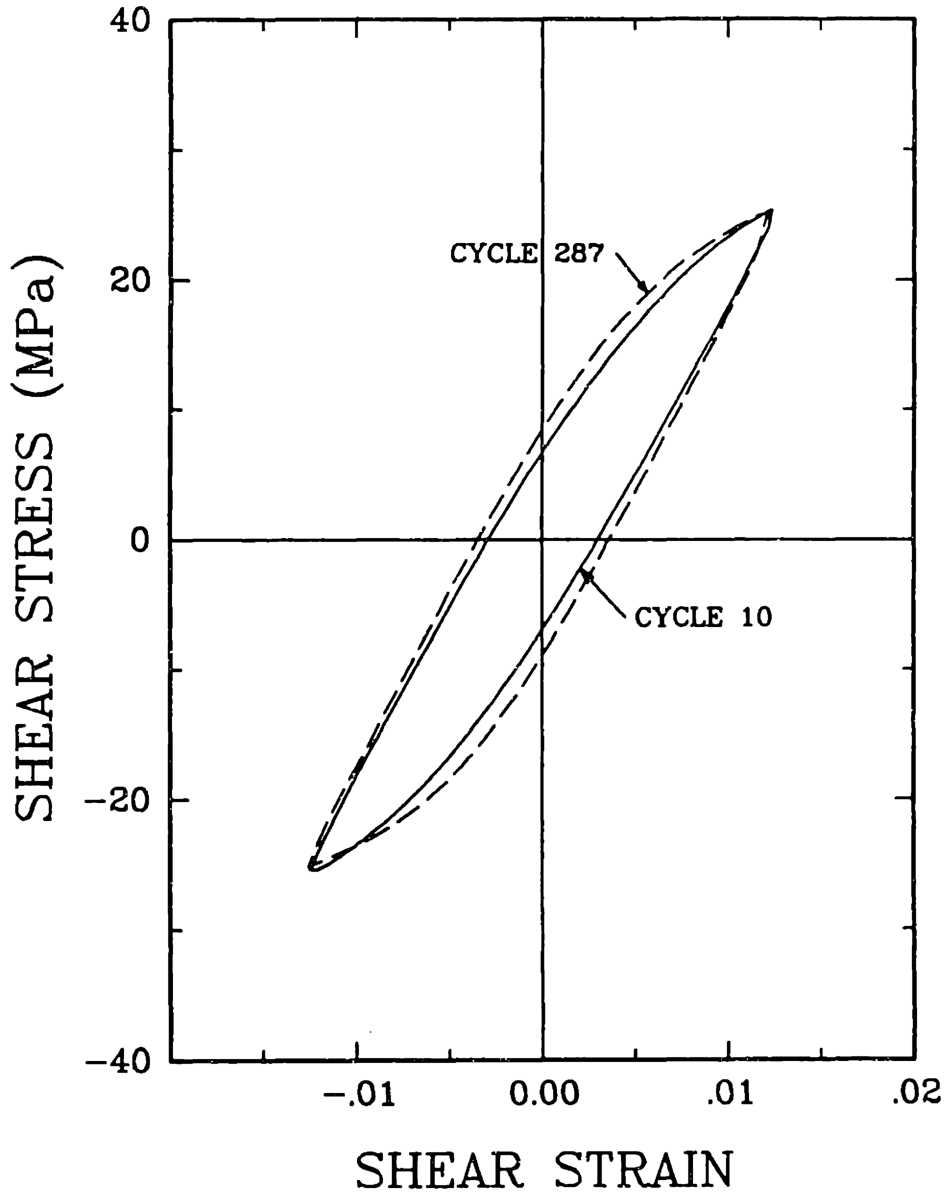

Figure 66: Hysteresis loops, shear strain range 2.5%

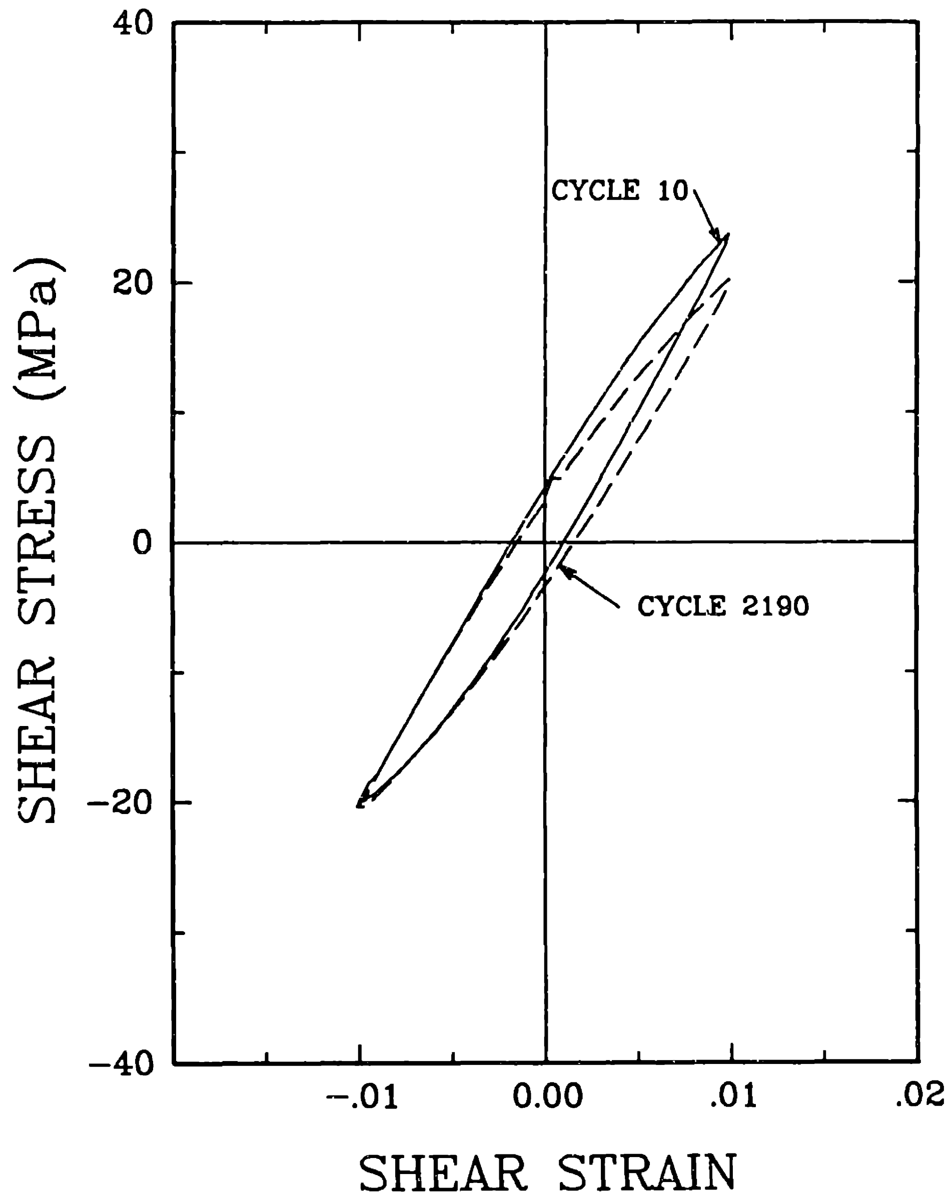

Figure 67: Hysteresis loops, shear strain range 2.0%

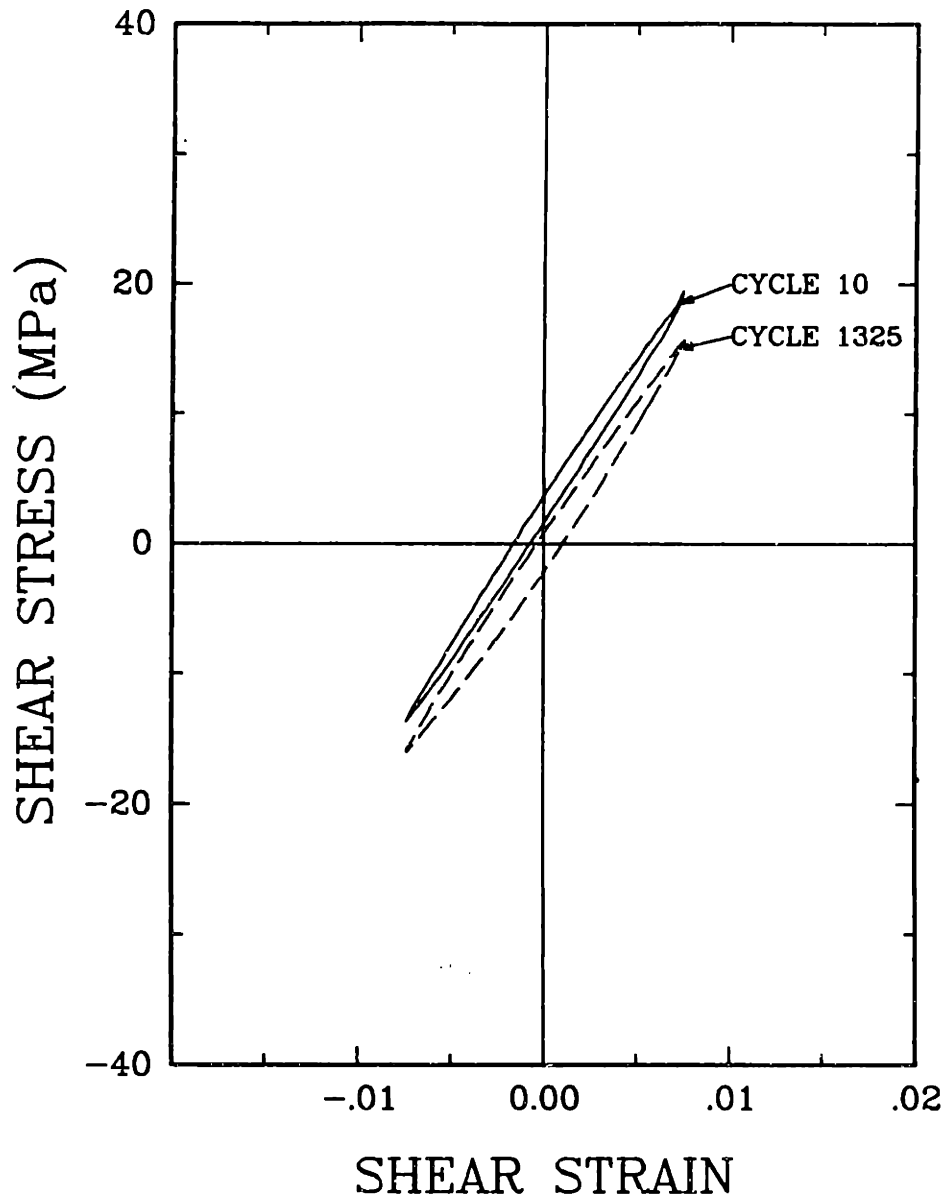

Figure 68: Hysteresis loops, shear strain range 1.5%

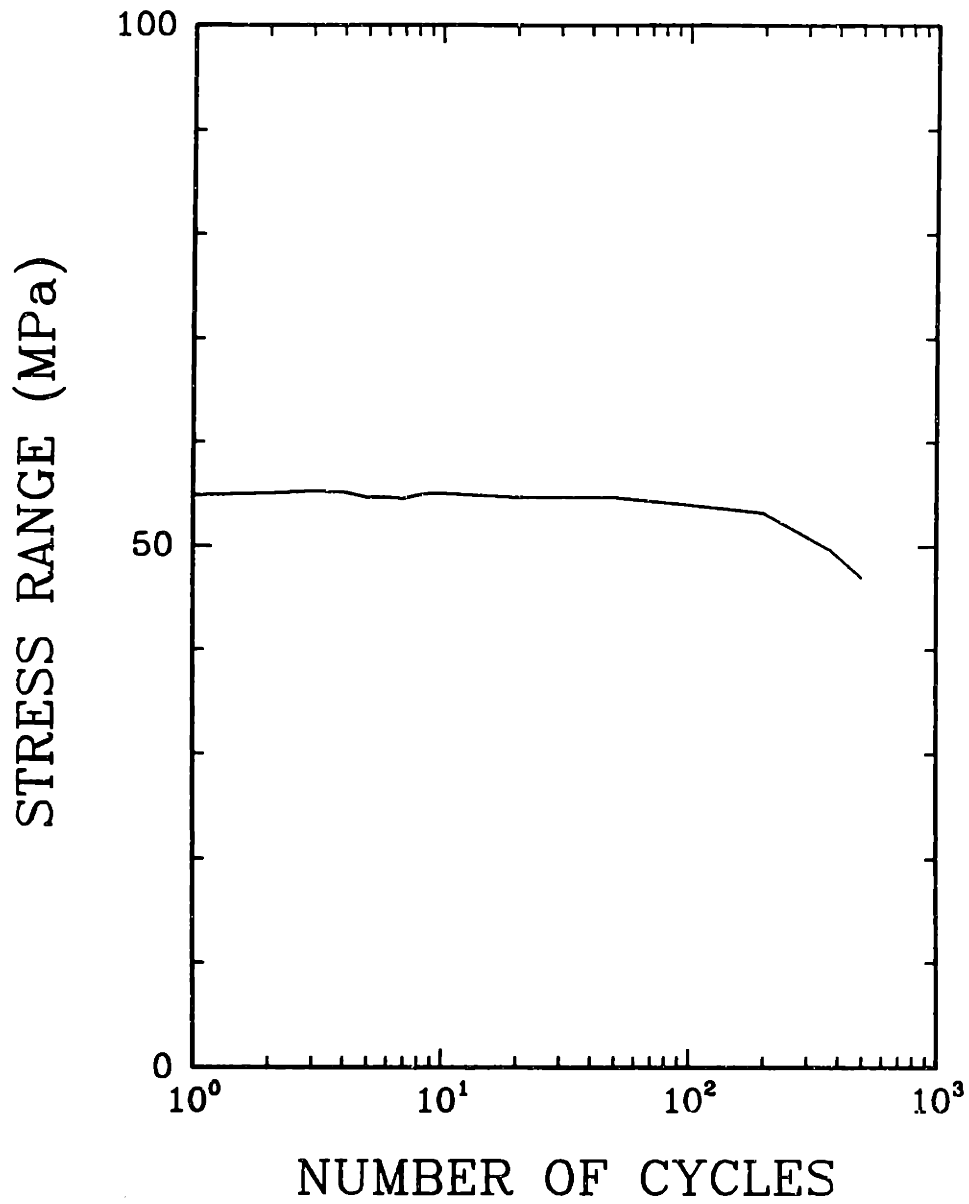

Figure 69: Stress range variation during the test, shear strain range 3.0%

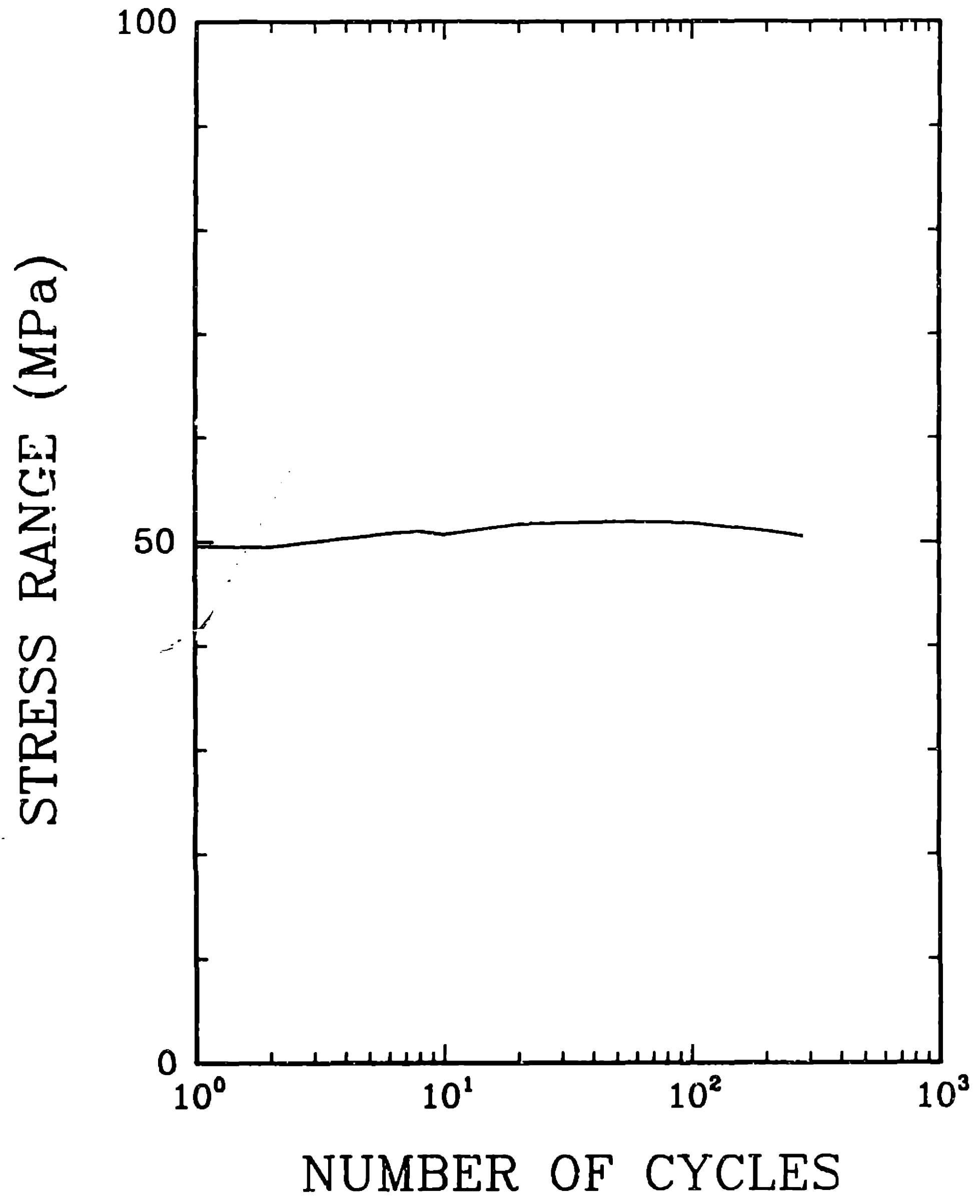

Figure 70: Stress range variation during the test, shear strain range 2.5%

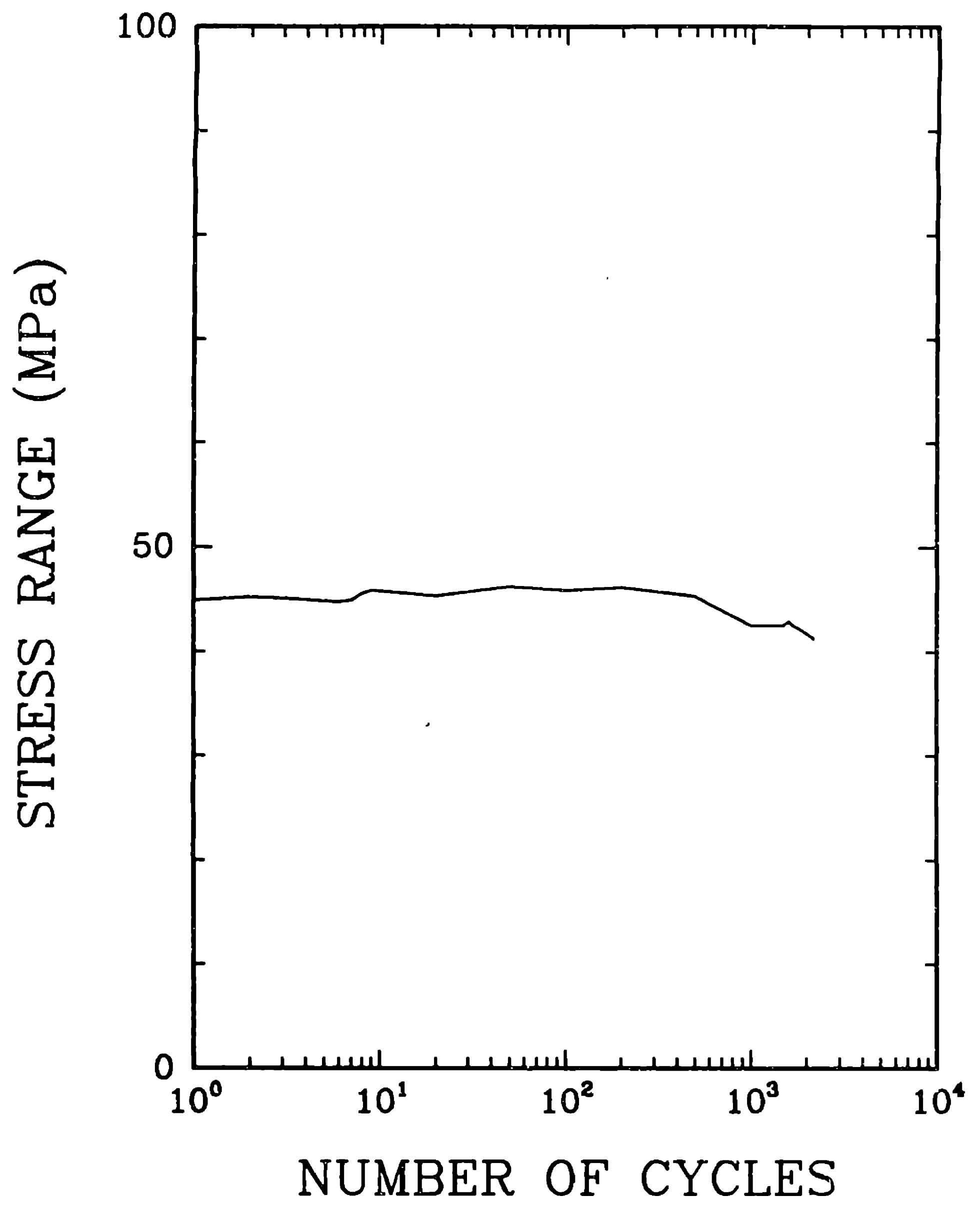

Figure 71: Stress range variation during the test, shear strain range 2.0%

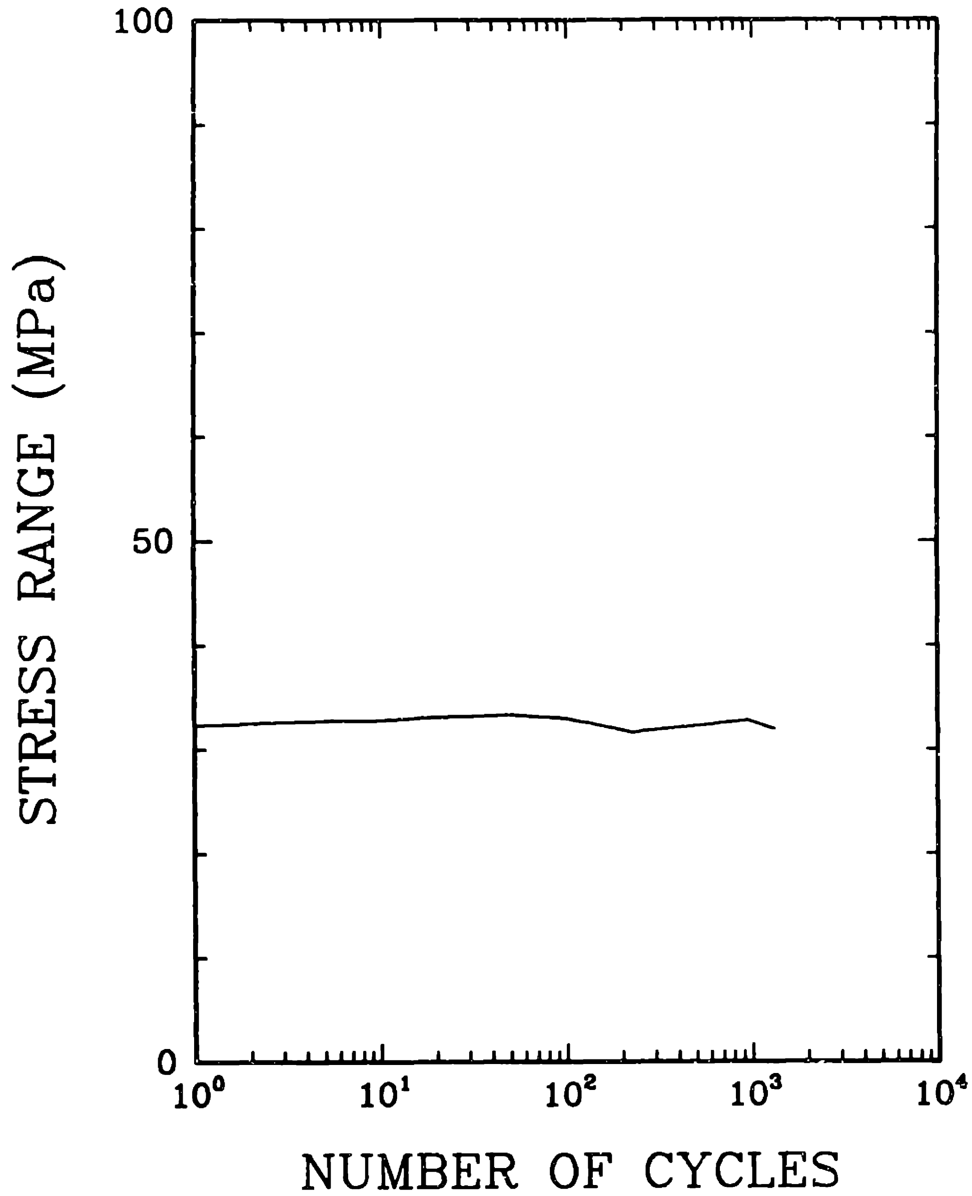

Figure 72: Stress range variation during the test, shear strain range 1.5%

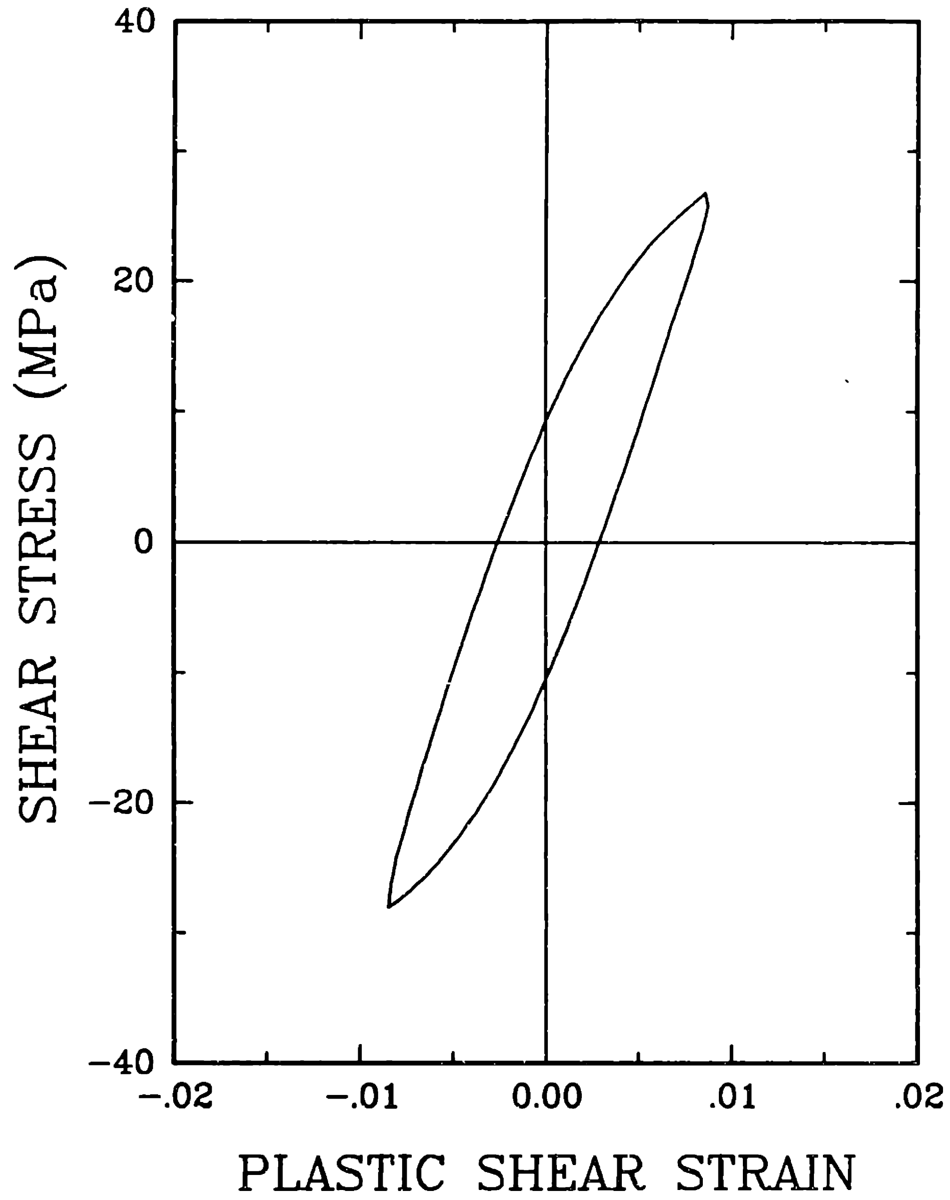

Figure 73: Plastic strain hysteresis loop, cycle 10, shear strain range 3.0%

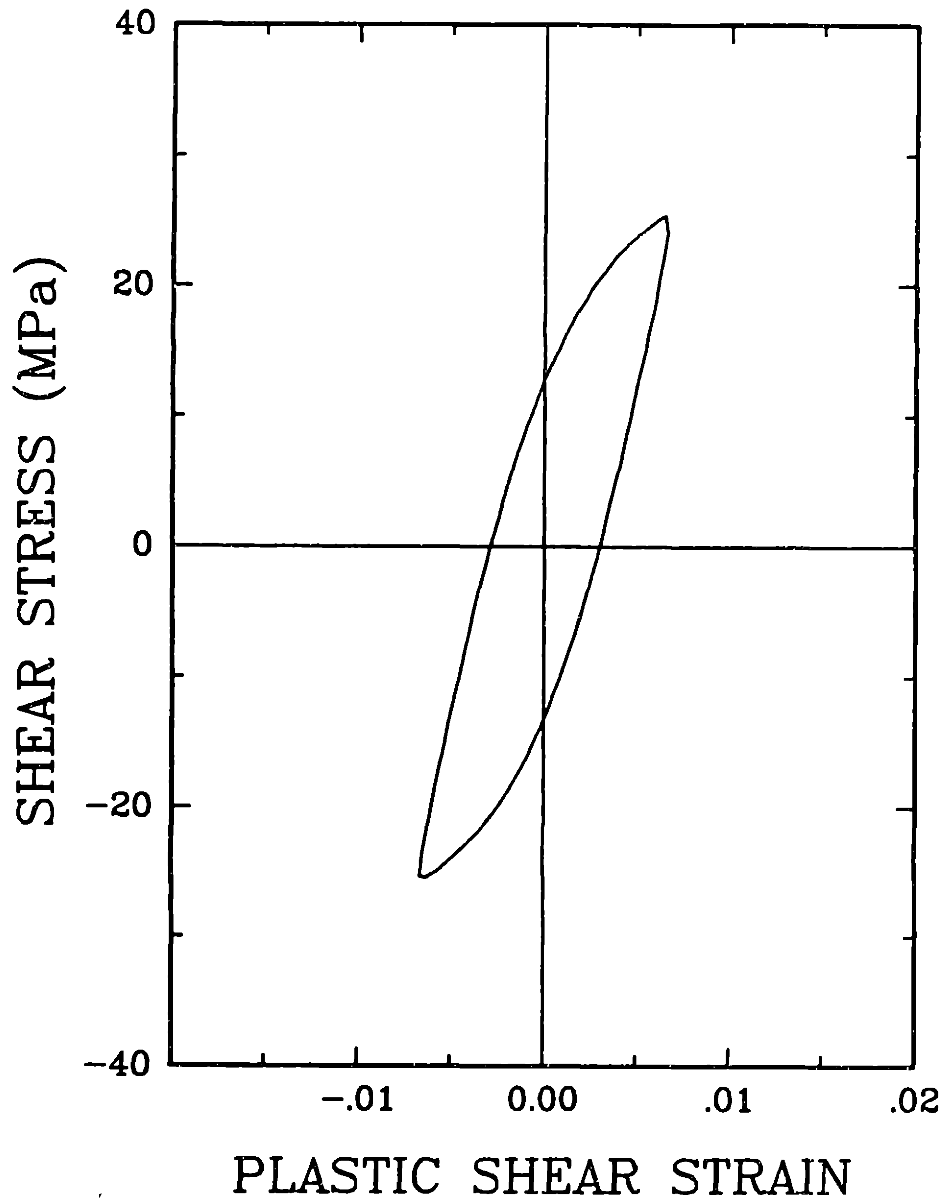

Figure 74: Plastic strain hysteresis loop, cycle 10, shear strain range 2.5%

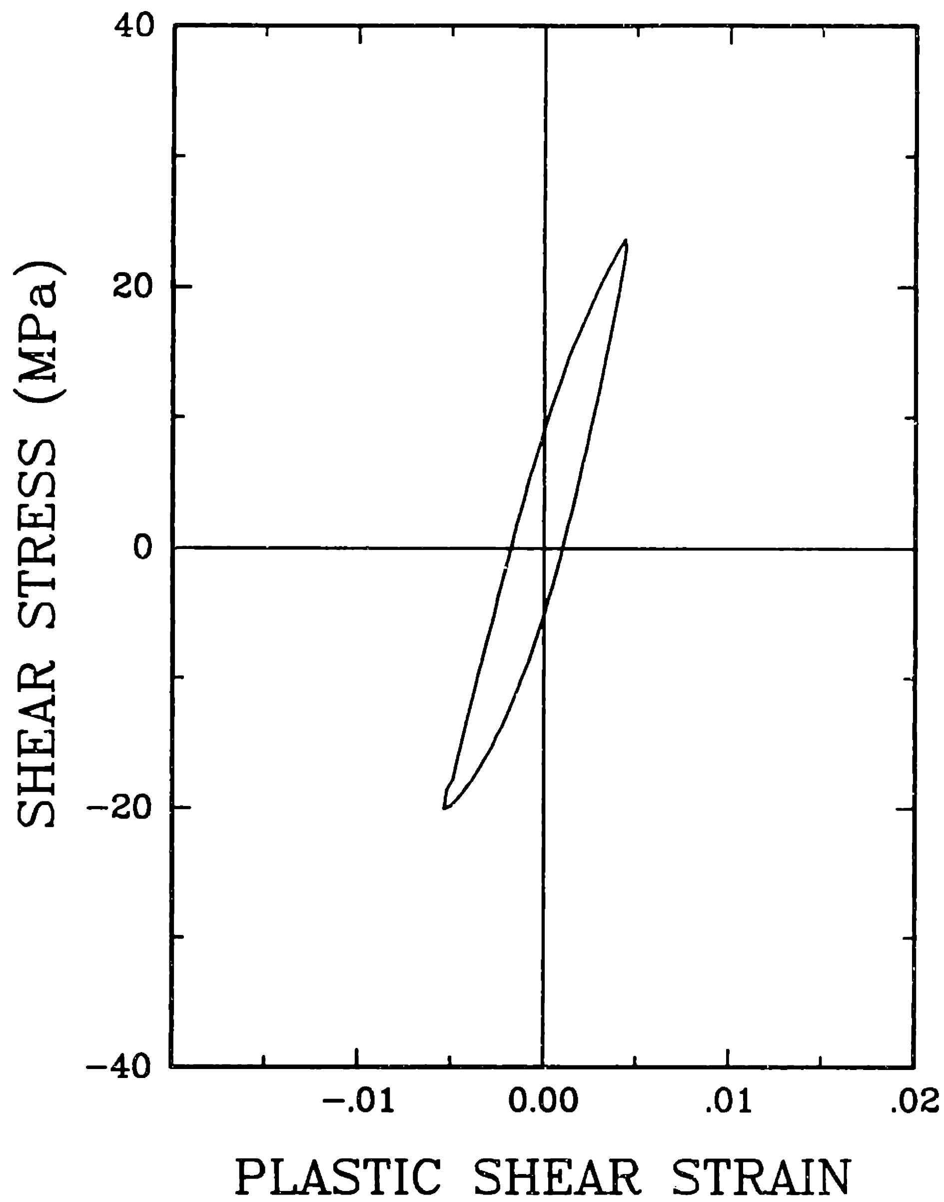

Figure 75: Plastic strain hysteresis loop, cycle 10, shear strain range 2.0%

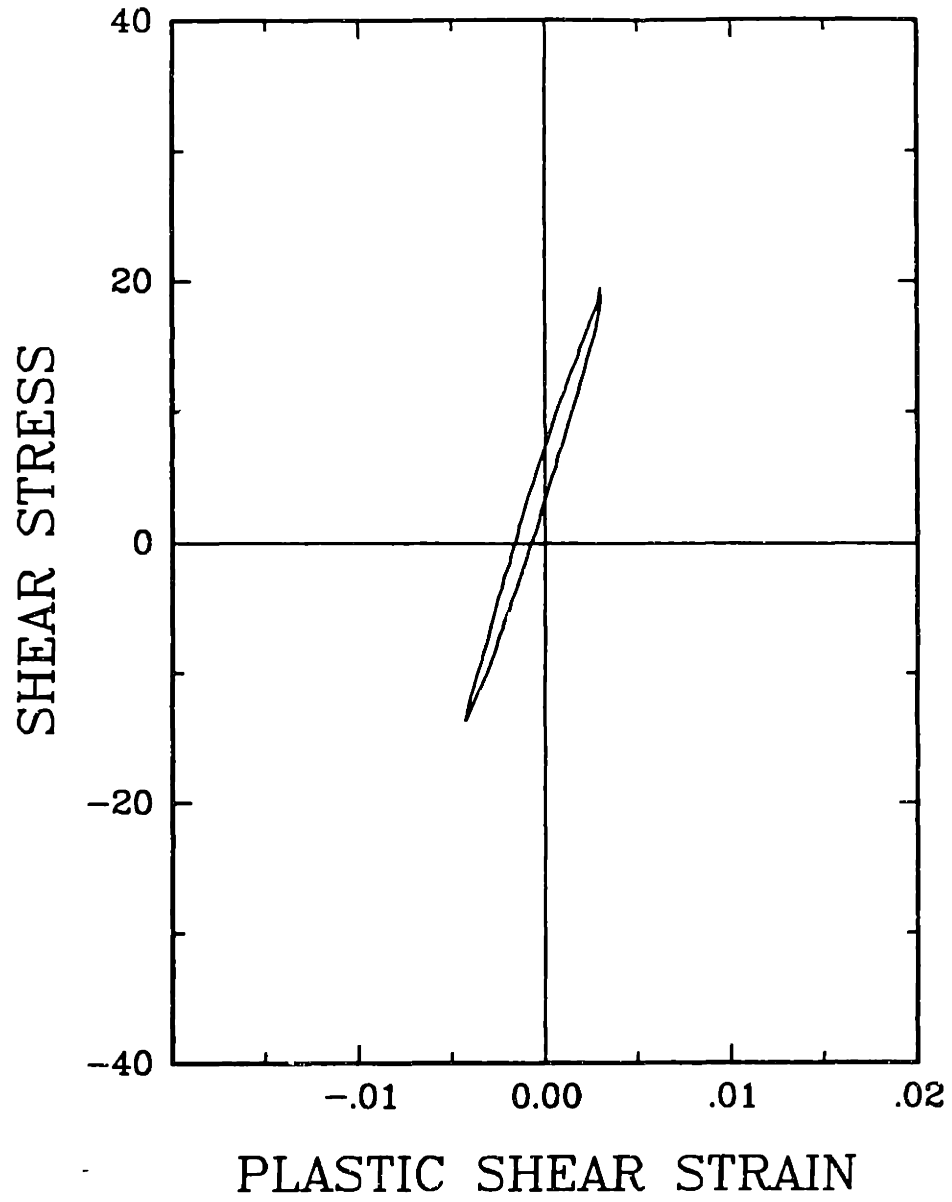

Figure 76: Plastic strain hysteresis loop, cycle 10, shear strain range 1.5%

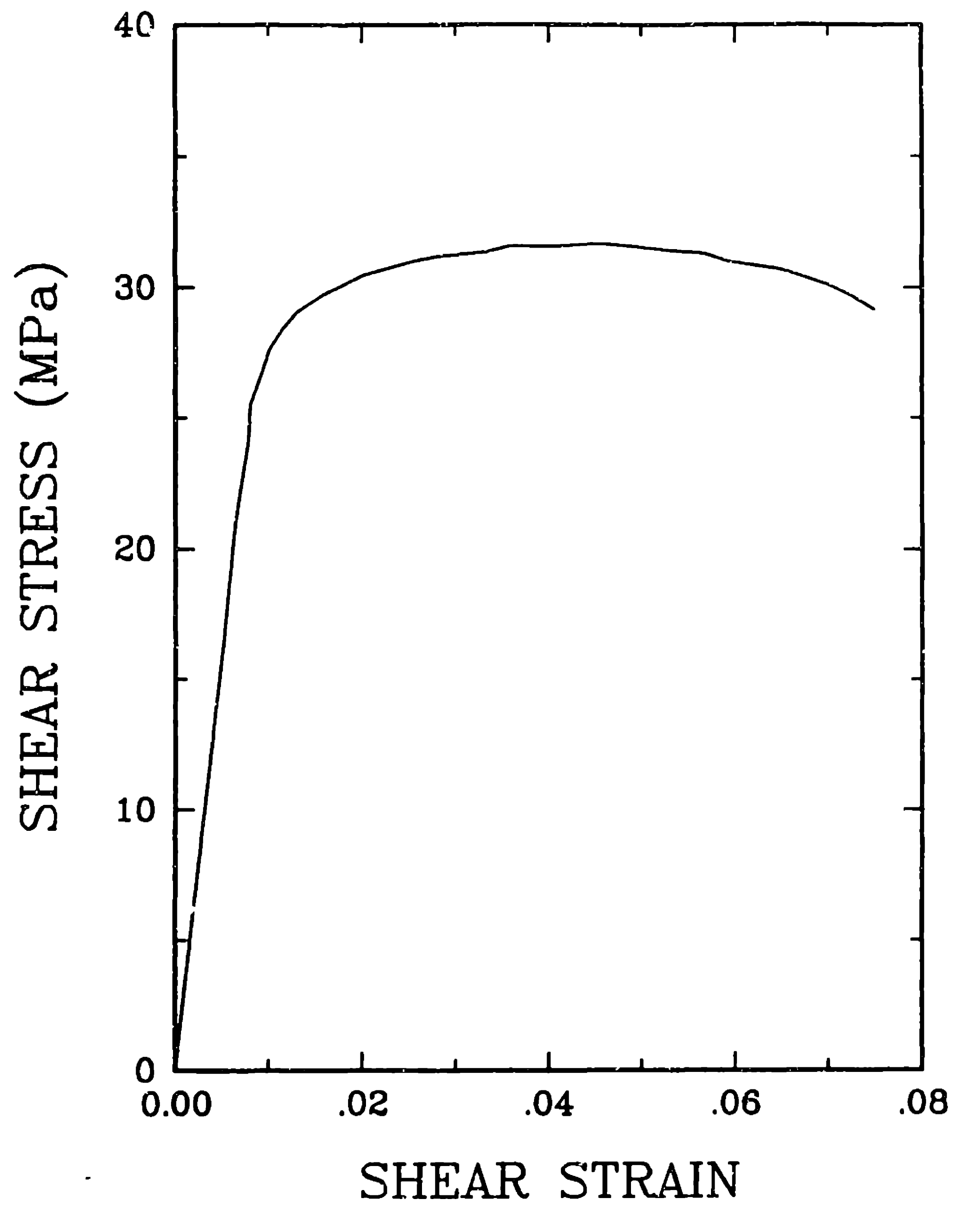

Figure 77: Stress-strain curve from monotonic shear test.

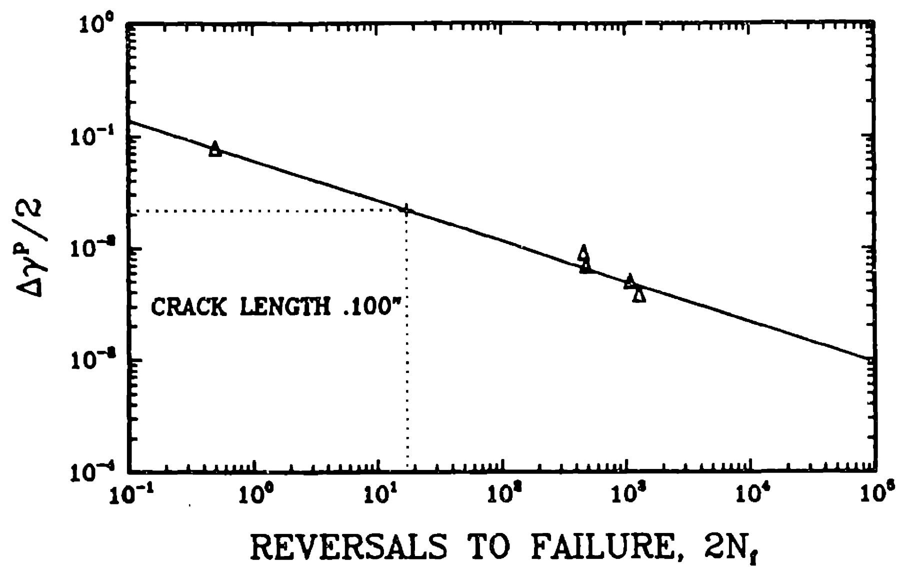

Figure 78: Shear fatigue life curve for a .100" crack

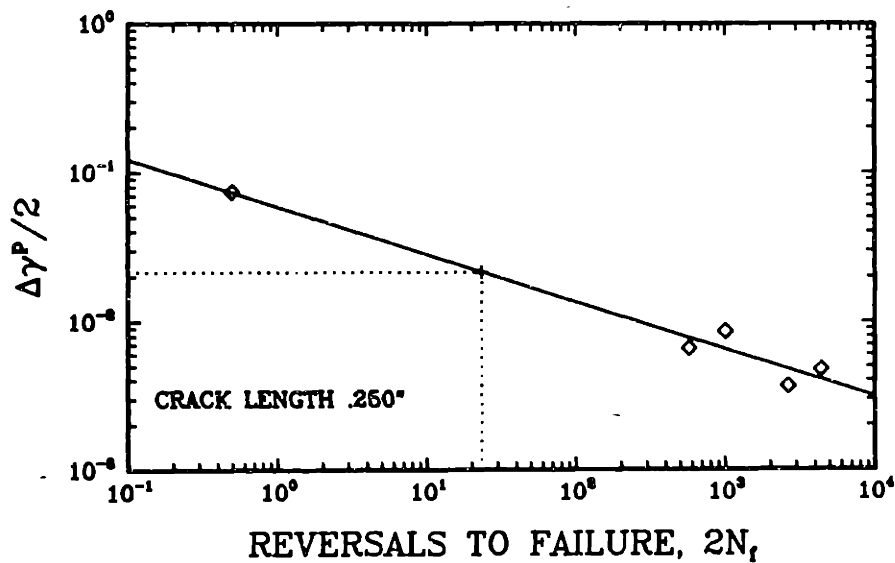

Figure 79: Shear fatigue life curve for a .250" crack

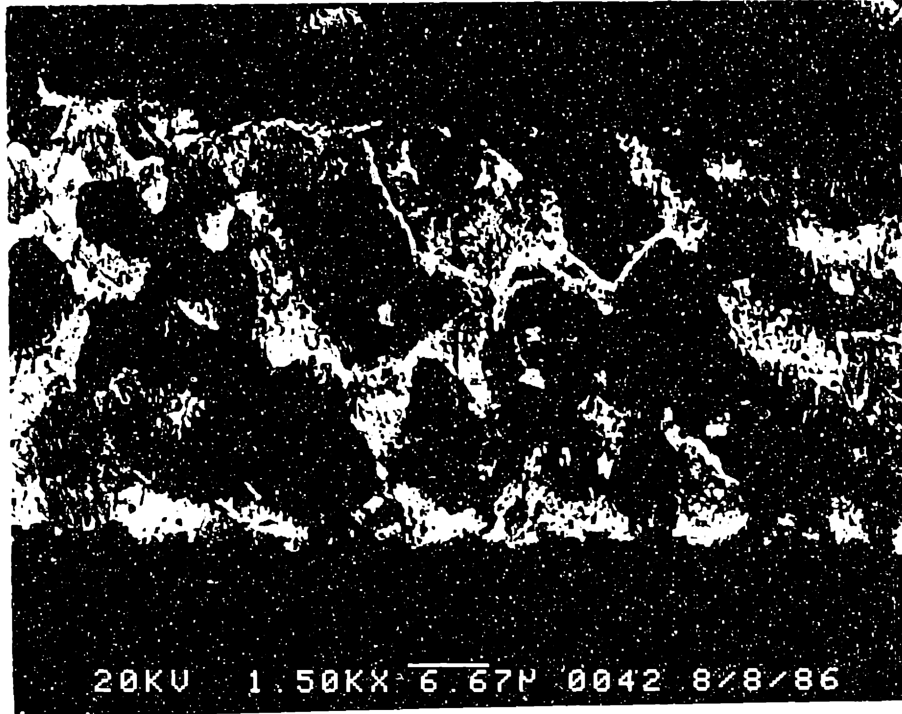

Figure 80: Thinnest section of solder joint

Figure 80: Thinnest section of solder joint

INTENTIONAL DUPLICATE EXPOSURE